MELTING OF METHANE ADSORBED ON GRAPHITE STUDIED BY NUCLEAR MAGNETIC RESONANCE

Thesis by

Michael Steven Pettersen

Submitted in partial fulfillment of the requirements

for the degree of Doctor of Philosophy

California Institute of Technology

Pasadena, California

1988

(Submitted May 11, 1988)

to Karen

Acknowledgements

It is a pleasure to remember all of the people who have helped me through the years towards the completion of this work.

First and foremost, I must thank my advisor, David L. Goodstein, for his patient encouragement and good advice. I hope that I am a better physicist for having worked with him.

I would also like to thank:

Don Strayer and John Dick, who taught me everything I know about RF electronics; Milton Cole and Bob Housley, who contributed to my scientific education; Nils Asplund, Ed Boud and Sandy Santantonio for invaluable technical assistance; and my officemates through the years, Jeff Hamilton, Mike Weimer, Roya Maboudian, Mark Lysek and Carlo Carraro, for many stimulating conversations, on scientific matters and others more abstruse.

Thanks also to the folk at the Caltech glass shop, Xavier Glass of Santa Ana, and Glass Instruments of Pasadena, for beautiful work on a very recalcitrant dewar.

For generous financial support, thanks to the Feynman fellowship fund, the J. S. Stemple fund, and the Schlumberger foundation. This research was supported in part by DOE contract no. DE-FG03-85ER45192.

Thanks also to Shirley Marneus, Olaf Frodsham and Delores Bing, who sustained with offerings of ambrosia the other Muses besides Urania; without which sustenance life at Caltech would have been vastly bleaker.

Among the most valuable things that I acquired at Caltech is the friendship of such as Francis, Maureen, Cheryl, Rosana, Mark, Jim, Pat, Vicky and last but far from least, IRus; and many others too numerous to list. Thanks to Richard for everything.

And finally, very special thanks to my parents, AAge and Roslyn Pettersen.

"See what you have done!... In a few minutes I shall be all melted, and you will have the castle to yourself. I have been wicked in my day, but I never thought a little girl like you would ever be able to melt me and end my wicked deeds. Look out—here I go!"[1]

Abstract

An NMR survey of the system of methane adsorbed on graphite, over a range of 70-105 K in temperature and .87-51 layers in coverage, is presented. The data are analyzed in terms of current models of the phenomena occurring in adsorbed films, such as wetting, roughening, surface melting, and melting.

The interaction between the substrate and adsorbate and its effect on T_1 is quantitatively analyzed in terms of a model of fixed paramagnetic spin centers in the substrate. Since the T_1 effect is very sensitive to the distribution of the adsorbate with respect to the surface, it is shown that it can be used as a powerful diagnostic tool for the study of wetting behavior in thick films where other techniques are insensitive.

While T_2 is also affected by the substrate, we show that it can still be used as a probe of molecular mobility in thin films. Roughening is found to cause an enhancement of mobility in a region of about 4 layers on the surface of the film.

A new, complete thermodynamic model of surface melting, applicable to adsorbed films, is presented, and possible new phase transitions are predicted. The data for methane on graphite are found to be inconsistent with the hypothesis of surface melting.

Finally, the bulk melting transition is traced from thick films all the way down to 1.39 layers. The transition is observed to persist to the thinnest supermonolayer films studied, in a region where previous heat capacity studies have shown the latent heat to vanish.

Contents

List of figures and tables

Chapter 1

The Problem of Melting

Aristotle says,[2]

> Water solidifies owing to the departure of heat; so it will clearly be dissolved by the entry into it of heat: cold, therefore, must be the agent in solidifying it.

Two thousand years of progress in physics have not overturned Aristotle's hypothesis, but have merely sharpened the question: viz., how does the transition between the two states of matter, solid and liquid, occur? That is the problem this thesis will address.

§1.1 Atomic theory

In the nineteenth century, with the introduction of the mechanical theory of heat, the following picture of melting began to arise. We imagine the molecules of a solid tethered to their lattice sites by a harmonic potential (the cohesive energy of the crystal). About these positions, the molecules may vibrate, due to their thermal energy. When the thermal energy becomes sufficient to unbind the molecules from the potential wells, the solid melts.

To quantify this picture, we start from the Debye model of vibrations in the crystal, and compute the RMS displacement of the molecules by thermal phonons. An excellent estimate of the melting temperature of many materials is provided by the temperature at which this displacement becomes some fixed proportion of the lattice spacing (Lindemann's law[3]). We have thus succeeded in deriving the melting temperature from the elastic properties of the medium. However, the model does not explain why the transition occurs so abruptly, rather than spreading out over a finite temperature range, nor why there is a discontinuity in the entropy (i.e., a latent heat); instead it gives a picture of the solid gradually turning to mush as the temperature approaches the triple point. However, melting in three dimensions is universally a first-order phase transition.[4]

§1.2 KTHNY

A more sophisticated model of melting was presented in 1973 by Kosterlitz and Thouless,[5] and later elaborated by Halperin, Nelson and Young:[6] hence the alphabet-soup title KTHNY.

The basic idea of the model is that since dislocations can glide through a crystal, it might be possible to soften the crystal to shear by generating enough dislocations. At any non-zero temperature, pairs of dislocations of opposite Burger's vector will be thermally excited. These pairs are bound, because the elastic strain energy of a bare (unpaired) dislocation is macroscopically large, varying as the log of the crystal size. However, the dislocation pairs can soften the elastic constants of the crystal by polarizing in response to the applied stress. When the temperature is high enough to produce many small pairs, the elastic constants at large scales may be softened enough to let the large bound pairs separate as far as the edges of the crystal. When this happens, the crystal loses its resistance to shear stress.

Because the lines of dislocation need not be straight, the model unfortunately proves intractable in three dimensions. In two dimensions, however, dislocations are point defects, and the model can be solved using the methods of the renormalization group. (This calculation applies to any two-dimensional system with point-like objects interacting by a logarithmic potential, such as a two-dimensional plasma, superfluid or superconductor, where the objects are respectively point charges, vortices and flux lines.)

The result differs from our three-dimensional experience in two major points. For one thing, it predicts that melting proceeds via two distinct transitions: first the long-range translational order breaks down, and then the long-range orientational order. (In two dimensions long-range crystalline order decays algebraically with distance,[7] but this can nevertheless be distinguished from the exponential decay characteristic of liquids.) The intermediate phase, something like a liquid crystal, is called *hexatic*. The second difficulty is that neither of these two transitions is first order: indeed, all

thermodynamic quantities are infinitely continuous across the boundaries.

Would the predictions of the KTHNY model lead to a first-order transition if it could be solved in three dimensions? Is KTHNY behavior observable in two dimensions? And can one pass from two dimensions to three dimensions in a continuous way to show that the melting process proceeds by related mechanisms in different dimensionalities? The answer to the first question may be negative. According to the approximate calculation of Williams,[8] a model which includes vortex rings in bulk liquid helium results in a λ-like transition. The other questions we shall address in the next two sections.

§1.3 Flatland

Our next step is to find some two-dimensional matter. We shall study the behavior of matter adsorbed on a surface. Molecules of a gas are attracted to a surface by Van der Waals forces, with a potential that varies asymptotically as $u(z) \sim -C_3/z^3$, where C_3 is a constant characteristic of substrate and gas. A single molecule trapped in the ground state of this potential well cannot exercise its third degree of freedom, but it can translate across the surface. Thus its behavior is effectively two dimensional. Many systems of different gases on different substrates have been studied, as well as exotic systems such as styrofoam in water[9] and electrons on liquid helium;[10] and they exhibit phase diagrams which mimic three-dimensional behavior, showing gas, liquid and solid phases in two dimensions. Unfortunately, the only claim of direct experimental evidence of a KTHNY transition in an adsorption system is for the λ transition in two-dimensional liquid helium.[11] Frequently, the two-dimensional melting transition is first order,[12] though not always;[13] some systems show a tricritical point where the order of the transition changes.[14]

Of course, there are modes of vibration perpendicular to the surface, and the surface, being made of atoms, is corrugated. The effects are not insignificant. For example, the corrugation produces a band structure in the two-dimensional translational energy,

which can be experimentally detected in the film's heat capacity.[15] Another effect is the existence of *registered* or *commensurate* phases in which the lattice constant of the adsorbate becomes locked to that of the substrate. The possibility of registry is important, as we shall remark in the next section.

§1.4 Beyond flatland

Once we move out of the submonolayer regime, the world becomes ever more complex. Our naïve hope that two-dimensional behavior evolves smoothly into three dimensions is incorrect: whole new species of film behavior evolve in the multilayer regime. This section attempts to touch on the highlights of multilayer taxonomy.

The first question is whether a film of arbitrary thickness can be formed at all. If the attraction of the adsorbate to itself is greater than its attraction to the substrate, it may be energetically favorable for it to form islands, beads or crystallites of bulk material instead of a uniform film. If, on the other hand, the film can be made to grow to macroscopic thickness before bulk material starts to condense, the adsorbate is said to *wet* the substrate. Young's law[16] for the contact angle θ of a bead with the surface, $\sigma_{g\omega} = \sigma_{i\omega} - \sigma_{ig} \cos\theta$ (where the σ's are the surface tensions between the adsorbed phase i, its co-existing vapor g, and the substrate ω), indicates that complete wetting should occur ($\theta = 180°$) for $\sigma_{g\omega} \geq \sigma_{i\omega} + \sigma_{ig}$.

However, if the adsorbate is solid, and the substrate potential is sufficiently strong, then the first few layers will form under great strain, and the energy cost of healing the strain may preclude further growth of the film. In general, solids are not expected to wet solids, according to Huse[17] and Gittes and Schick,[18] unless epitaxial growth is promoted by an accidental commensurability between bulk and substrate lattice constants.[19] The non-monotonic dependence of wetting on substrate potential is shown in the data of Bienfait et al.[20]

In 1977, Cahn showed that even if a liquid (or binary fluid mixture) does not wet at low temperature, it must do so in the region of the critical point.[21] This opens the

prospect of a *wetting transition* at some temperature. This seminal paper sparked the current interest in wetting phenomena.

The relevance of wetting to the present experiment is apparent from the work of Pandit and Fisher.[22] Near the triple point, even if both solid and liquid wet, the difference in surface tensions between the two phases may make one or the other energetically favored in a region of temperature where the bulk is unstable. Then, films of macroscopic thickness cannot form. This phenomenon is called *triple point dewetting*, and will be discussed further in Section 3.3.

An extraordinarily thorough review of wetting is to be found in the work of Dietrich.[23]

Next, we ask whether the film forms smoothly, the number on the surface being a continuous function of chemical potential, or whether each layer undergoes a condensation analogous to the two-dimensional gas-solid or gas-liquid transitions. According to the lattice-gas model of Pandit et al.,[24] at low temperatures, condensation is stepwise, but the layering transitions end in critical points, above which growth is continuous. (The same behavior is seen in the 6-state Potts model of Conner and Ebner,[25] which elaborates on the lattice-gas model by including a liquid-like phase.) The limit of the critical points as the number of layers becomes infinite is the *roughening transition*, a property of the bulk solid surface. This transition has been observed in only a few systems.[26–28]

Another possibility that can arise near the triple point is *surface melting*. Since the molecules at the surface of a solid have lower co-ordination than those in the interior, and thus lower binding energies, it might be anticipated that they will melt at a lower temperature than the bulk. Thermodynamically we would expect surface melting if $\sigma_{sg} \geq \sigma_{sl} + \sigma_{lg}$, where the phases indicated by the subscripts are solid, liquid and gas. Then the liquid wets the solid, and the surface energy is reduced by introducing an intermediate layer of liquid. It has been argued[29] that surface melting and triple point

dewetting are mutually exclusive phenomena; but our complete thermodynamic analysis of Section 3.5 will show otherwise. Surface melting has been observed in a number of systems.[30,31]

From this brief survey it is clear that melting in the multilayer regime is a phenomenon of diverse aspect.

§1.5 Experimental techniques

The experimental techniques used to examine film behavior fall into four main categories.

1. *Thermodynamic*. This includes measurements of heat capacity and vapor pressure. Adsorption measurements of this type date back at least to Boyle.[32] The thermodynamic technique can detect the presence of phase transitions, but cannot tell what phases are present.
2. *Volumetry* by ellipsometry, fiber oscillator microbalance and capacitance microbalance. These techniques are good detectors of layering phenomena and wetting transitions. The fiber oscillator is also in principle capable of detecting changes in rigidity in the film, though the quantitative interpretation is complex.
3. *Scattering* of anything that can be focussed on a surface, including neutrons, electrons, helium atoms, and X-rays. These techniques are sensitive to spatial structure.
4. *NMR*, which directly probes the frequency distribution of molecular motion in the film. It is thus complementary to the other methods.

The work presented in this thesis is intended to complement a previously published thermodynamic survey.[26]

§1.6 Methane and Grafoil

The system chosen for this study is methane adsorbed on graphite. This section reviews the important physical properties of the materials and concludes with a brief survey of previous work on the methane/graphite system.

1. *Methane*

It is desirable to keep the adsorbate molecule as simple as possible. Complex molecules possess angle-dependent interactions which can complicate the picture; indeed the study of orientational orderings on surfaces is a well-developed field in its own right.[12,33,34] Those isotopes of the noble gases which possess nuclear magnetic moments are rare and expensive, leaving methane the adsorbate of choice. The four protons per molecule provide a large NMR signal.

Methane possesses the tetrahedral symmetry T_d, so its lowest non-zero permanent electrostatic moment is the octupole, of magnitude 3×10^{-34} esu cm^2.[35] For a lattice spacing of about 4.1 Å,[36] this results in an interaction energy of 3.2 K.[37] Below 20 K, methane undergoes a λ-like transition to an orientationally ordered state.[36] Above the λ point, however, the molecules rotate independently.

The length of the C-H bond is 1.09 Å,[36] leading to a moment of inertia of 5.3×10^{-40} g cm^2. The small moment of inertia results in a large spacing between rotational energy levels; the lowest excited state is 15 K above the ground state. At the temperatures of the present experiment, however, methane is essentially a classical rotator, as can be seen, e.g., in the rotational heat capacity, which approaches the classical value of 3/2 k_B.[38]

The Fermi statistics of the protons leads to a correlation between the molecular angular momentum and the nuclear spin state; however, as shown in Appendix I, the correlation is unimportant in the present experiment because the molecular rotation is in the classical limit.

2. *Graphite*

The substrate used in this experiment is a commercially available graphite product called Grafoil.* The structure of graphite makes it easy to cleave along the (0001) plane,

*Grafoil is a registered trademark of the Union Carbide Corporation.

and it is possible to produce powders that have large surface areas that are atomically flat. Grafoil is produced by the process of exfoliation, in which natural crystals of Madagascar graphite are intercalated and then heated rapidly, fracturing the crystal. The resultant powder is pressed into sheets for use as a lubricant. The flakes are about 1-4 μm across and 500-1000 Å thick;[39] the correlation length for surface flatness is 100 Å;[40] 30% of the flakes are aligned with the sheets with a deviation of ±13°.[41] The introduction of similar exfoliated graphites in the early 1960's[42] revolutionized adsorption physics by providing materials with high specific area and good surface homogeneity. (NMR experiments on submonolayer methane were done from the early days of NMR,[43] but the results were not satisfactory because of the low homogeneity of the rutile substrate.) Although Grafoil is not the most uniform graphite substrate available,[44] it was chosen for this experiment because of its high specific area.

There are some difficulties posed by the use of graphite as a substrate in an NMR experiment, which are summarized in Appendix II. In particular, Grafoil is known to produce a shortening of T_1 and T_2 in adsorbed films; the effect on T_1 has not heretofore been satisfactorily investigated. While studies have shown that MgO smoke can provide nearly the surface quality of Grafoil,[45] neutron scattering data for methane on MgO show that the melting transition is pre-empted by surface melting,[30] and hence it is not a suitable substrate for the present experiment.

3. *The methane/graphite system*

Methane on graphite has been studied extensively in the submonolayer regime by a variety of techniques. The most complete phase diagram to date[46] is shown in Figure 1. It is not known whether the second layer possesses a melting transition analogous to the first. An unidentified transition that might be associated with second layer melting, detected in vapor pressure experiments,[26] is shown also in the same figure.

The 1-3 layer regime at low temperature has been studied both experimentally[47] and theoretically[48] to understand why the solid phase wets. The results, while not

Figure 1. *Submonolayer phase diagram for methane on graphite, showing 2D liquid (L), gas (G), commensurate solid (CS), expanded (low density) incommensurate solid (ES), and dense incommensurate solid (DS)*

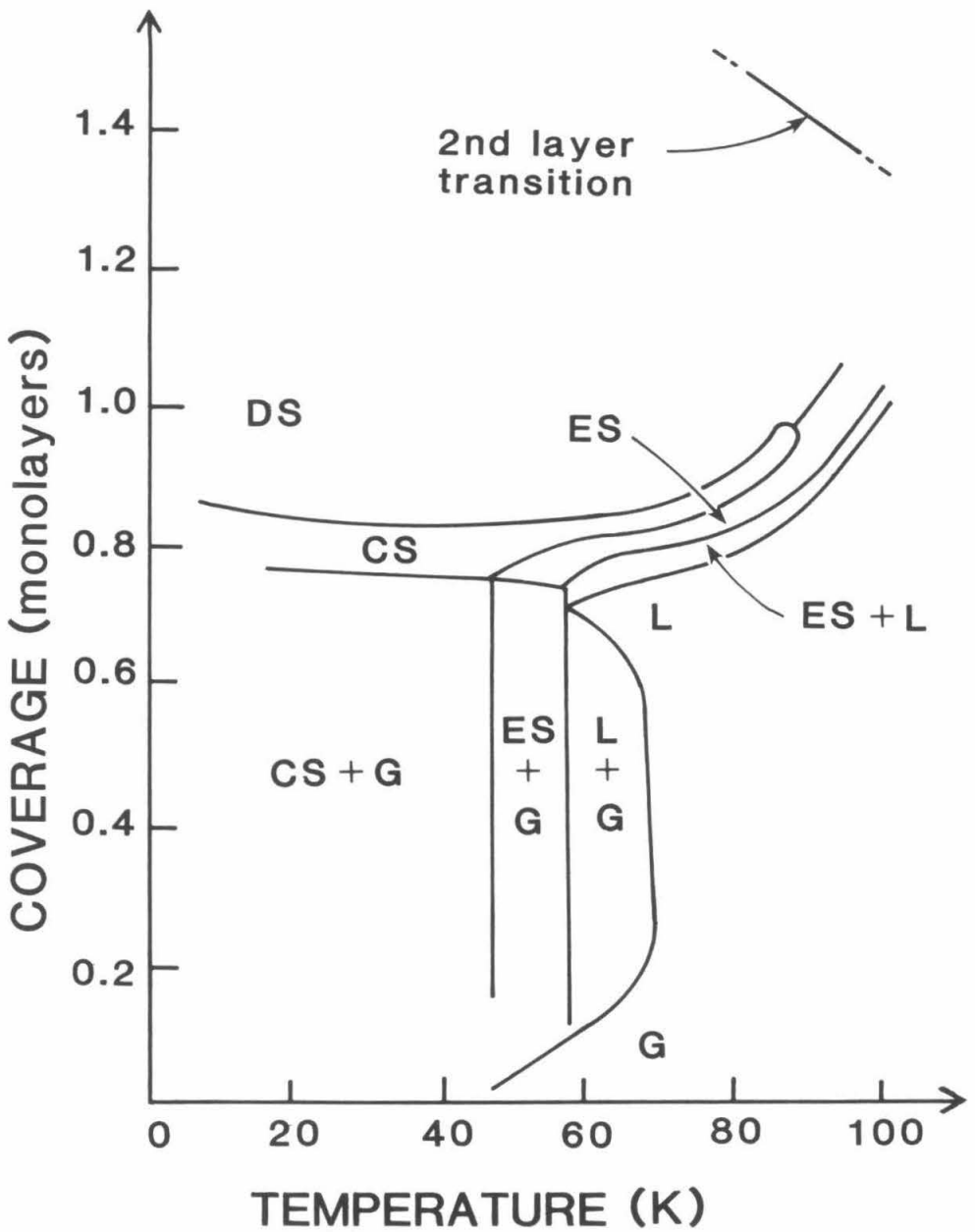

definitive, support the conjecture[49] that the accidental near match between the lattice constants of methane and graphite enable the film to break free of registry and grow at the natural bulk density. Below 40 K, LEED data[50] suggest that methane fails to wet graphite. This result disagrees with the heat capacity results of Kim et al.,[51] who find that wetting occurs at least as low as 20 K, with a possible transition to non-wetting at 11 K. Heat capacity experiments at higher temperatures[26,52] show wetting in the region above 65 K, with a triple point dewetting transition at 90.48 K, just below the triple point of 90.66 K.

The heat capacity experiments have traced the melting transition from about 18 layers to 4 layers, where the latent heat vanishes, as shown in Figure 2. However, according to an argument of Landau,[53] the melting transition cannot end at a critical point. It is therefore important to learn what happens to the melting transition for thinner films where the transition becomes continuous and cannot be studied by heat capacity techniques.

§1.7 Prospectus

In this thesis we shall attempt to explore several of the themes brought out in the preceding sections. We shall study the effect of Grafoil on T_1 in the adsorbate and present a quantitative model showing that it is due to fixed paramagnetic centers in the substrate. The strong dependence of the effect on the distance of the film from the surface will then be used to study the wetting behavior of methane on graphite in films so thick that no other experimental technique can distinguish them from bulk. We shall develop a model of surface melting applicable to the case of an adsorbed film, and show that it is not compatible with our data. Finally, we will use T_2 to study the thin film regime, where we shall find that the surface layers of the film show an enhanced mobility with respect to the bulk, attributable to roughening, but that the melting transition otherwise appears to extrapolate smoothly from the bulk all the way down to one layer.

Figure 2. *Latent heat of melting*

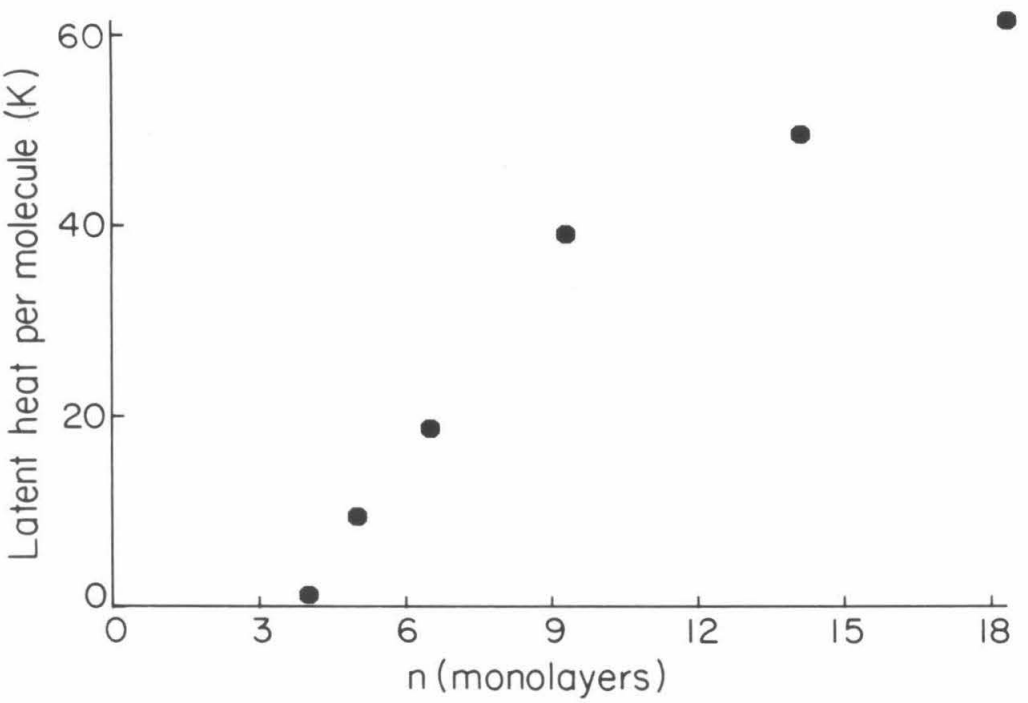

Chapter 2

Fundamentals of Nuclear Magnetic Resonance

This chapter presents a terse introduction to the basic concepts of nuclear magnetic resonance.[54] It is not intended to catechise the uninitiated, but to refresh the reader's memory of the terminology of the faith. Those already communicant may skip this chapter without loss.

§2.1 Nuclear magnetism

Nuclei of non-zero spin possess a magnetic dipole moment $\vec{\mu}$, which (according to the Wigner-Eckart theorem) is collinear with the nuclear spin $\hbar\vec{I}$. The constant of proportionality between the two vectors is called the gyromagnetic ratio γ: $\vec{\mu} = \gamma\hbar\vec{I}$. This magnetic moment is a quantum mechanical object, although there exists a classical analogue in the moment of a rotating distribution of charge.

For a Dirac point particle,[55] the gyromagnetic ratio is given by $\gamma = g\,e\,/2Mc$, with e and M the charge and mass of the particle, c the speed of light, and the Landé g-factor is 2; for a nucleus, however, g is not required to be 2. Because of the factor of M in the denominator of the gyromagnetic ratio, nuclear magnetic moments are $O(10^3)$ times smaller than that of the electron. The proton possesses the largest magnetic moment of all the nuclei, with $g = 2.79$, or $\mu = 14.1\times10^{-24}$ erg/G.

Because nuclear ground states are parity eigenstates, they cannot possess electric dipole moments. Many nuclei possess an electric quadrupole moment, which plays an important role in NMR; however, the Wigner-Eckart theorem implies that the moment will be zero unless the nuclear spin $I \geq 1$. Since we shall be concerned with protons, whose spin is $I = ½$, we can dismiss all electromagnetic moments except for the magnetic dipole.

§2.2 Resonance

When a magnetic dipole is placed in a magnetic field, it possesses an energy given by the Zeeman Hamiltonian, $\mathbf{H} = -\vec{\mu} \cdot \vec{H}_0$. Since $\vec{\mu} = \gamma \hbar \vec{I}$, the eigenvalues of this Hamiltonian are $E = \gamma \hbar H_0 m$, where $m = -I, \ldots, I-1, I$. An oscillating magnetic field $\vec{H}_1$ rotating in the plane perpendicular to $\vec{H}_0$ can induce transitions $\Delta m = \pm 1$ if the frequency of rotation is $\omega = \gamma H_0$. For typical laboratory magnetic fields, ω is in the radio frequency (RF) range, and thus easily accessible to experiment. The phenomenon of nuclear magnetic resonance was first observed in 1945 by the groups of Bloch[56] and Purcell.[57]

There is a classical analogue to the resonance condition on ω. A classical magnetic moment in a magnetic field experiences a torque $\vec{\Gamma} = \vec{\mu} \times \vec{H}_0$, so the angular momentum $\vec{L}$ obeys $d\vec{L}/dt = \gamma \vec{L} \times \vec{H}_0$. The spin axis therefore precesses about $\vec{H}_0$ at the Larmor frequency $\omega_0 = \gamma H_0$. In the presence of the rotating field $\vec{H}_1$, we can solve for the motion of the spin by changing to a reference frame rotating with $\vec{H}_1$ at frequency ω. In the new (primed) co-ordinates, $\vec{H}_0$ lies along $\hat{z}'$, and $\vec{H}_1$ is fixed along $\hat{x}'$, as in Figure 3. The equation of motion in this co-ordinate system is derived from that in the laboratory frame[58] by substituting $d/dt \rightarrow \partial/\partial t + \vec{\omega} \times$, with $\vec{\omega} = -\omega \hat{z}'$: thus, $\partial \vec{L}'/\partial t = \gamma \vec{L}' \times (\vec{H} + \vec{\omega}/\gamma) = \gamma \vec{L}' \times \vec{H}_{eff}$, where $\vec{L}'$ is the angular momentum in the primed co-ordinates. In the rotating frame, the spin simply precesses about an effective magnetic field given by $\vec{H}_{eff} = \vec{H} + \vec{\omega}/\gamma$. Only for $|H_0 - \omega/\gamma| < H_1$ can the rotating field cause the magnetization to rotate appreciably away from $\hat{z}'$ (producing a change in the Zeeman energy); otherwise, the effect as seen in the laboratory frame is to add a small nutation to the Larmor precession.

In a typical NMR experiment, the average magnetization $\langle \vec{M} \rangle$ of many nuclei is observed. By the correspondence principle, this quantity must obey the classical equations of motion. The rotating co-ordinate frame proves convenient for understanding the macroscopic behavior of the nuclear magnetization.[59]

Figure 3. *Effective magnetic field and motion of spins in rotating frame*

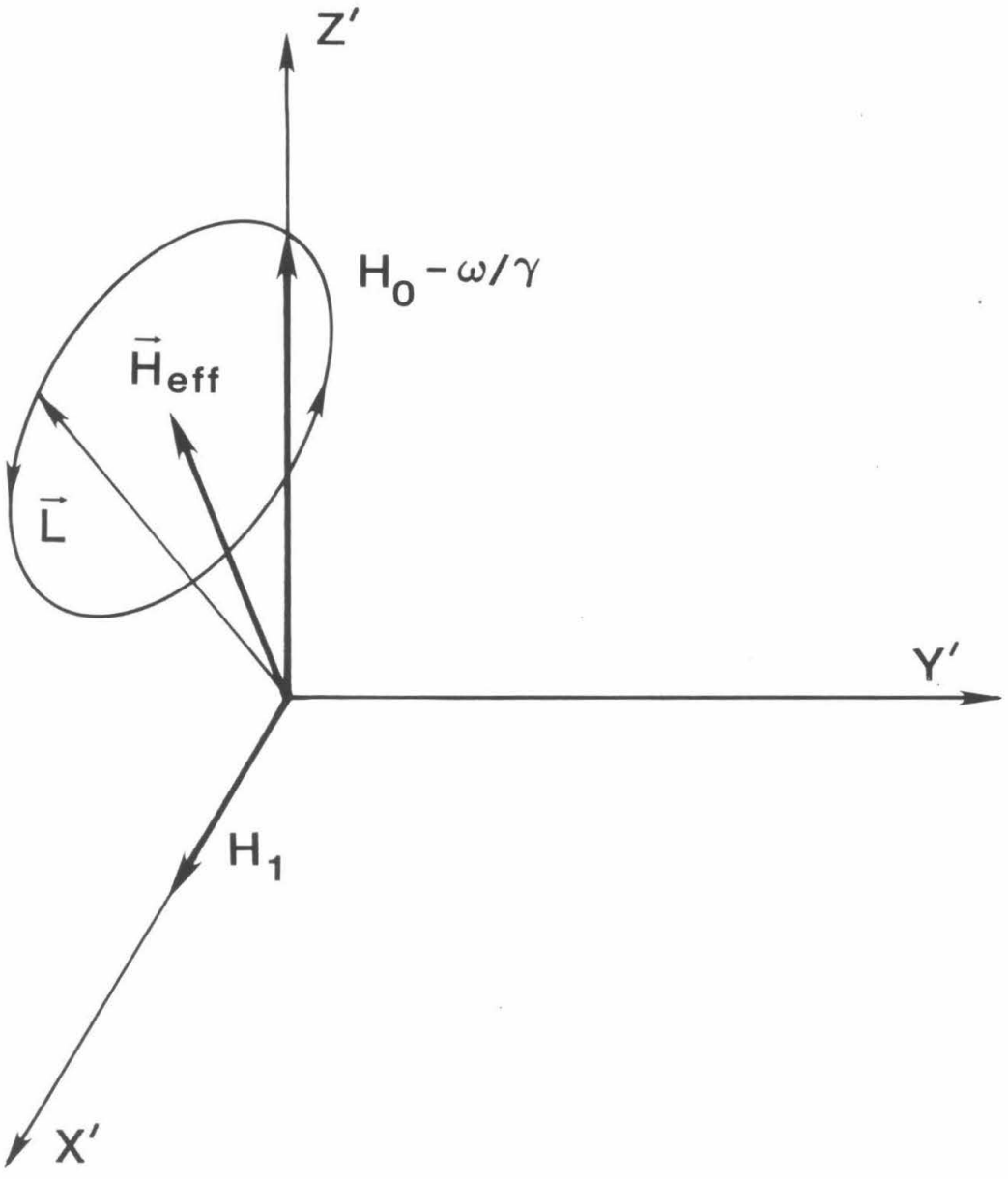

Typically, the oscillating field $\vec{H}_1$ is generated in an experiment by a solenoidal coil. It is thus linearly, not circularly, polarized. The linearly polarized field may, however, be described as the sum of two oppositely rotating circularly polarized fields. The counter-rotating component can be shown to produce small satellite lines at $\omega_0/3$, $\omega_0/5$, etc., corresponding to multiple quantum effects; otherwise we may neglect the counter-rotating field.

§2.3 Thermal equilibrium

In thermal equilibrium, the spins will occupy the various energy states according to the Boltzmann distribution, resulting in a net magnetization $M_0 = N\gamma^2\hbar^2 I\,(I+1)\,H_0/3\,k_B\,T$ for a density of spins N. In the state where all energy levels are equally occupied, and the off-diagonal terms in the density matrix are zero, corresponding to a Boltzmann distribution at infinite temperature, the average magnetization is zero, and since the torque produced by $\vec{H}_1$ is proportional to $\langle\vec{M}\rangle$, the spins do not absorb energy from the RF field. This corresponds to the fact that the quantum transition rates are equal for upward and downward transitions. Only the uneven initial distribution enables the net transfer of energy between the field $\vec{H}_1$ and the spin system.

If the populations are disturbed from equilibrium by the RF field, interaction terms between the spin degrees of freedom and the other degrees of freedom of the system (called the *lattice*) will cause a relaxation of the spins back to the Boltzmann distribution. Interactions amongst the spins cannot change the total energy of the spin system. They conserve the total Zeeman energy, $\langle\vec{M}\rangle\cdot\vec{H}_0$. Therefore, spin-spin interactions can cause decay of the transverse magnetization $M_\perp$, but cannot relax the longitudinal component $M_\parallel$ back to its equilibrium value M_0. The characteristic time for the decay of $M_\perp$ is called T_2. Coupling of the spins with the lattice, on the other hand, can produce an exchange of energy, and can thus relax $M_\parallel$. The characteristic time for this process is called T_1.

§2.4 Spin echoes and saturation recovery

In the present experiment, the nuclear magnetism is sensed by means of the EMF induced by the Larmor precession of the spins in the same RF coil used to generate the field $\vec{H}_1$. Since $\vec{H}_1 \perp \vec{H}_0$, spins precessing about $\vec{H}_0$ will present a sinusoidally varying component of magnetization along the coil axis. The longitudinal component $M_{\|}$, aligned with $\vec{H}_0$, does not precess and cannot be directly detected. Of the transverse components of $\langle \vec{M} \rangle$, one will be in phase with $\vec{H}_1$ and lie along the rotating axis $\hat{x}'$. The other component, 90° out of phase with $\vec{H}_1$, will lie along the axis $\hat{y}'$. Using the oscillator that generates $\vec{H}_1$ as a phase reference, it is possible to separate the two. If the frequency ω of $\vec{H}_1$ is not exactly equal to the Larmor frequency ω_0, the components will be mixed at the beat frequency.

Suppose we apply a pulse of RF energy to the coil long enough to cause the magnetization to precess about $\hat{x}'$ in the rotating frame by 90°, so that $\langle \vec{M} \rangle$ lies along $\hat{y}'$. Such a pulse is called a 90° pulse. Then, as the transverse magnetization precesses about $\hat{z}'$, the induction signal and its decay can be directly measured. By the usual Green's function theory, the Fourier transform of this free induction decay (FID) is the frequency response of the spins. Since each spin sits not only in the external field $\vec{H}_0$ but also in the small magnetic field $\vec{H}_{loc}$ of its neighbors, there is a small distribution of the local fields ΔH_{loc} experienced by the individual nuclei, and the resonance frequency ω_0 is therefore broadened to a finite width $\Delta\omega = \gamma \Delta H_{loc}$ by the same spin-spin interactions which cause the decay of the transverse magnetization. Because of the Fourier relation, $\Delta\omega = 1 / T_2$.

The line can be further broadened if the DC magnetic field $\vec{H}_0$ is not uniform but has a distribution of width ΔH_0. As each spin precesses at its own Larmor frequency, it becomes progressively out of phase with its neighbors and destructive interference averages the transverse magnetization to zero.

However, this broadening can be deconvolved from the intrinsic line width by the

method of *spin echoes*, first demonstrated by Hahn,[60] and later developed by Carr and Purcell.[61] Let us imagine that we have used $\vec{H}_1$ to rotate $\langle \vec{M} \rangle$ to $\hat{y}'$, and that the individual spins are starting to dephase, as shown in Figure 4a. After a time τ, we apply another pulse of RF energy, so as to rotate the spins about $\hat{x}'$ by 180°. Now the slower spins are ahead in phase, and the faster ones are behind, as shown in Figure 4b. As long as the spins have not diffused in a time τ to regions of different local field, the dephasing process is completely reversed, and at time 2τ the signal is precisely reconstructed to form the spin echo, with the spins lined up along $-\hat{y}'$. The amplitude of the echo will be less than that of the initial FID only to the extent that spin-spin interactions have caused an intrinsic decay in the phase correlations amongst the spins. Thus if we measure the amplitude of the spin echo as a function of τ, we can trace out the shape which the FID would possess in the absence of field inhomogeneity. The Carr-Purcell modification is a pulse sequence with a 90° pulse at time t=0 and 180° pulses at times $t = \tau, 3\tau, 5\tau, \cdots$. Spin echoes occur at $t = 2\tau, 4\tau, \cdots$. The Carr-Purcell pulse sequence was not used in this experiment because the H_1 inhomogeneities due to the presence of Grafoil in the cell result in cumulative errors in such repetitive pulse sequences.

Because it is impossible to detect the longitudinal relaxation directly, a sequence of pulses is necessary to measure T_1 as well. First a 90° pulse is applied to flip the magnetization into the transverse plane. The transverse magnetization decays in a short time because of the DC field inhomogeneity, leaving $\langle \vec{M} \rangle = 0$. The longitudinal magnetization is then allowed to grow back toward its equilibrium value M_0 for a period τ, after which we flip the magnetization back into the transverse plane with another 90° pulse and observe its amplitude. By varying τ, we can sample the recovery of the magnetization as a function of time. This experiment is referred to as *saturation recovery*. A similar measurement can be made replacing the initial 90° pulse with a 180° pulse; then the magnetization recovers from $-M_0$ to M_0. This *inversion recovery* method was not used in this experiment for the reason that it takes more time when T_1 is long.

Figure 4. *Method of spin echoes*

a. Spins dephasing from $\hat{y}'$

b. Spins are reversed, now refocussing on $-\hat{y}'$

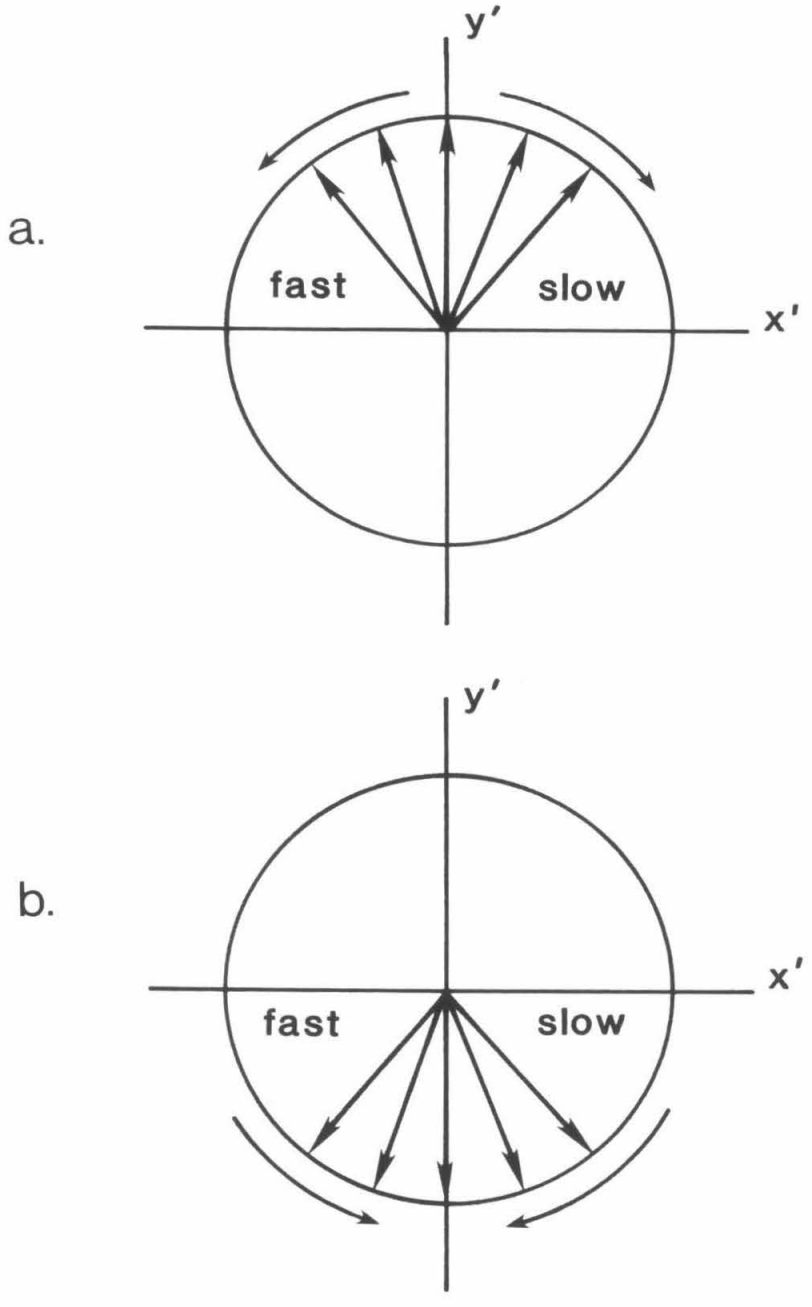

§2.5 Motional narrowing

The interaction terms in the Hamiltonian will contain terms coupling the spins to such degrees of freedom in the lattice as molecular translation and rotation. When the power spectrum of the lattice motions contain appreciable components at the Larmor frequency, the transfer of energy is most efficient, for then the local magnetic fields seen by the spins fluctuate at the resonance frequency. There will thus be a minimum in T_1 when the correlation time for molecular motion τ_c satisfies $\tau_c\ \omega_0 = 1$, as shown in Figure 5. Often the correlation time is determined by a thermally activated process, so that $\tau_c \sim \exp(-E / k_B T)$, where E is the energy barrier inhibiting the process.

The spin-spin interactions, on the other hand, are significant even when the lattice is rigid, for then each spin cannot escape the field $\vec{H}_{loc}$ of its neighbors. Motions in the lattice only weaken the spin-spin coupling. When the spectrum of thermal motions lies well above the Larmor frequency (as it typically does in liquids), the fluctuating local magnetic fields are effectively averaged to zero over a Larmor period, and the line is said to be *motionally narrowed*. In the regime of extreme motional narrowing, $T_2 \simeq T_1$ (T_2 cannot be greater than T_1, for the longitudinal magnetization cannot grow back to its equilibrium value before the transverse magnetization has decayed away). Typical behavior for T_2 is also shown in Figure 5.

NMR can thus be used as a diagnostic of phase transitions in the lattice, for the values of T_1 and T_2 depend on the dynamics of molecular motion, as we have described.

Figure 5. *Typical dependence of T_1 and T_2 on correlation time τ_c for lattice motions*

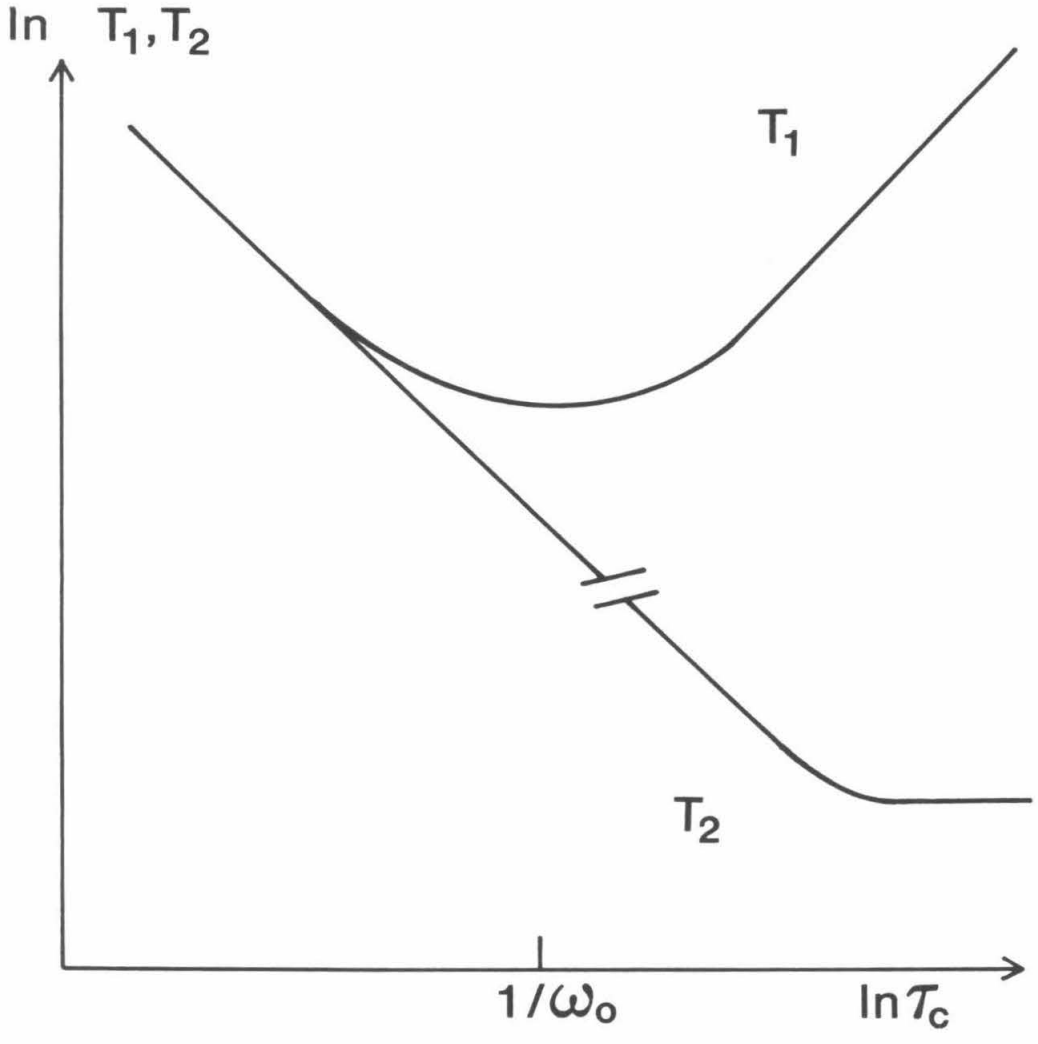

Chapter 3

Thermodynamics of Films

In a bulk medium, the surface is such a small part of the material that edge effects are ordinarily negligible. However, when the medium is condensed in the form of a film, the surface tension can form an appreciable fraction of the total free energy. (Indeed, we can picture the adsorbed film as being merely a modification of the substrate surface, so that the whole free energy of the film is nothing but a change in the substrate surface tension.) Thus, we shall wish to distinguish between free energies associated with the presence of interfaces, and modifications of the free energy due to changes in the microscopic internal behavior of the adsorbed medium. In this chapter we shall calculate the former.

§3.1 The Landau potential

In what follows, it will be convenient to use, for our free energy, the Landau potential Ω, related to the Helmholtz free energy F by $\Omega(\mu, T, V; A) = F(N, T, V; A) - \mu N$, where the proper thermodynamic variables for each function (chemical potential μ, number of molecules N, temperature T, volume V and surface area A) are shown. The reason for choosing Ω is that the film is free to exchange molecules with its co-existing vapor, so that the number in the film $N_2 = N - p\,V / k_B\,T$ is not a convenient variable. On the other hand, the chemical potential of the film is necessarily equal to that of the gas, independent of the distribution of matter in the cell. Note that in order to be consistent with the Gibbs construction, N_2 is defined as the *surface excess*, i.e., the difference between the total number of molecules in the cell and the number of gas molecules $N_g = p\,V / k_B\,T$ which would occupy the cell volume, including the volume occupied by the film, at the same temperature and pressure.

Since for a homogeneous bulk phase $\Omega = -p\,V$, we can define the surface excess Landau potential to be $\Omega_2(\mu, T, A) = \Omega(\mu, T, V; A) + p\,V$. Since the substrate area A is a fixed quantity, we shall drop all further reference to the dependence of Ω_2 on this one

of its proper variables.

§3.2 Homogeneous phases

Suppose that the surface is covered by a film of some phase, solid or liquid, denoted by i; and that the film can be pictured as an incompressible bulk continuum phase. Then the surface excess density, or *coverage*, is $n_2 = N_2/A = (\rho_i - \rho_g)\, z_i$, where z_i is the film thickness, ρ_i is the number density of phase i, and ρ_g is a small correction, neglected for the rest of this section, which accounts for the displaced gas. To construct Ω_2^i for phase i, we need the equation of state for the film. For thick films, we can use the Frenkel-Halsey-Hill (FHH) isotherm,[62] $\mu - \mu_i(T) = -\Delta C_3^{i\omega} / {z_i}^3$. Here, $\mu_i(T)$ is the chemical potential for co-existence of the bulk phase i with its vapor, and $\Delta C_3^{i\omega} = C_3^{(\omega)} - C_3^{(i)}$, the difference between the coefficients of the van der Waals potentials of a half space of substrate and adsorbate, respectively. The usual justification of the FHH equation is given in Appendix III; an alternative derivation will be found in Section 3.4 below.

Now we have

$$\frac{\Omega_2^i}{A} = -\int_{-\infty}^{\mu} n_2(\mu', T)\, d\mu' = -\int_0^{n_2} n_2' \frac{d(\mu - \mu_i)}{dn_2'} dn_2',$$

where the integration is performed at constant T. The FHH equation is not valid at the lower limit, but we can write $\sigma_{i\omega} + \sigma_{ig} = -\int_0^{\infty} n_2' \frac{d(\mu - \mu_i)}{dn_2'} dn_2'$, where the σ's are the surface tensions of the bulk phase with the substrate and the vapor, respectively. Then[63] $\Omega_2^i / A = \int_{n_2}^{\infty} n_2' \frac{d(\mu - \mu_i)}{dn_2'} dn_2' + \sigma_{i\omega} + \sigma_{ig}$. Thus,

$$\frac{\Omega_2^i}{A} = \frac{3}{2} \frac{\rho_i \Delta C_3^{i\omega}}{{z_i}^2} + \sigma_{i\omega} + \sigma_{ig}, \tag{1}$$

or in terms of its proper variables,

$$\frac{\Omega_2^i}{A} = \frac{3}{2}\rho_i\,(\Delta C_3^{i\omega})^{1/3}(\mu_i(T)-\mu)^{2/3}+\sigma_{i\omega}+\sigma_{ig}$$

as we have shown in Ref. (52) (where, however, we neglected the small distinction between $\Delta C_3^{l\omega}$ and $\Delta C_3^{s\omega}$). The quantity Ω_2^i/A is the negative of the spreading pressure of the film. We shall discuss the physical significance of this equation further in Section 3.4.

§3.3 Triple point dewetting

Let us consider the possibility of equilibrium between two homogeneous phases. A film can melt if $\Omega_2^s = \Omega_2^l$; hence the co-existence curve is defined by:

$$\rho_s\,(\Delta C_3^{s\omega})^{1/3}\,(\mu_s(T)-\mu)^{2/3} - \rho_l\,(\Delta C_3^{l\omega})^{1/3}\,(\mu_l(T)-\mu)^{2/3} = -\frac{2}{3}\delta,$$

where δ is the difference of surface tensions, $\delta = \sigma_{sg}+\sigma_{s\omega}-\sigma_{lg}-\sigma_{l\omega}$. Pandit and Fisher[22] point out that in general one expects $\delta \neq 0$. Hence (for $\delta > 0$) the melting curve intersects the bulk solid co-existence curve at a temperature

$$T_W = T_t - \frac{1}{\alpha}\left[\frac{2}{3}\,\frac{\delta}{\rho_l\,(\Delta C_3^{l\omega})^{1/3}}\right]^{3/2},$$

and with a slope $d(\mu_s-\mu)/dT \propto (T_W - T)^{1/2}$, where α is the difference in slopes $\alpha = (d\mu_s/dT - d\mu_l/dT)\,|_{T_t}$ and is related to the bulk latent heat of melting per molecule L by $\alpha \simeq L/T_t$. Thus, for $\delta > 0$, the surface tension favors stability of the liquid phase below T_t. Furthermore, between T_W and T_t, a liquid film can co-exist with bulk solid, but not with a solid film. Hence a film passing through T_W must convert any film in the solid phase into bulk crystallites—a dewetting transition. Finally, the asymptotic tangency of the melting curve to the sublimation curve, together with FHH, implies that for a film of coverage n_2, the temperature at which melting begins obeys $(T_W - T) \propto 1/n_2^2$.

Typically experiments are done under approximately *isosteric* conditions (constant coverage). Then, if we heat a film through the melting transition, just as for three-dimensional melting done at constant volume, the film must pass through a two-phase co-existence region of finite width in temperature, as shown in Figure 6 for two different film thicknesses. For the thinner of the two, an isostere in the μ–T plane encounters the melting curve as T is raised, follows it until all the solid film is melted, then breaks off into the liquid film region. In the two-phase region we must supply enough heat to cause conversion of solid to liquid, and hence the heat capacity of the film will show the mesa-like shape seen in the figure. For the thicker film, the isostere follows the melting curve until it encounters bulk co-existence at T_W. As it does so, we must supply heat to convert to bulk crystallites whatever portion of the film is in the solid phase. Using the asymptotic form for the melting curve at T_W, we find that for such thick films the heat capacity must vary as $C \propto (T_W - T)^{-1/2}$, resulting in a spike in the middle of the mesa for such thick films.

The results of a heat capacity experiment of M. Lysek[52] on thick films of methane on graphite are in agreement with this model: the heat of conversion is observed at T_W, where $T_W < T_t$, as seen in Figure 7, and the onset of melting obeys the asymptotic form $T_W - T \propto n_2^{-2}$, according to the data shown in Figure 8. It is found that $T_t - T_W = .18$ K. The value found for ΔC_3 is 1.4×10^4 K$\mathring{A}^3$; compared to the theoretical prediction $\Delta C_3^{l\omega} \simeq \Delta C_3^{s\omega} \simeq 1.2\times10^4$ K$\mathring{A}^3$ from Appendix III, the agreement is not bad, especially considering that only the cube root of the parameter appears in the model. The resulting phase diagram is given in the inset to Figure 6.

It is a consequence of thermodynamics that any transition between a wetting phase and a non-wetting phase must meet the bulk co-existence curve tangentially.[64] We shall use the melting transition to illustrate our proof. Let us consider a box of volume V in contact with a particle bath at chemical potential μ and a heat bath at temperature T. This box has two phases: $i = 1$, solid film plus vapor, and $i = 2$, liquid film plus vapor.

Figure 6. *Triple point dewetting, phase diagram and heat capacities. Theoretical isosteric specific heat for 6.5 and 18.3 layers. Inset shows corresponding isosteric trajectories in the μ–T plane (dotted lines), bulk phase boundaries (solid lines), and melting curve (dashed line).*

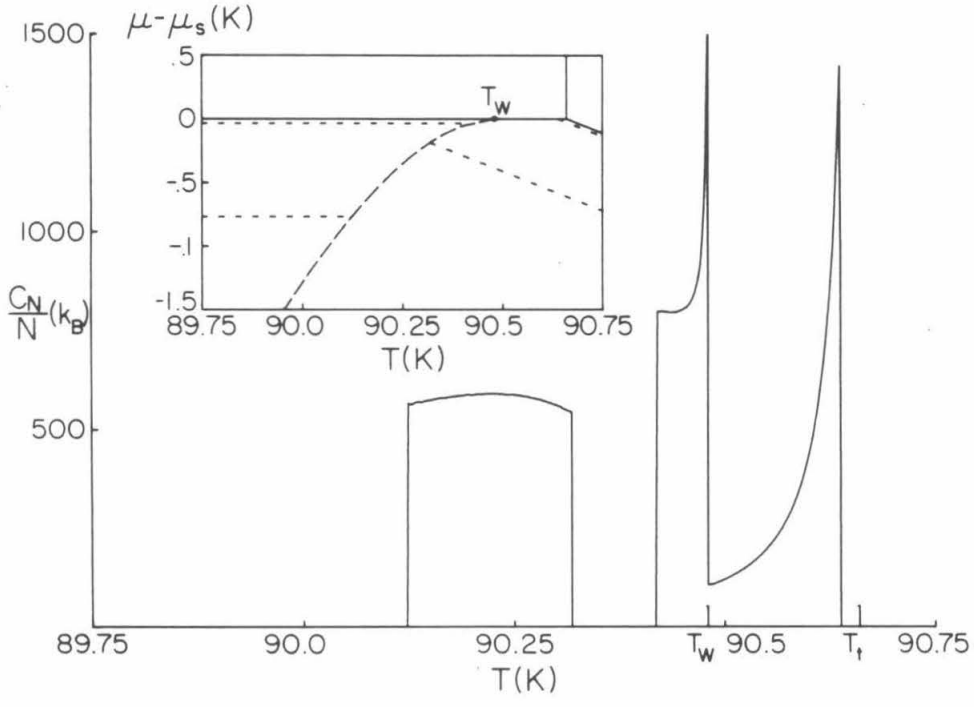

Figure 7. *Experimental heat capacities for film thicknesses of 18.3, 14.1, 9.3, 6.5 and 5.0 layers (top to bottom). Inset shows features of 18.3 layer curve identified as onset of melting, dewetting, and completion of melting.*

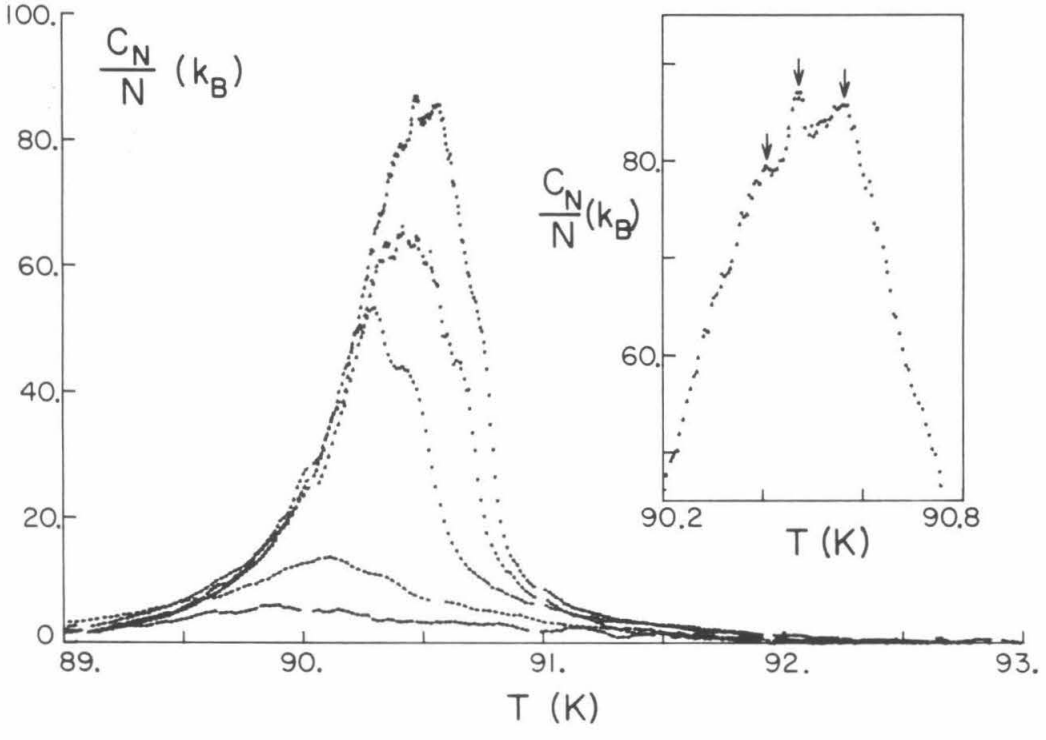

Figure 8. *Onset temperature of melting as a function of film thickness (circles); diamonds indicate temperature of wetting spike for 18.3 and 14.1 layer films.*

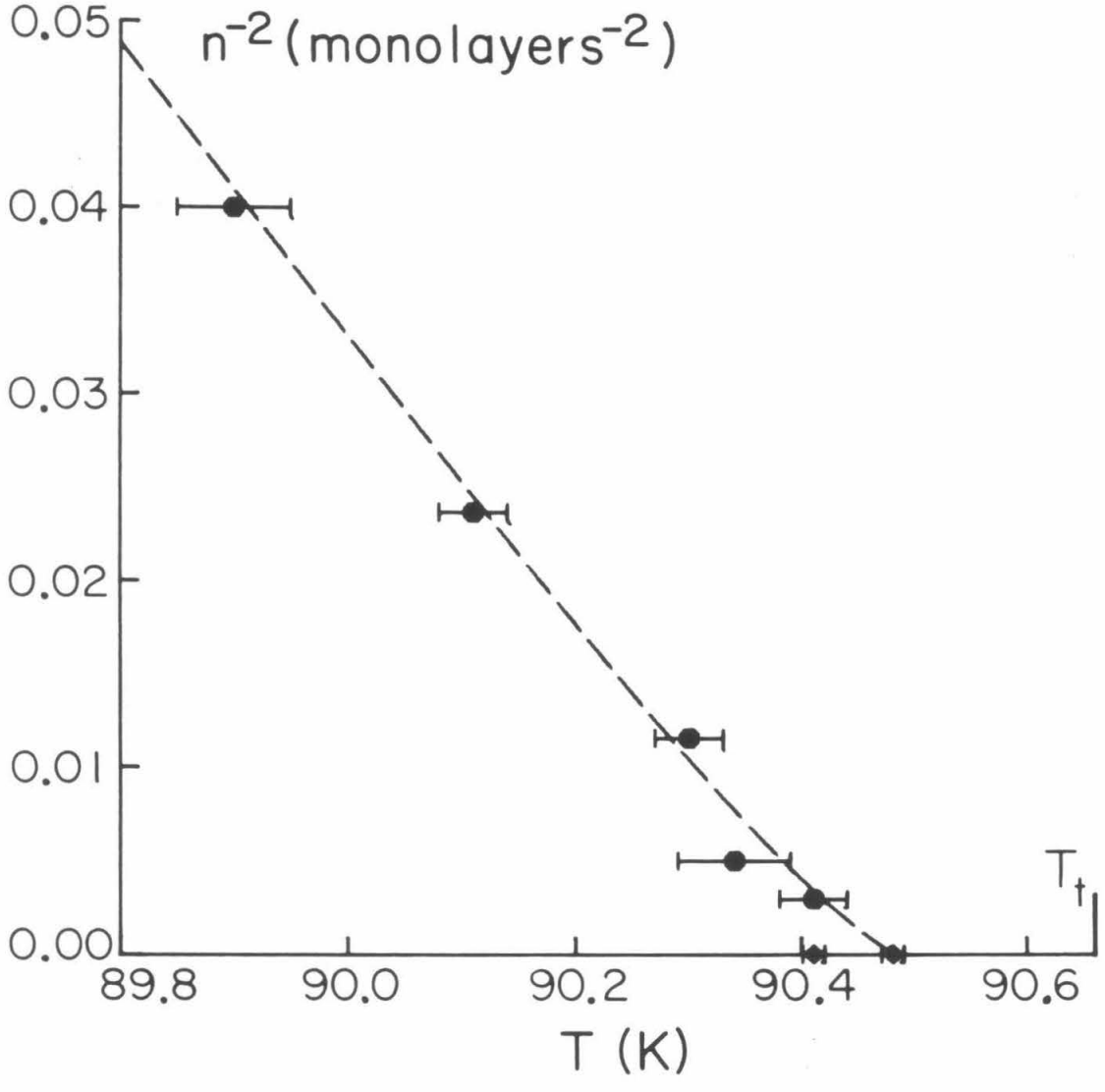

For each phase, we have $d\Omega_i = -S_i\, dT - N_i\, d\mu$, where S and N are the total entropy and particle number of the box; and so the transition between the two phases obeys $d\Omega_1 = d\Omega_2$, or $d\mu/dT = -(S_1 - S_2)/(N_1 - N_2)$, the analogue of the Clausius-Clapeyron equation for the variables μ and T. Now let us follow the transition close to the bulk co-existence curve. Then in phase 1, the solid can fill nearly all of V, while in phase 2 the liquid can only take up a tiny fraction of the volume. In the thermodynamic limit, $(S_1, N_1) \to (S_s, N_s)$ and $(S_2, N_2) \to (S_g, N_g)$, where the subscripts s and g refer to solid and gas. Thus,

$$\lim_{\mu \to \mu_s} (d\mu/dT)_{melting} = -(S_g - S_s)/(N_g - N_s),$$

which is equal to the slope of the bulk sublimation curve.

§3.4 Surface melting

There is a third possible phase which we have not yet considered, namely a stratified phase where the lower layers of the film are solid, and the upper ones liquid. This is the film analogue of surface melting of the bulk, as we described in Section 1.4. We might expect this phenomenon to occur since the bottom layers are under great pressure due to the van der Waals forces: this argument, however, is false; for we shall see that position of the liquid-solid interface can be quite far from the substrate.

Thermodynamically, the idea is that if $\sigma_{sg} \geq \sigma_{sl} + \sigma_{lg}$, then the liquid wets the solid; and near the triple point, where Ω_s and Ω_l are close, the extra energy cost $\Omega_l - \Omega_s$ of making a thin layer of liquid at the surface may be more than compensated for by the decrease in surface tension. Then as T_t is approached from below, the energy cost $\Omega_l - \Omega_s$ decreases, and the surface layer of liquid will grow, until at T_t it consumes the solid. Then the solid can be said to melt from the surface downward. It is not required that $\Omega_l = \Omega_s$, as is the case for bulk melting, which occurs only at extremely high pressures for temperatures away from T_t.

We need an equation of state for the surface melted phase in order to proceed. The usual prescription[27] is to say that the liquid surface layer is a property of the solid surface. So the thickness of the solid is governed by the FHH equation for solid on adsorbate. Now the liquid can also be described as a film growing on the solid, so it too can be described by the FHH equation with the appropriate coefficient. This model results in a heat capacity of the form $C_N \sim (T_t - T)^{-4/3}$ and a downward shift in peak temperature T_p from T_t that depends on film thickness as $(T_t - T_p) \propto {n_2}^{-3}$. Both of these predictions, we note, are violated by the heat capacity data for methane on graphite.[52]

The model we have just described, however, neglects the interaction of the substrate with the liquid phase. We shall show that the effect is crucial, and allows an underlayer of solid to be stabilized above T_t just as the solid surface stabilizes a layer of liquid below T_t. Thus an adsorbed film, unlike bulk material, can display surface melting effects on both sides of the triple point.

We consider the following alternative procedure, adapting the method of de Gennes[65] to surface melted films. We wish to add up all the excess free energy in the system due to the fact that it is inhomogeneous, given the assumption that the medium is at each point locally bulk-like and in equilibrium. One contribution to this energy arises from the presence of condensed phases in the region of the phase diagram where the state of lowest free energy is the vapor. Since the Gibbs free energy per particle is equal to the chemical potential, the extra energy cost of forming the wrong phase may be written $\mu_i(T) - \mu$, where $\mu_i(T)$ is the chemical potential of the bulk phase i at co-existence, as above. Each molecule in the system in addition feels a potential $\Delta\phi(\vec{r})$, where the external field $\Delta\phi$ is the perturbation of the local van der Waals potential due to the fact that far away the medium is replaced by some other phase (or substrate). The sum over molecules is converted to an integral over space by a factor of the local density. Thus, the total potential energy per area is

$$W = \frac{1}{A} \int_{all\ space} dV \rho_i \Delta\phi(\vec{r}). \tag{2}$$

We shall compute the integral for a stratified medium, so that the problem is one-dimensional. If two points in the medium are attracted by a $1/r^6$ van der Waals potential, then the potential per area between two slabs separated by a distance z is proportional to $f(z) = -1/z^4$ for large z. The coefficient of the slab interaction is related to the potential $-C_3^{(2)}/z^3$ for a single molecule of phase 1 over a surface of medium 2 by taking the limit as the density of medium 1 goes to zero, and integrating over z to make a half space of medium 2. The coefficient is found to be $3\rho_1 C_3^{(2)}$.

At the end of our calculation we must have no terms which depend on $f(z)$ for small z. However, when we compute the integral in Eq. (2) for two half spaces of media 1 and 2 in contact, we find a surface energy W_{12} proportional to $\int_0^\infty dz' \int_{z'}^\infty dz'' f(z'')$, which we identify as the surface tension σ_{12}. We must take the surface tension as an empirical parameter.

Next, we solve Eq. (2) for the case that there is a slab of thickness z_2 of medium 2 sandwiched between half spaces of media 1 and 3. We find $W = W_{12} + W_{23} + W_{123}$, where W_{123} is an excess free energy per area given by

$$W_{123}(z_2) = -3(\rho_1 - \rho_2)(C_3^{(2)} - C_3^{(3)}) \int_{z_2}^\infty dz' \int_{z'}^\infty dz'' f(z''). \tag{3}$$

This W_{123} is the energy of interaction between surfaces (1,2) and (2,3). Note that W_{123} vanishes as it should if any two of the media are identical. An interesting result is obtained for the case that phases 1, 2 and 3 are the vapor, liquid and solid, respectively, of the same material. The denser the medium, the more powerful its van der Waals potential, so if $\rho_s > \rho_l$ then W_{123} is positive and the interfaces repel. That is, the surface free energy is reduced by growing a layer of an intermediate phase. If $\rho_s < \rho_l$, then surface melting is energetically unfavorable, for the interfaces will collapse together. This argument implies that for substances such as water and germanium (both of which have

$\rho_s < \rho_l$ and are said to show surface melting in the bulk[66]), the surface melted layer cannot grow to infinite thickness at the triple point. This result is a special case of the general property that interfaces do not like to be infinitely sharp, but prefer to reduce their energy by relaxing their density profile.

How does this model compare with the results of Section 3.2? We have

$$\frac{\Omega_2^i}{A} = \sigma_{i\omega} + \sigma_{ig} + W_{123}(z_2) - (\mu - \mu_i(T))\, n_2, \tag{4}$$

where the last term represents the free energy cost of forming the phase i; and of course the surface excess is $n_2 = (\rho_i - \rho_g)\, z_2$. To get the Landau potential in terms of its proper variables, we impose on Eq. (4) the thermodynamic identity $\partial\Omega_2/\partial\mu|_T = -n_2$; the result proves to be the FHH isotherm. Substituting back in to Eq. (4) then shows that it is identical to Eq. (1). This confirms our confidence in our procedure, and we now calculate the equation of state for a surface melted film.

When we compute the Landau potential for a system of four media (substrate, solid, liquid, vapor), a new term arises, W_{1234}, which is a three-body interaction amongst the surfaces: thus $W = W_{12} + W_{23} + W_{34} + W_{123} + W_{234} + W_{1234}$, where

$$W_{1234}(z_2, z_3) = -3\,(\rho_1 - \rho_2)\,(C_3^{(3)} - C_3^{(4)}) \int_{z_2+z_3}^{\infty} dz' \int_{z'}^{\infty} dz''\, f(z''),$$

where z_2 and z_3 are the thicknesses of the layers of media 2 and 3. This form could almost have been guessed, since we must have $W_{1234} = 0$ if media 1 and 2 or media 3 and 4 are the same, and $W_{1234} = W_{124}$ if medium 2 equals medium 3.

Adding up all the terms, including the free energy costs for forming the wrong phases, for our special case of surface melting we have

$$\frac{\Omega_2^{sm}}{A} = (\rho_s - \rho_l)\frac{\Delta C_3^{s\omega}}{2 z_s{}^2} + \rho_l \frac{\Delta C_3^{ls}}{2 z_l{}^2} + \rho_l \frac{\Delta C_3^{s\omega}}{2 (z_s + z_l)^2}$$

$$- \rho_l (\mu - \mu_l(T)) z_l - \rho_s (\mu - \mu_s(T)) z_s + \sigma_{s\omega} + \sigma_{sl} + \sigma_{lg}$$

where here and henceforth we are subsuming the terms ρ_g into reduced volumes $\rho_i \to \rho_i - \rho_g$. The simplest way to turn Ω_2^{sm} into an equation of state is to observe that the equilibrium values of z_l and z_s will minimize Ω_2^{sm} for fixed μ. (To prove this, one must treat the solid and liquid as distinct species with separate chemical potentials μ' and μ''. One imposes first the condition $\partial\Omega_2/\partial\mu|_T = -n_2$ for each species and then that the chemical potentials are equal: $\mu' = \mu'' = \mu$.) The resulting coupled equations relate (z_l, z_s) to (μ, T):

$$\rho_l (\mu - \mu_l(T)) = -\rho_l \left[\frac{\Delta C_3^{ls}}{z_l{}^3} + \frac{\Delta C_3^{s\omega}}{(z_s + z_l)^3} \right] \tag{5a}$$

$$\rho_s (\mu - \mu_s(T)) = -\left[(\rho_s - \rho_l)\frac{\Delta C_3^{s\omega}}{z_s{}^3} + \rho_l \frac{\Delta C_3^{s\omega}}{(z_s + z_l)^3} \right] \tag{5b}$$

Now Ω_2^{sm} simplifies to

$$\frac{\Omega_2^{sm}}{A} = \frac{3}{2}\left[(\rho_s - \rho_l)\frac{\Delta C_3^{s\omega}}{z_s{}^2} + \rho_l \frac{\Delta C_3^{ls}}{z_l{}^2} + \rho_l \frac{\Delta C_3^{s\omega}}{(z_s + z_l)^2} \right] + \sigma_{s\omega} + \sigma_{sl} + \sigma_{lg}$$

in perfect analogy to Eq. (1). To get Ω_2^{sm} in terms of its proper variables, Eqs. (5) must be solved numerically for z_l and z_s in terms of μ and T.

§3.5 Experimental consequences of surface melting

The heat capacity signature of surface melting is a smooth peak, for when Eqs. (5) are solved for (z_l, z_s) as a function of T with $n_2 = \rho_l z_l + \rho_s z_s$ held constant, the result is that the position of the liquid-solid interface moves smoothly through the film. When the

interface is moving most rapidly, near the triple point, the heat required to convert solid to liquid is greatest. Indeed, the free energy terms $1/z_l^2$ and $1/z_s^2$ prevent the film from ever becoming totally homogeneous in this model, and a small amount of the wrong phase remains even when the temperature is far from T_t. For very thin films, the solid-liquid interface is effectively pinned, and the transition can be extremely broad (and the heat capacity correspondingly suppressed). The resulting isosteric heat capacities are shown in Figure 9. The power law $C_N \sim (T_t - T)^{-4/3}$ derived from the simpler model described at the beginning of this section is clearly not correct; however it turns out to be a good approximation for thick films that $C_N \sim (T_p - T)^{-4/3}$ below T_p, where T_p is the temperature of the heat capacity peak, and T_p approaches T_t in the thick film limit.

Because z_l and z_s appear in Eqs. (5) only in terms of degree –3, the solutions scale, so that the peak of the heat capacity curve varies with thickness as $T_t - T_p \propto n_2^{-3}$, in contradistinction to the exponent of –2 we found for triple point dewetting. A priori calculations using the coefficients from Appendix III indicate that the peak temperature for methane on graphite would be shifted slightly *upward* from T_t, if the system exhibited surface melting.

Bienfait et al.[30] claim to have observed surface melting of methane on MgO. However, as we have seen, surface melting in films is strongly dependent on the substrate. Furthermore, the experiments of Pluis et al.[67] on Pb show that surface melting can vary as a function of crystal face for a given substance. If, as they argue, the (100) surface is more likely to surface melt than the (111) surface, it may give an additional reason for the difference between the MgO and graphite experiments, for MgO is square co-ordinated and graphite is hexagonal, so methane should grow in different orientations on the two substrates.[45]

Finally, we address the question of whether or not the surface melted phase is stable with respect to the formation of homogeneous phases. We solve $\Omega_2^{sm} = \Omega_2^s$ or $\Omega_2^{sm} = \Omega_2^l$. The results will depend on two parameters, $\delta = \sigma_{sg} + \sigma_{s\omega} - \sigma_{lg} - \sigma_{l\omega}$ and

Figure 9. *Heat capacity signal of surface melting for coverages of 10, 8, 6, 4 and 2 layers (top to bottom).*

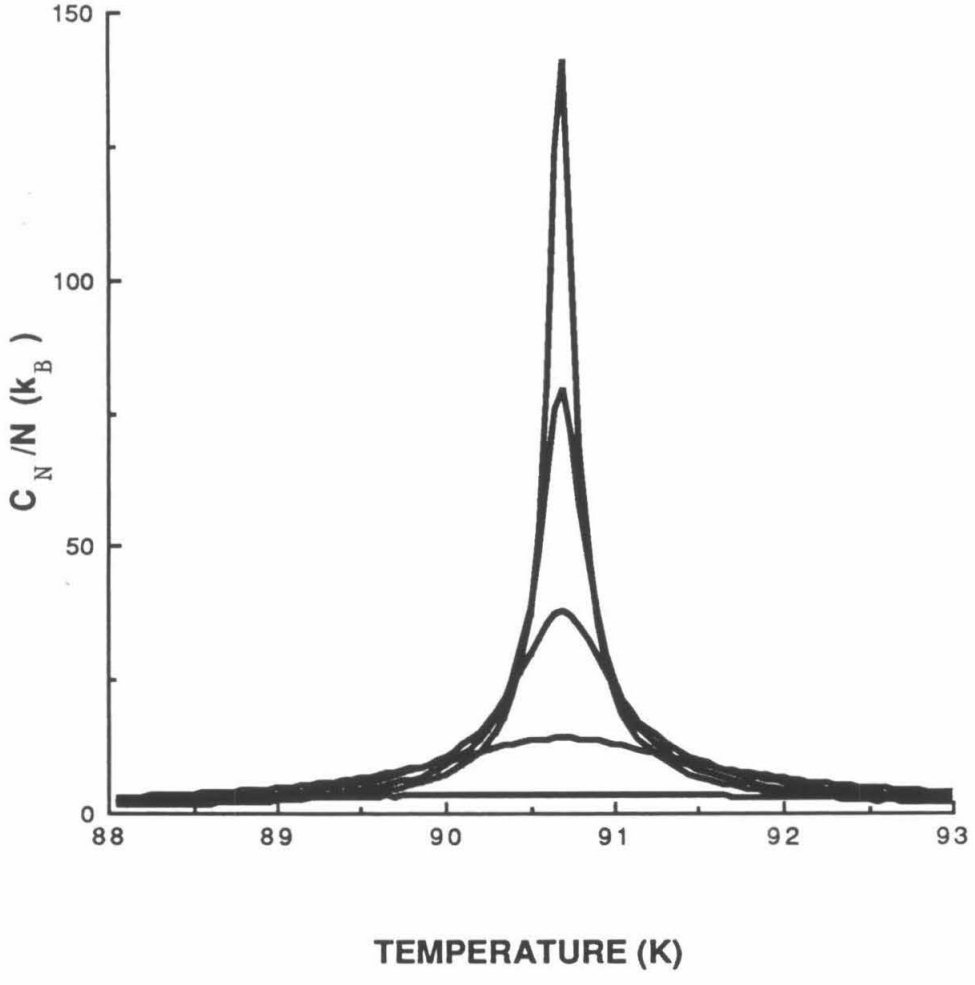

$\delta' = \sigma_{sg} - \sigma_{lg} - \sigma_{sl}$.

The following general rules determine the topology of the phase diagram (for $\rho_s > \rho_l$). The sign of δ' governs whether the transition between solid and surface melted phases occurs above or below the triple point; and $\delta - \delta'$, between liquid and surface melted phases. If $\delta > 0$ and $(\Delta C_3^{ls}/\Delta C_3^{l\omega})^{1/3}\delta > \delta'$, or $\delta < 0$ and $[(1-\rho_l/\rho_s)^{1/3} - 1]\,|\delta| > \delta'$, then surface melting is suppressed, and the sign of δ determines the location of the solid-liquid transition, as in Section 3.3. For $\delta = .21$ K/Å^2 and $\delta' = 0$, the surface melted phase is never stable and the resulting phase diagram is the same as that of Figure 6. Figure 10 shows phase diagrams for other values of δ and δ'. In Figure 10a, the surface melted phase is allowed both above and below T_t, and there is no dewetting transition. There would be a heat capacity signal on entering or leaving the surface melted region, however. In Figure 10b, surface melting occurs only below T_t, and there is a dewetting transition from the surface melted phase to the liquid phase. Phase diagrams like those of Figures 10a and b were also proposed by Pandit and Fisher.[22] Otherwise, however, the possibility of a first order transition from the surface melted phase to a homogeneous phase does not appear to have been fully appreciated. The surface melted state is never favored for very thin films, because of the high energy cost of the repulsion between the interfaces. Thus if surface melting occurs there must be a triple point between the solid, liquid and surface melted phases. However, for such thin films the bulk continuum picture of a liquid atop a solid may not be valid anyhow.

Figure 10. *Surface melting phase diagrams*

a. $\delta = .4K\mathring{A}^{-2}$, $\delta' = .75K\mathring{A}^{-2}$

b. $\delta = 2K\mathring{A}^{-2}$, $\delta' = 1.43K\mathring{A}^{-2}$

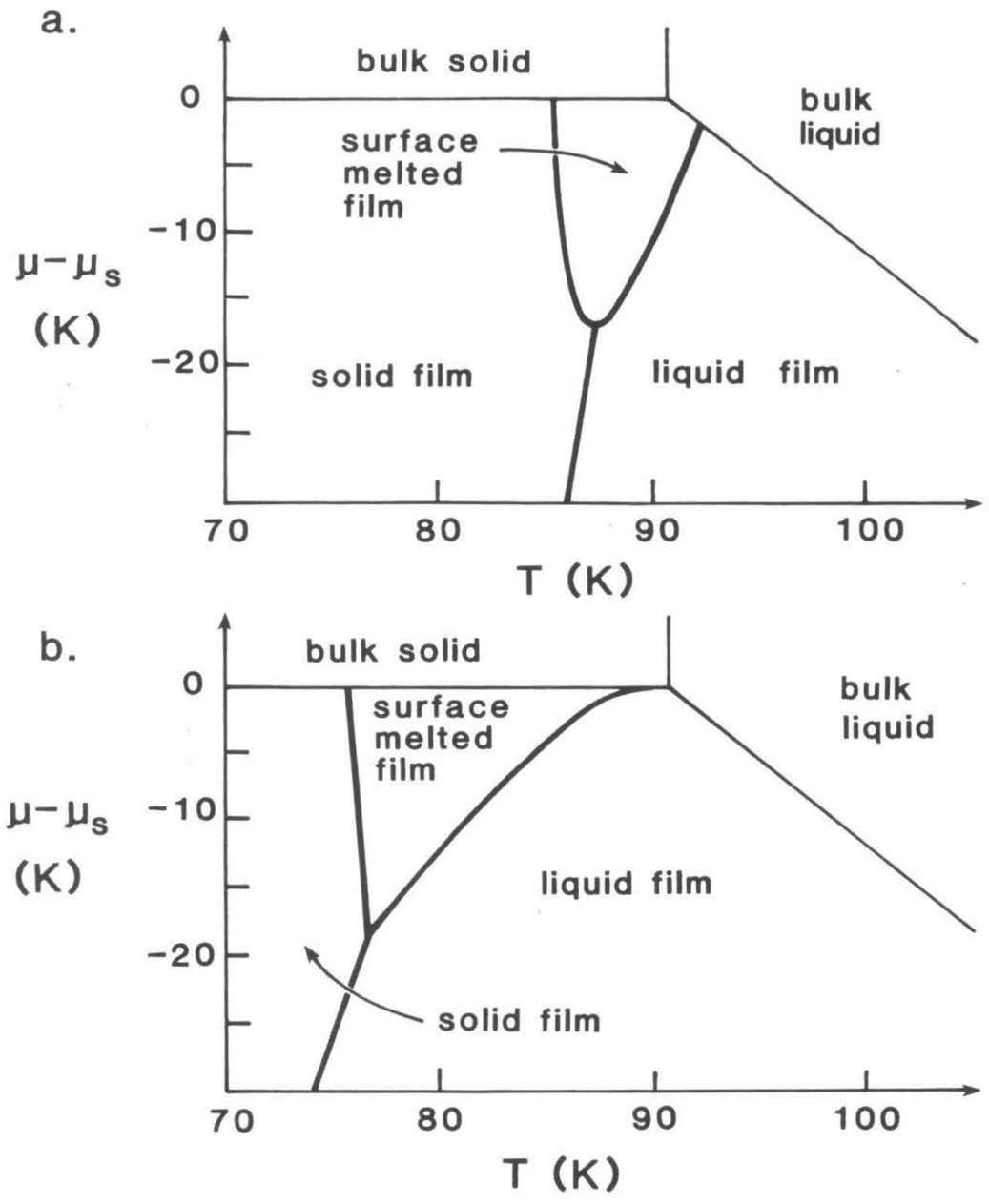

Chapter 4

Experimental Design and Method

The experimental apparatus was constituted of three component systems: vacuum, cryogenic, and RF; the first two to control the independent variables of coverage and temperature, and the third, a complete pulsed NMR spectrometer. This chapter will describe the construction of the apparatus, the operating procedures, and the method of data analysis.

§4.1 The cell

The cell in the present experiment contained 1.398 g of Grafoil. In order to remove residual impurities left from the manufacturing process, the Grafoil was heated to 800°C (as determined by a Chromel-Alumel thermocouple), under $< 10^{-5}$ mbar vacuum for 10.5 hours[68] before being transferred in the atmosphere to a Pyrex cell. Glass was chosen for the cell material because it is non-magnetic, non-conductive and contains no hydrogen to interfere with the NMR signal. It was joined to the 3/16" stainless steel fill line via a Housekeeper (Pyrex/Cu) seal. The more robust glass/Kovar seal was not used because Kovar is magnetic. A metal-gasket vacuum fitting above the Housekeeper seal made the cell demountable. For experiments on bulk methane, the cell was replaced by one without Grafoil. The fill line terminated in a vacuum valve. After the cell was mounted, it was heated in situ to 100°C under 10^{-5} mbar overnight to remove adsorbed air. The valve at the top made it possible to remove the probe from the system for repair or adjustment without further exposure of the surface to the atmosphere.

§4.2 Vacuum system

The gas handling system is depicted in Figure 11. It was composed entirely of metal, ¼" tubing of stainless steel and Cu, joined by metal-gasket fittings. The calibrated volume, V_0, was a stainless steel beaker with a lid welded to it. Its volume (2015 ± 1 cc) was measured by filling it with water and then measuring the volume of the water. The

Figure 11. *The gas handling system. Only one of two concentric dewars is shown*

V_0 = *calibrated volume* *IG = ion gauge*

CH_4 = *methane cylinder* ⊗ = *valve*

DP = diffusion pump

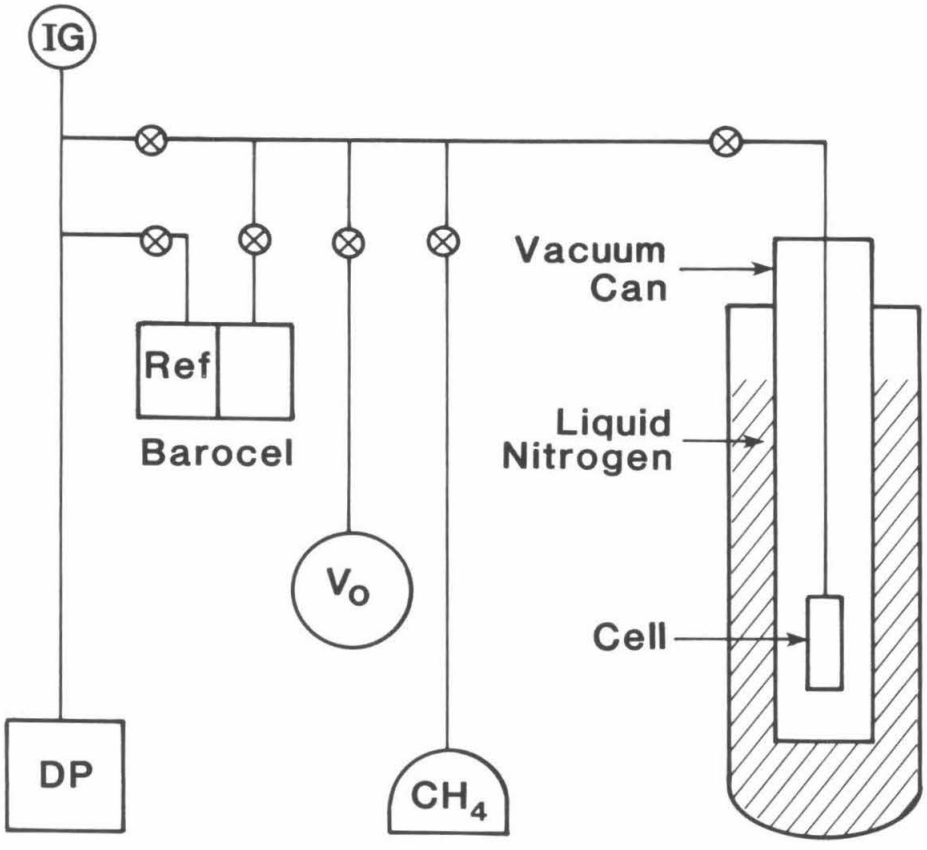

volumes of the rest of the system were measured by filling V_0 with helium gas, allowing the gas to expand into the other volumes, and measuring the change in pressure.

Pressures were measured using a Barocel electric capacitance manometer.* The instrument has a 4½ digit readout, with an accuracy of .1% ± .03 torr.

To know the total number of molecules of gas in any part of the system, it was necessary to know the temperature as well as the volume and pressure. Ambient temperature was read to .1°C from a mercury thermometer. Typically, the total error in measuring the amount of gas in the cell was .2 layers for films over 10 layers thick and .1 layers for films under 10 layers.

The diffusion pump was capable of reaching a pressure of 10^{-7} torr. The ion gauge was mounted near the diffusion pump, far from the cell, because the gas handling system was not dedicated to the present experiment, but shared. The ion gauge reading must therefore be considered merely diagnostic of the cell pressure.

The methane used was 99.99% and 99.999% pure, with an oxygen content of < 2 ppm.† It is very important to prevent contamination of the methane by O_2. Levels of 10 ppm are known to affect measurements of T_1 in methane.[69] To avoid the difficulty of ensuring oxygen-free conditions in a regulator valve, none was used. Instead, a 5 cm length of tubing just outside the cylinder valve was closed off with a vacuum valve. Filling this small section to the cylinder pressure allowed the metering of small quantities of gas into the manifold.

§4.3 Cryogenic system

The temperature range of experimental interest was determined by the triple point of methane, 90.66 K,[70] and the roughening temperature, 78 K.[26] These temperatures were easily attained with liquid nitrogen refrigerant. The only difficulty was to keep the

*Datametrics, sensor model 538H-12 and meter model 1174.
†Matheson Research grade and Alphagaz Research Plus grade, respectively.

cell the coldest part of the system accessible to the gas, to ensure that the methane condensed on the Grafoil and not in the fill tube.

The probe designed for this purpose is sketched in Figure 12. Two concentric dewars were used: the inner dewar was vacuum tight, and the vapor pressure could be regulated, so that the bath temperature could be lowered to the nitrogen triple point, 63 K. The probe was isolated from the bath by a vacuum can. To maintain the cell at a temperature above the bath, the cell was surrounded by an aluminum thermal shield wound with a 125 Ω Evanohm heater, as shown in Figure 12. A 250 Ω Manganin heater wire was wound on the fill tube to hold it above the cell temperature.

Exchange gas was maintained in the vacuum can, at a pressure between 20 and 100 μmHg, to provide a thermal link to the bath. At these pressures, the mean free path of particles in the gas is comparable to the dimension of the vacuum can, and the thermal conductivity of the gas is proportional to the pressure.[71] The heat link was thus a controllable parameter.

The fill tube had a diameter much smaller than the vacuum can, so the thermal contact between fill tube and bath was weak; but the thermal shield nearly touched the vacuum can, providing a good link to the bath. The heat flow in the probe was therefore mainly down the fill tube from room temperature, through the thermal shield to the bath, resulting in a monotonic temperature profile along the length of the probe. A simple model of the thermal profile along the probe, using experimentally determined parameters for the thermal conductivities and heat capacities of probe and exchange gas, was used to determine the allowable ranges for heater powers and exchange gas pressure. The high thermal conductivity of aluminum made the environment of the cell approximately isothermal, preventing cold spots from occurring at the Housekeeper seal, which was the narrowest point of the fill line (1/8"). Insofar as any temperature gradient was present in the shield, it varied in the right direction so that the cell was colder than the neck where the fill line passed through the thermal shield.

Figure 12. *Sketch of probe. Shading indicates location of heaters. Not to scale.*

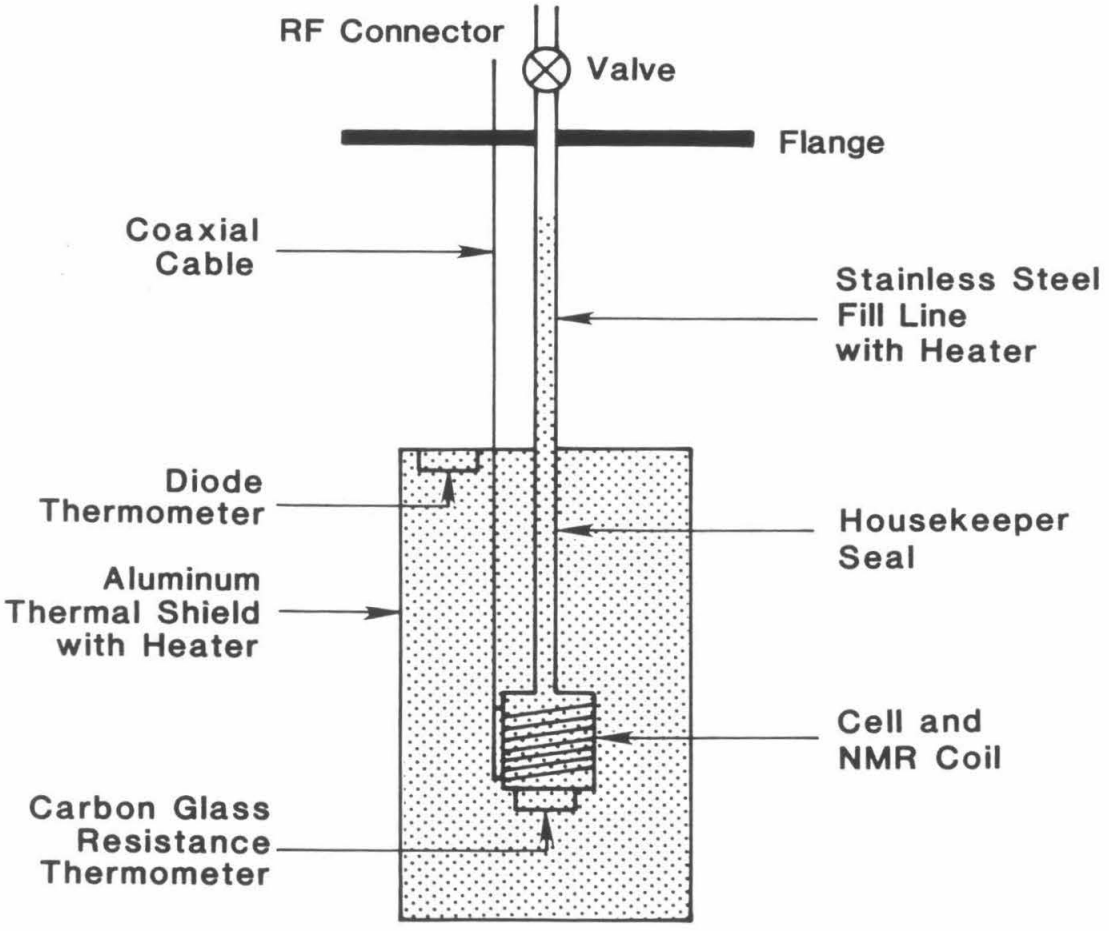

Temperature stability was maintained by controlling the power to the shield heater by feedback from a diode thermometer* fixed to the top of the shield. Other heat leaks such as that to the bath varied slowly with time (for example, as the bath level dropped), so stability was good.

The temperature of the cell differed from that of the shield, although it followed it. Cell temperature was independently measured by a carbon glass resistance (CGR) thermometer† fixed to the outside of the cell with GE7031 varnish. Carbon glass was chosen for the sensor because of its low magnetoresistance. At the fields in the present experiment, the error is negligible.[72]

Because Pyrex is a relatively poor thermal conductor, the thermometer may not always have reflected accurately the temperature of the contents of the cell. However, as we shall see below, when the temperature of the cell was allowed to drift up and down, the NMR data correlated with the reading of the thermometer within a degree, which gives an upper limit to the error due to thermal gradients across the cell wall.

A calibration of the thermometer was made against a Pt resistance thermometer, and the triple point of bulk methane as determined both by NMR and the bulk heat capacity. The last involved letting the shield temperature drift up and down through T_t; the latent heat of melting causes the rate of change of the temperature of the cell thermometer to slow at the onset of the transition. The results of all three calibrations agreed with the one provided by Lakeshore Cryogenics to within a few tenths of a degree. The absolute accuracy of our thermometry may thus be taken to be .2 K. The relative accuracy was .01 K.

The resistance of the CGR thermometer was measured with an active AC Kelvin bridge, based on a circuit developed by Rubin and Golahny.[73] The error signal was

*Lakeshore Cryogenics, model DT-470.
†Lakeshore Cryogenics, model CGR-1-2000.

detected by a lock-in amplifier,* digitized by a multimeter with an IEEE interface,† and logged by computer.

§4.4 RF electronics

A block diagram of the NMR spectrometer is shown in Figure 13. It is a single-coil transceiver based on a design by Clark.[74] We shall analyze the circuit by tracing the signal from left to right. Two pulse generators‡ are set to produce pulses of widths selected to produce tip angles of 90° and 180°. The computer, a PDP-11/34, also counts the pulses of the first pulse generator, which thus serves as a timing device. The software is capable of following pulse rates as high as 5 kHz, providing a limit to time resolution of 200 μsec, with an accuracy of .5%. This implies that T_2's shorter than .2 msec were below instrumental resolution using the method of spin echoes.

At each clock cycle, the computer can select one of the pulse generators. The gated pulses are used to control a solid-state RF switch,§ generating square pulses of 30 MHz RF from an oven-controlled crystal oscillator source,** with a frequency stability of 10^{-8} per day.

The RF pulses in turn are amplified to about 200 W by a gated transmitter amplifier.†† The pulses pass through a broadband tuned filter and series crossed diodes to reduce the residual transmitter noise.

Series and parallel tuning capacitors match the coil impedance to 50 Ω for maximal coupling and minimal reflection of signal. (Real and imaginary components of the coil impedance can be separately adjusted with two capacitors in this configuration.[75]) The tuned part of the circuit, including the transceiver coil, is called the *tank*. Because the

*PAR, model HR-8.
†Fluke, model 8840A.
‡Systron-Donner, model 101.
§Watkins-Johnson, model S-1.
**Vectron, model CO220.
††PAR, model 200L.

Figure 13. *Block diagram of NMR spectrometer*

PG = pulse generator
~ = oscillator
sw = RF switch
ϕ = phase shifter
BP = bandpass filter
λ / 4 = quarter-wave line
cpl = directional coupler
xmit = transmitter amplifier
rcv/ϕ = receiver amplifier and phase detector
wfr = transient waveform recorder
pre = pre-amp

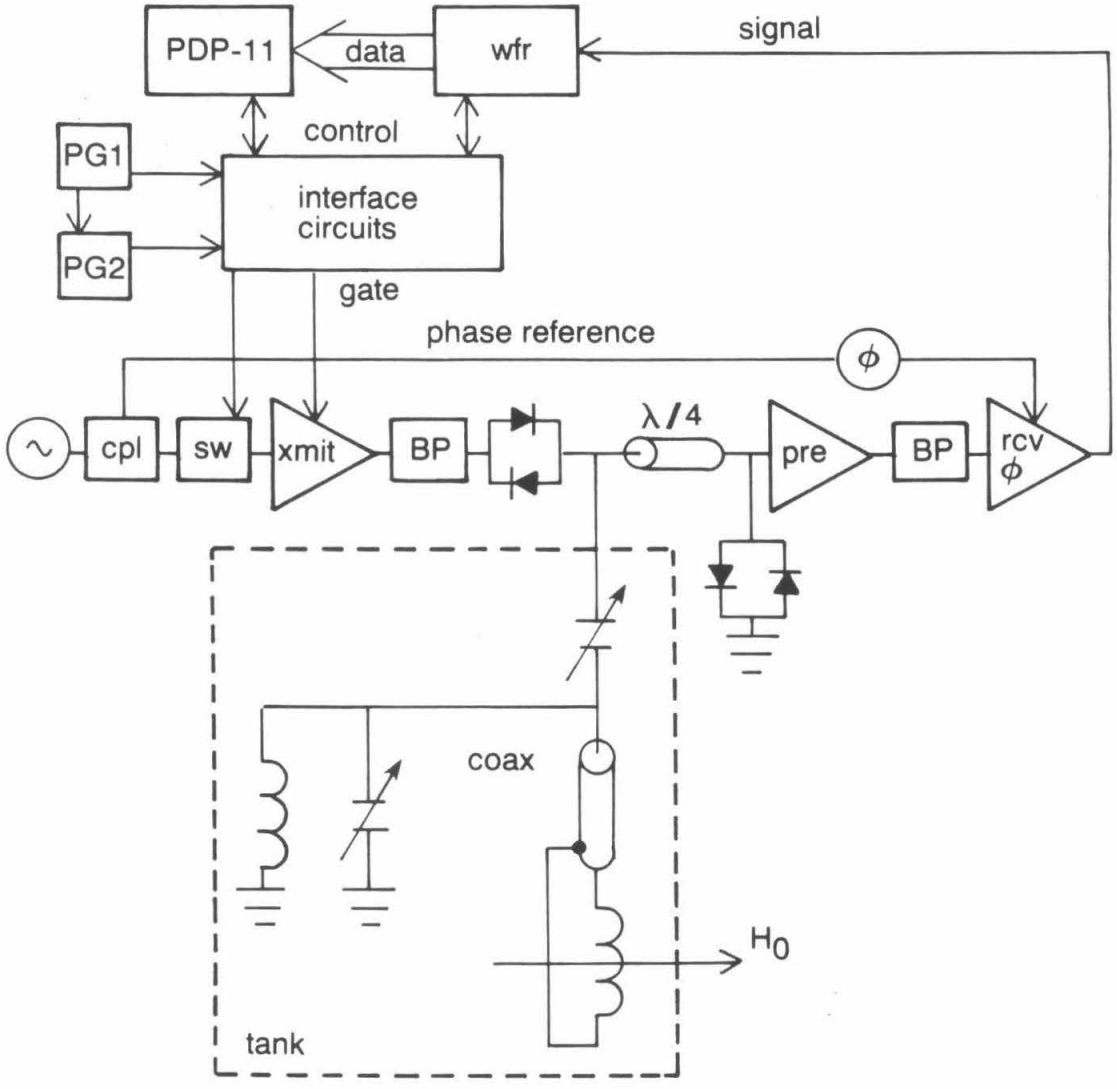

tuning components are at room temperature, while the coil is at the bottom of the dewar vessel, 1 m of semi-rigid coaxial cable is included in the tank circuit.

The magnitude of the RF field H_1 can be computed from energy considerations: the power P, expressed in terms of the energy E stored in the coil, is given by $P = \omega E / Q$, where Q is the quality factor of the coil. For a coil of volume V, the stored energy of a magnetic field H is $E = H^2 V / 8\pi$. Recalling that only half the RF magnetic field is counter-rotating, so $H_1 = \frac{1}{2} H_{peak}$, and that for a sinusoidal time variation, $\overline{H^2} = H_{peak}^2 / 2$, we find for a power of 200 W, $H_1 = (4\pi Q P / \omega V)^{\frac{1}{2}} \approx 30$ G. At this field, the length of the pulse necessary to tip the spins by 90° should be 5 μsec, which is in excellent agreement with the empirically determined value.

The FID is then picked up by the receiver and pre-amp.* The parallel crossed diodes at the pre-amp input protect it from the transmitted pulse. The quarter-wave line behaves like a switch, since the impedance Z' looking into one side of the line is related to the impedance Z at the other end by the relation $Z' = Z_0^2 / Z$, where Z_0 is the characteristic impedance of the coax. For large signals, such as the transmission pulse, the diodes turn on hard, so Z' is large and the receiver is essentially decoupled from the circuit. For small signals, such as the FID, the diodes turn off, and the tank sees only the 50 Ω input impedance of the pre-amp.[76]

The inclusion of a length of coax in the tank complicates the circuit, but once again we can use energy considerations to compute the size of the FID signal at the pre-amp input. Because the tank circuit is critically coupled to the receiver, i.e., the impedance of the tank is equal to the input impedance of the receiver, power dissipated in the receiver is equal to the power dissipated in the tank; and in the equivalent circuit shown in Figure 14, we must have $\omega_0^2 L C = 1$, since the circuit is tuned to the Larmor frequency ω_0. In the tank circuit, the loss is entirely in the coil, so if we let L be the coil inductance, and

*Matec, models 254 and 625.

Figure 14. *Equivalent circuit for tank and receiver*

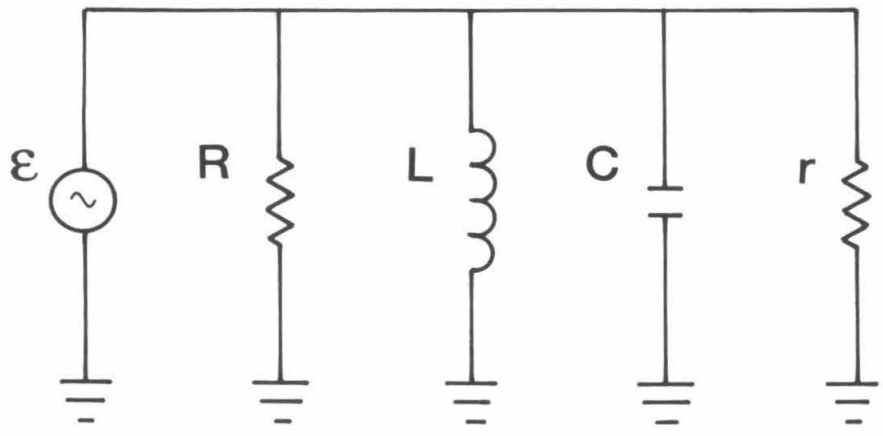

$R = Q\,\omega L$ its equivalent parallel resistance, and lump the coax, receiver and tuning components into r and C, we find the power dissipated in the tank by the nuclear induction EMF ε_{nuc} is $P = {\varepsilon_{nuc}}^2 / Q\,\omega L$. If on the other hand the coil, coax and tuning components are lumped together into R, L and C, then ε represents the voltage V_{rcv} present at the receiver input, and the power in the receiver is $P = {V_{rcv}}^2 / 50\ \Omega$. Thus, for a critically coupled circuit, tuning gives us a voltage gain $V_{rcv} / \varepsilon_{nuc} \propto \sqrt{Q}$, instead of the factor of Q usually cited in the literature, which is computed for an uncoupled circuit. The same relation holds true for the EMF of Johnson noise as well, so that the presence of the coax in the tank circuit does not alter the computation of the S/N ratio. For the present apparatus, we expect,[77] before signal averaging,

$$S/N \approx \frac{\pi}{f}\left[\tfrac{1}{2}\eta\left(\frac{\nu}{\Delta\nu}\right) Q\ \chi_0\left(\frac{\chi_0 {H_0}^2 V_s}{kT}\right)\right]^{1/2} = 5.6\ per\ monolayer,$$

where f is the noise factor of the receiver and pre-amp, η is the fraction of the coil occupied by the sample, χ_0 is the DC nuclear magnetic susceptibility, V_s is the volume of the sample, ν is the Larmor frequency, and $\Delta\nu$ is the detector bandwidth.

We return to tracing the RF signal path. A 1% bandwidth tuned filter is placed between the pre-amp and the receiver to prevent noise from swamping the detector. The FID is mixed with a sample of the oscillator frequency to produce a phase-sensitive detected signal. This signal is digitized by a transient waveform recorder* and read by the computer.

§4.5 Tuning

The spectrometer must be tuned in order to operate. First the tank circuit was tuned to 50 Ω at 30 MHz, using an RX meter. The Q of the coil depends weakly on temperature, because of the conductivity of the Grafoil, so tuning was performed after the cell

*Physical Data, model 523A.

was cold.

Next the magnetic field was tuned to bring the proton resonance to 30 MHz. When the Larmor frequency was not quite equal to the oscillator frequency, and the signal was phase-detected, the FID displayed beats. The FID lasted about 100 μsec, so when it showed no beats, the field was tuned to within .1 G (out of 7.046 kG). The DC field inhomogeneity, which is responsible for the decay of the FID, limits more precise tuning.

Because the coil can only pick up the precession of transverse magnetization, when the spins are completely inverted, there is no FID. Therefore the length of the 180° pulse was adjusted by looking for a null in the FID.

It would be possible to adjust the 90° pulse by looking for a maximum in the FID, but a null experiment is much more sensitive. The procedure for tuning the pulse width was to perform two 90° pulses in rapid succession. The transverse magnetization created by the first pulse vanished in an FID decay time. Any longitudinal magnetization remaining when the tip angle of the first pulse was not exactly 90° was tipped down into the transverse plane by the second pulse, producing an FID. This signal was null when the tip angle was exactly 90°.[78]

From the analysis of Chapter 2, it is clear that the tip angle can depend on the precise tuning of H_0. These two parameters must therefore be adjusted together.

The phase reference was adjusted by looking for a null of the FID. The reference was then brought into coherence with the FID by adding or subtracting a quarter-wave cable from one of the lines. The spin echo is particularly sensitive to the phase, so a fine adjustment is made until the spin echo was symmetrical in shape.

The DC magnetic field control* was subject to drift. A temperature-controlled box was installed around it, which held the field steady enough to run an experiment; but the field typically had to be adjusted at the beginning of each run. The other parameters

*Varian Fieldial Mark II.

required only occasional adjustment.

§4.6 Calibration of the surface area

The primary calibration standard for Grafoil surface area is the registered phase of helium, in which one helium atom occupies every third hexagon in the graphite surface honeycomb.[79] Since the lattice constant of graphite is well known, the total area can easily be computed when the amount of helium needed to fill the surface with the registered phase is determined from a vapor pressure isotherm. The calibration in the present experiment was secondary, the area being determined by comparison of a 77.4 K methane isotherm to the data of Hamilton.[38] Since the temperature of the cell varied slightly during the measurement (due to variations in the level of refrigerant, and so on) the vapor pressure data were reduced to a common temperature of 78 K according to the formula $p\,(78\text{ K})/p_0(78\text{ K}) = p\,(T)/p_0(T)$. The results, shown in Figure 15, demonstrate the difference in surface quality between the Grafoil and the Grafoil-foam product used by Hamilton. The specific areas are respectively 25.1 m^2/g and 20.7 m^2/g. Our cell had an area of 28.9 m^2, and one nominal monolayer of methane contained 8.05 stpcc.

§4.7 Procedure

At the beginning of a run, the cell, V_0, and the gas handling system were all evacuated to $1\text{-}2\times10^{-7}$ torr. Methane was then admitted to V_0 (and usually also the Barocel and a section of manifold). The valve at the top of the probe was then opened, and the dewar was filled with liquid nitrogen. When enough methane had condensed in the cell, the probe valve was shut. This was done to minimize the dead volume in contact with the surface, because molecules must exchange between the surface and the gas to maintain the equilibrium vapor pressure over the film as the temperature changes. Thus the surface coverage may vary even though the number in the cell is constant. Figure 16 shows the number on the surface as a function of temperature for the runs made in the present experiment. To compute the number of molecules in the vapor phase, the pressure was extrapolated from the data of Hamilton and the temperature profile in the fill

Figure 15. *78K vapor pressure isotherms. Circles for Grafoil, solid curve for Grafoil foam data of Hamilton.*[38]

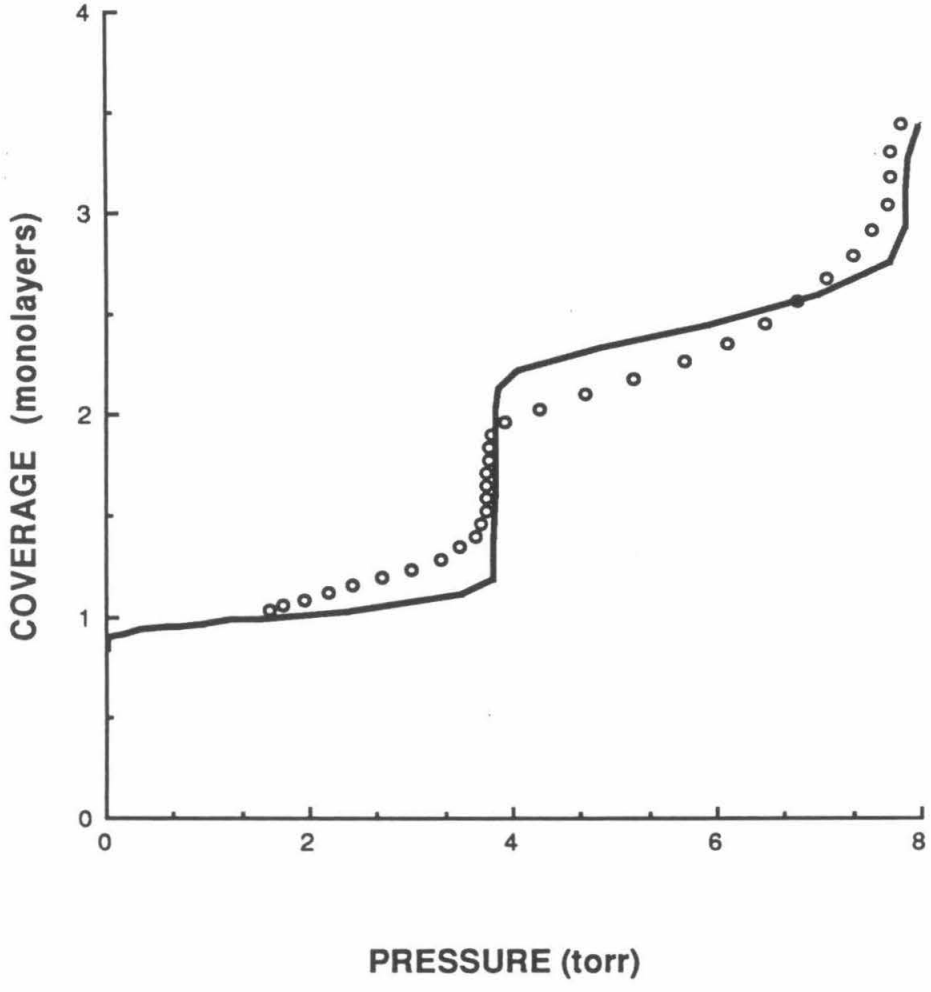

Figure 16. *Effects of desorption on surface coverage for fixed cell fillings of 51, 24, 17, 13, 10, 7.4, 4.6, 3.5, 1.8 and .87 layers (top to bottom).*

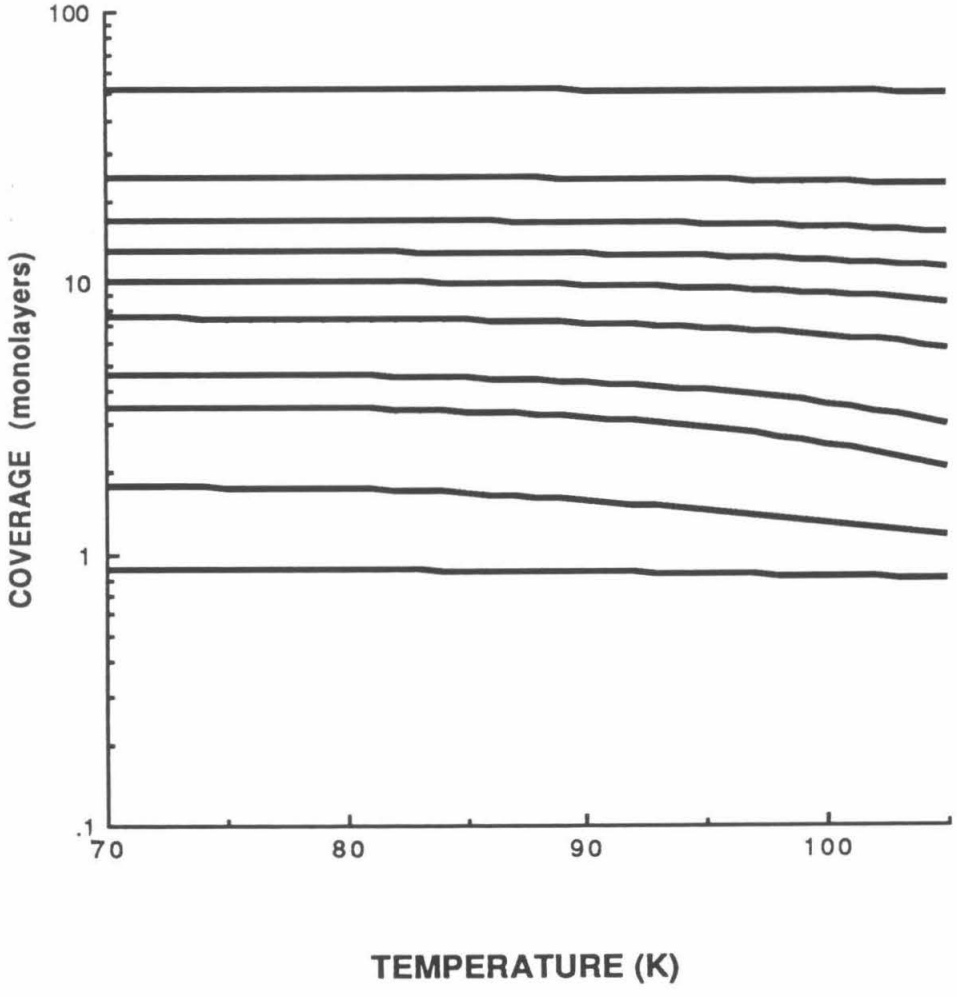

tube was assumed to be linear to allow approximately for the effect of temperature on the gas density. Effects of the non-ideality of methane gas are negligible[38] and not taken into account.

The films were annealed at 105 K. At this temperature, the vapor pressure of bulk methane is over ½ atmosphere; distribution of methane throughout the cell should take place rapidly. When this procedure was followed, the data were quite reproducible, indicating that mass equilibrium was established.

Once a particular coverage was established in the cell, the temperature of the shield was made to drift linearly with time. The drift was slow, in order to maintain thermal equilibrium: the usual rates were 10 to 15 K over an 8 hour period. Figure 17 shows T_1 data for a coverage of 17 layers, taken with both signs of temperature drift. Except near the melting transition, the data are seen to be independent of drift direction.

§4.8 Data reduction and error analysis

To measure T_1 and T_2, one must know the amplitude of the longitudinal and transverse magnetizations as a function of time after the spins are perturbed. As explained in Chapter 2, however, the signals that reach the digitizer are either FID's or spin echoes. If the shape of the waveforms were known, it would be possible to measure the amplitude by curve fitting; however, the shape is rather sensitive to the precise tuning: if H_0 drifts slightly off resonance, beats appear in the signal. By way of compromise, the integral of the signal was used as a measure of amplitude. Only ratios of amplitudes are important, and H_0 never drifted rapidly enough to cause a change in the shape of the curve during the ten minutes or so required to collect an entire saturation recovery or spin echo decay curve.

The error in the integral is estimated as follows. The baseline for the FID or spin echo is measured by averaging a flat portion of the signal, and the RMS noise voltage is taken from the scatter about this baseline. Since the error accumulates as the square root of the number of samples, one expects

Figure 17. *Thermal hysteresis shown in T_1 data for 17 layer film. Circles show data taken with upward temperature drift, squares downward.*

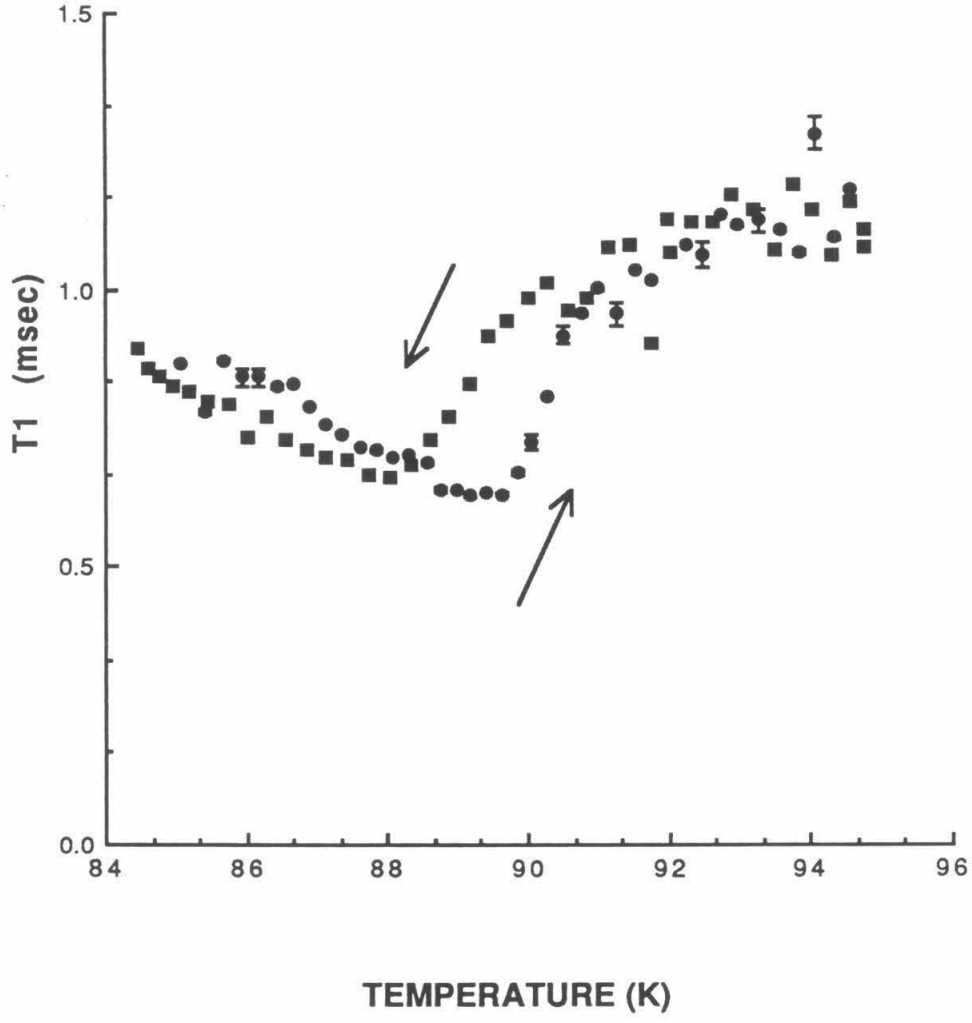

$$RMS\ error^2 = \left[N \langle V^2 \rangle + N^2 \frac{\langle V^2 \rangle}{N_b} \right] f_s^{-2} \qquad (6)$$

where N is the total number of samples on the curve, N_b is the number of points used to measure the baseline, and $1/f_s$ is the sampling interval. The first term is the integral of the noise; the second is the error in measuring the baseline, times the width of the baseline. The two terms add in quadrature.

Eq. (6) actually underestimates the noise by a factor of $\sqrt{f_s / \Delta f}$, where f_s is the sampling rate and Δf is the bandwidth of the phase detector's low-pass output filter. This is because the sampled noise voltages are not independent; the low pass filter causes the individual points to be correlated. The proof is relegated to appendix IV.

Once we have found the error in the integral for each point, the statistical errors in T_1 and T_2 are found in the usual way from a least squares analysis.[80] The fitting functions were

$$M_\perp = M_0 e^{-t/T_2} \quad \text{and} \quad M_\parallel = M_0 (1 - e^{-t/T_1}),$$

with free parameters M_0, T_1, and T_2. In all cases, exponential curves provided excellent fits, as shown in Figure 18.

Figure 18. *Typical saturation recovery and spin echo decay curves. The data shown are for T = 87.35 K and a coverage of 8.0 layers.*

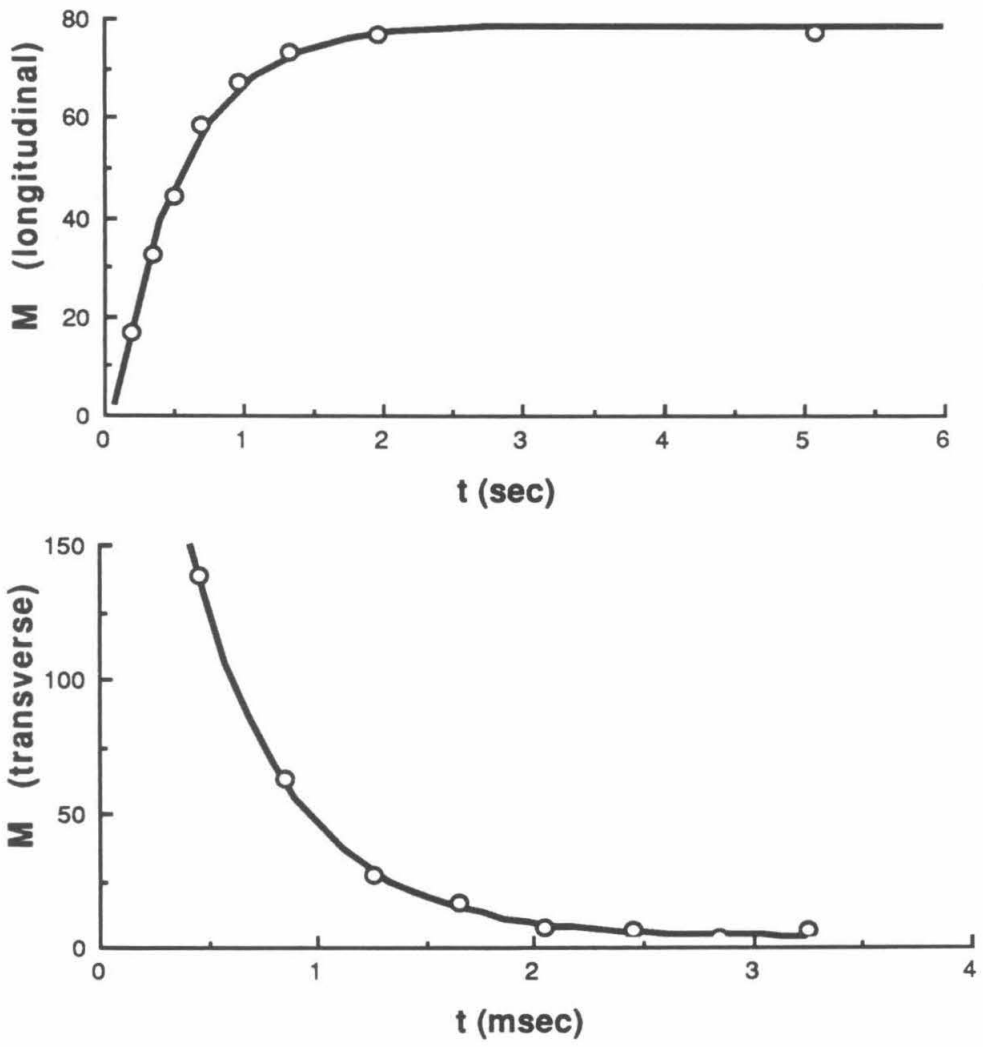

Chapter 5

Experimental Results

In this chapter we present our experimental results and the models we propose to explain them. First we discuss measurements made on pure bulk methane, which serve as a check of our experimental technique; next we consider results for thick films, where the film is substantially bulk-like, to determine the effects of the substrate on the methane NMR signal; and finally we analyze our thin film results.

§5.1 Bulk results

The NMR properties of bulk methane are well understood.[81,82] The liquid is in the motionally narrowed regime where the correlation time for diffusion, τ_c, is short compared to the Larmor period, so $\tau_c\ \omega_0 \ll 1$. In this regime, T_1 is proportional to the diffusion constant D, and presumably $T_2 = T_1$, although measurements of T_2 in bulk liquid methane have not hitherto been reported. At the triple point, T_t, the diffusion constant D of bulk methane changes from 6.7×10^{-9} cm^2/sec[82] to 2.5×10^{-5} cm^2/sec.[83] Bulk methane shows discontinuities in both T_1 and T_2, reflecting the abrupt change in molecular dynamics, as seen in Figure 19. Because of the low mass of the methane molecule, diffusion is important in the solid too, and down to 65 K, just as for the liquid, the translational degrees of freedom are the main source of relaxation, via the *inter*-molecular dipolar coupling. However, diffusion is sufficiently slow in the solid that $\tau_c\ \omega_0 \gg 1$, and in this regime $T_1 \propto 1/D$ while $T_2 \propto D$. The line shape for the solid above 65 K is Lorentzian, that is, the transverse magnetization decays exponentially, as one expects in a solid with diffusion the dominant relaxation mechanism. Diffusion is a thermally activated process in both liquid and solid, so $D \propto \exp(-E_d / k_B T)$, where the energy barrier E_d is about 1900 K for the solid and 390 K for the liquid. Because of the activated form, it is convenient to plot T_1 and T_2 on a logarithmic scale for bulk and thick films.

Figure 19. *NMR in bulk methane. T_1 for solid and liquid; T_2 for solid (open circles) and T_2^* for liquid (closed circles). Curves show data of references 81 and 82. Note logarithmic scale.*

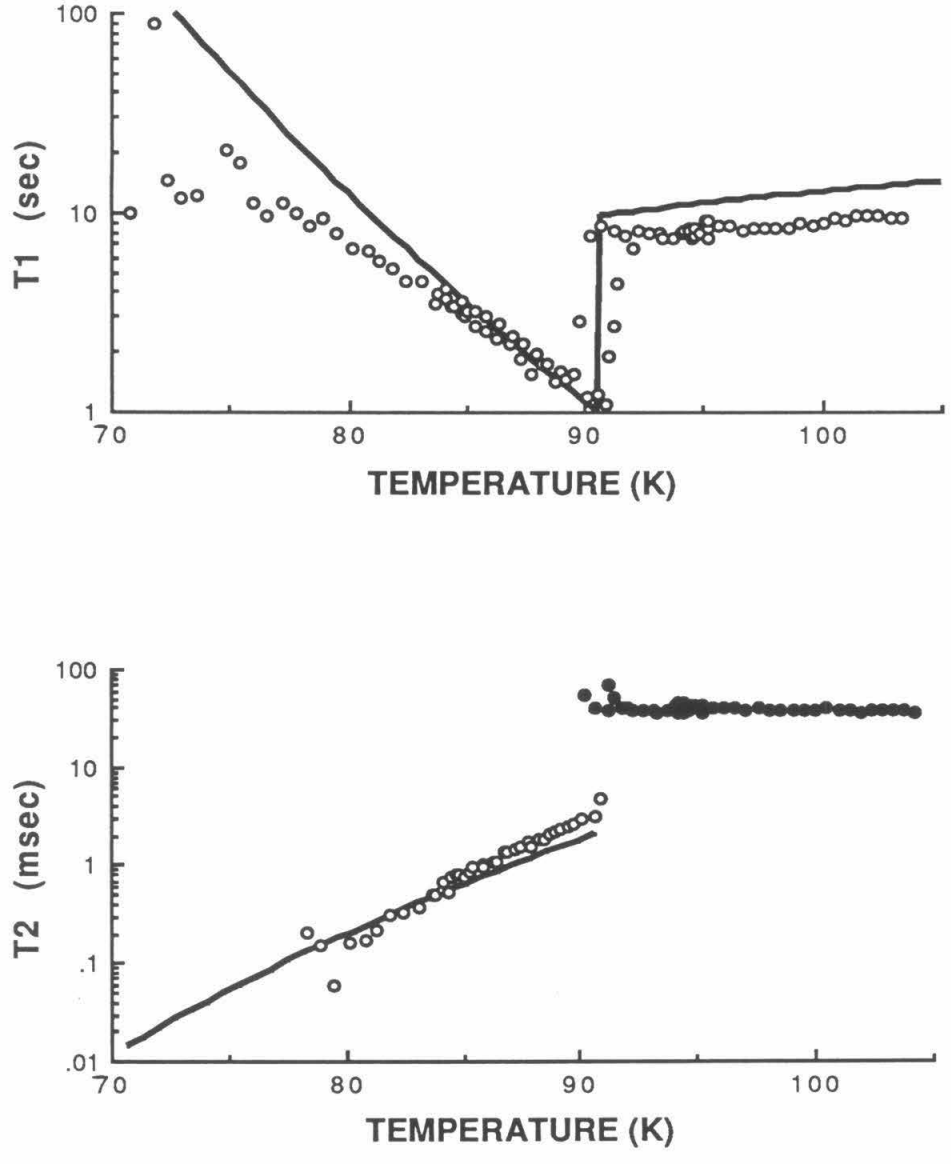

Our T_1 results serve as a check for oxygen contamination of our methane. The data shown in Figure 19 agree well with the results of previous experiments for $T_1 \lesssim 10$ sec, proving the purity of our sample. We did not successfully measure T_1's much longer than 10 sec because our repetition rate was 24 sec in the experiments on bulk samples. In our analysis of the film results below, our data are much more accurately predicted if we assume the bulk T_1's are like those of Ref. (82) and not like our shortened ones, so we conclude that the shortening in our bulk data is instrumental, and not due to contamination.

In the liquid, the decay of the transverse magnetization is observed not to be exponential. This arises from the effects of field inhomogeneity. In the presence of a gradient of the DC magnetic field, the transverse nuclear magnetization decays according to the law

$$M_{\perp}(t) \propto \exp(-t/T_2 - \gamma^2 G^2 D\, t^3/12), \tag{7}$$

where G is the field gradient and D is the diffusion constant.[84] This is because as the spins drift into regions of different H_0, they precess at different rates and lose phase coherence. For the liquid, T_2 and D are both large, so the cubic term dominates the exponential in agreement with our data. We therefore use the fitting function $M_{\perp}(t) \sim \exp(-t^3/T_2^{*3})$ for the liquid; and while for convenience we plot T_2^* on the same graph as T_2 of the solid, it should not be overlooked that the two quantities are of different physical origin.

To check this interpretation of the behavior of the transverse magnetization in the liquid, we can estimate the order of magnitude of T_2^* as follows. Our field inhomogeneity, as measured from the length of the free induction decay (FID), is $\Delta H = .4$ G. Therefore the field gradients should be on the order of $G = \Delta H / a$, where a, the sample size, is 11 mm. Using the value of the diffusion constant cited above, we predict $T_2^* \approx 170$ msec, in reasonable agreement with our results. This lends confidence to our

interpretation of the bulk liquid T_2's. For the solid we would compute $T_2^* = 3$ sec, so the cubic term is negligible compared to the intrinsic decay term, which is why our solid T_2's are in good agreement with values published elsewhere.

§5.2 Thick films: T_1

Figure 20 shows our T_1 data for a coverage of 24 layers. While the discontinuity at the melting transition is still clearly visible, it is enormously reduced compared to the bulk. Furthermore, T_1 is highly depressed from its bulk value. While the shortening of T_1 in monolayer films on graphite is a standard observation, it is surprising to see a large effect in such a thick film, where the molecular dynamics might be expected to be bulk-like.

Two explanations for the T_1 shortening in films are commonly offered: relaxation by substrate conduction electrons,[85] and relaxation by paramagnetic impurities in the substrate.[86] The conduction electron hypothesis must be rejected, however, because with a correlation time for electronic diffusion of $\tau_c = 10^{-13}$ sec and a carrier concentration of only 2×10^{18}/g,[87] the resulting relaxation is motionally narrowed to the point of complete ineffectuality. On the other hand, it is not necessary to invoke the existence of undetected paramagnetic impurities, for it has been shown[88] that the graphite crystal structure is very susceptible to damage, perhaps especially at the surface, resulting in localized paramagnetic electronic defect states. In order to study the origin of the shortening of T_1 and the suppression of the discontinuity, a series of runs was made at large coverage. It was found that the effect is distinctly observable even in films as thick as 51 layers (about 65 layers saturates the Grafoil pores) and depends smoothly on coverage. We shall now demonstrate that the effects of fixed paramagnetic spin centers in the substrate are in agreement with our data; our model will not rely on the exact nature or distribution (bulk or surface) of the paramagnetic sites.

First let us compute the relaxation rate $1/T_1'$ due to a single paramagnetic center. The full dipolar coupling Hamiltonian is given by

Figure 20. *T_1 for 24 layers*

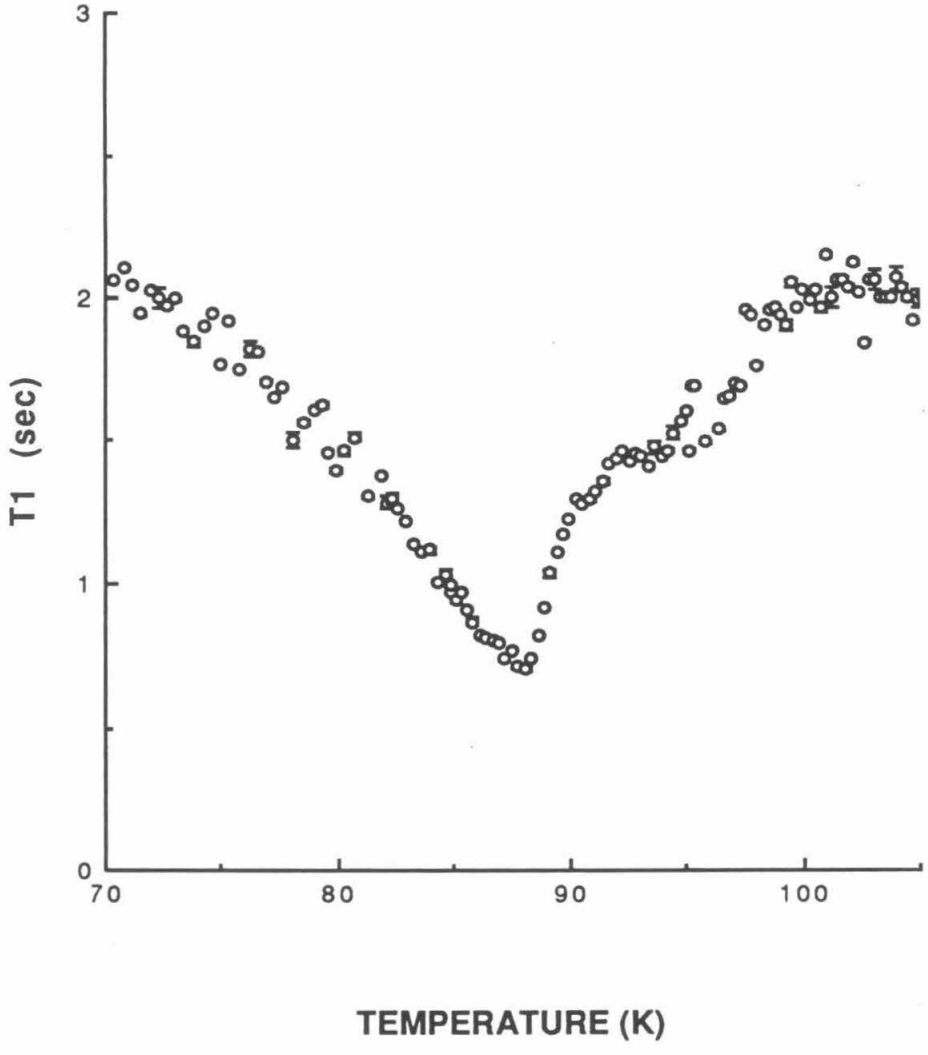

$$\mathbf{H} = \gamma_S \, \gamma_I \, \hbar^2 \vec{\mathbf{I}} \cdot \left[\frac{\vec{\mathbf{S}}}{r^3} - \frac{3\vec{r}\,(\vec{\mathbf{S}} \cdot \vec{r})}{r^5} \right],$$

where γ_I, $\vec{\mathbf{I}}$ and γ_S, $\vec{\mathbf{S}}$ are the gyromagnetic ratio and spin operator for the nucleus and the paramagnetic site, respectively, and $\vec{r}$ is the separation between them. Of all the terms in this Hamiltonian, only two will contribute significantly to the relaxation rate, viz.,

$$\mathbf{H} = -\frac{3}{2} \sin\theta \cos\theta \, \gamma_I \, \gamma_S \, \frac{\hbar^2}{r^3} \, e^{-i\phi} \, \mathbf{S}_z \, \mathbf{I}_+ + \textit{Hermitian conjugate},$$

where $\mathbf{I}_+ = \mathbf{I}_x + i\,\mathbf{I}_y$, and θ, ϕ are the polar co-ordinates of $\vec{r}$ with respect to the $\hat{z}$ axis defined by the direction of $\vec{H}_0$. The other terms are negligible for the following reasons.

1. The operators $\mathbf{S}_\pm = \mathbf{S}_x \pm i\,\mathbf{S}_y$ cause flips of the electronic spin, and therefore require fluctuating fields of frequency on the order $\omega_S = \gamma_S \, H_0$, which we shall see are much higher than the frequencies available.
2. Any terms with the operator $\mathbf{I}_z$ commute with the Zeeman Hamiltonian and therefore do not produce relaxation between the unperturbed states.

With this simplified Hamiltonian, the usual second order time-dependent perturbation theory yields a relaxation rate

$$1/T_1' = \frac{9}{2} \, \frac{{\gamma_S}^2 {\gamma_I}^2 \hbar^2 \sin^2\theta \cos^2\theta}{r^6} \left\langle \int_{-\infty}^{\infty} S_z(0) \, S_z(t) \, e^{-i\omega_I t} \, dt \right\rangle,$$

where the longitudinal spin S_z can now be treated as a fluctuating classical random variable; the factor in the expectation value brackets is its power spectrum. We may replace the angular factor by its average value of 2/15 and approximate the power spectrum of S_z by $(2/3)\,S(S+1)\,\tau/(1+{\omega_I}^2\tau^2)$, with τ the longitudinal relaxation time for the paramagnetic center. Then we have

$$1/T_1' = \left[\frac{2}{5} \, \frac{{\gamma_S}^2 {\gamma_I}^2 \hbar^2}{r^6} \, S(S+1) \, \frac{\tau}{1+{\omega_I}^2\tau^2} \right].$$

So far we have followed the standard theory of relaxation by fixed paramagnetic impurities in a solid.[89]

Let us now compute the total paramagnetic relaxation $1/T_1^{par}$ due to a distribution of spin centers on the surface with density σ and spin $S = ½$. If the fluctuations of the individual spins are uncorrelated, then each will contribute in parallel, and the total relaxation $1/T_1^{par}$ will be the integral over the surface of the individual relaxation rates,

$$1/T_1^{par} = \int \frac{\sigma d^2 A}{T_1'} = \frac{3\pi}{20} \frac{\sigma \gamma_S{}^2 \gamma_I{}^2 \hbar^2}{z^4} \frac{\tau}{1+\omega_I{}^2 \tau^2},$$

for a nucleus at a height z above the surface.

Now we write a macroscopic equation for relaxation of the longitudinal nuclear magnetization, $M_\parallel(t, z)$, to its equilibrium value, $M_\parallel^0$,

$$\frac{\partial}{\partial t} M_\parallel(t, z) = \frac{M_\parallel{}^0 - M_\parallel}{T_1{}^b(T, d)} + \frac{M_\parallel{}^0 - M_\parallel}{T_1^{par}(z)} + D(T)\nabla^2 M_\parallel$$

The first term represents the bulk relaxation rate which can depend on temperature, and in principle on film thickness d, if the film's physics changes with coverage. The second term represents the local relaxation by the substrate spin centers. The third term accounts for transport of magnetization by molecular diffusion. In films this molecular diffusion term can have the effect of averaging $T_1{}^{par}(z)$ over the thickness d of the film. In particular, in our data, the diffusion constant is always sufficiently large that each methane molecule traverses the entire film profile in a time T_1; even for the lowest temperature and the shortest experimental T_1's, the diffusion length $\sqrt{DT_1}$ is greater than the thickness d of any of our films. Hence, to an excellent approximation,

$$\frac{\partial M_\parallel}{\partial t} = \left\langle \frac{1}{T_1{}^b} + \frac{1}{T_1^{par}(z)} \right\rangle (M_\parallel{}^0 - M_\parallel);$$

the experimental result is an exponential decay with a time constant averaged over z. (An example of a similar averaging effect is given by Wu et al.;[90] in this experiment, molecules of xenon gas experience a quadrupolar relaxation averaged laterally over the cell walls.) With a cutoff of d_0 (of the order of a molecular diameter), we have

$$\frac{1}{T_1} = \frac{1}{T_1{}^b} + \frac{\pi}{20}\gamma_S{}^2\gamma_I{}^2\hbar^2\frac{\sigma}{d_0{}^3 d}\frac{\tau}{1+\omega_I{}^2\tau^2}. \qquad (8)$$

If the spin centers are distributed throughout the bulk with density ρ instead of being confined to the surface, the result is changed only by the substitution of $\rho/2d_0{}^2$ for the factor $\sigma/d_0{}^3$.

In principle, one could learn whether the paramagnetic centers are bulk or surface distributed by studying the dependence of T_1 on the cutoff parameter d_0. We performed one experiment in which data from a 3.5 layer film was compared to data from the same amount of methane separated from the surface by 5 layers of xenon. The xenon increases T_1 by a factor of 2, much less than expected. The xenon may have mixed with the methane, or the model may not well reflect the dependence of T_1 on d_0; but the result nevertheless confirms that T_1 depends of the distance of the film from the substrate.

Figure 21 shows a one-parameter fit to our data. The agreement is remarkable over two orders of magnitude in predicting the dependence of T_1 on coverage, and the suppression of the discontinuity. The coefficient of $1/d$ is found to be 55 Å/sec. To make a numerical comparison of this coefficient to the prediction of our model, let us suppose that the spin centers have the gyromagnetic ratio of the free electron, and a relaxation time of 10^{-8} sec, as observed in Ref. (87). (We are assuming that the paramagnetic spins have powerful relaxation mechanisms of their own, so that the longitudinal and transverse relaxation times are the same and we can infer the longitudinal relaxation time from the line width.[87]) To produce our observed relaxation rate, we require a surface concentration σ of one spin center per 10^4 Å^2, which corresponds to a

Figure 21. *Dependence of T_1 on coverage shown on logarithmic scale. Data are shown for bulk, 51, 24, 17 and 10 layers (top to bottom). Solid curves, 1-parameter fit to data.*

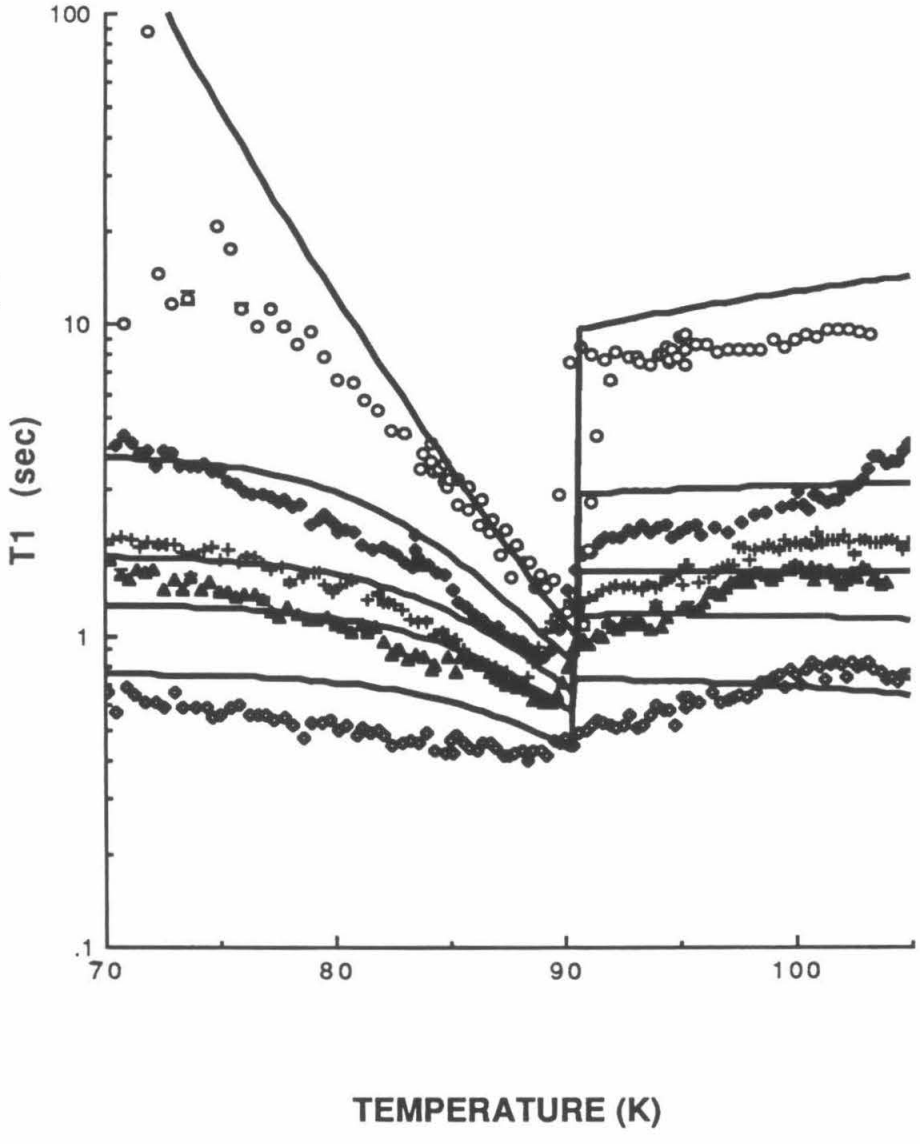

total density of 2×10^{17}/g for our sample. (The analogous result for a bulk distribution is 2×10^{19}/g.) In Ref. (88) it was found that mechanical grinding of Madagascar graphite produced a density of 10^{19} spins/g; compared to this, only a small number of defect sites are required to produce the observed effect if they are distributed on the surface; a bulk distribution requires a concentration of spins comparable to that produced by grinding.

The success of this simple model indicates that uniform methane films, both solid and liquid, grow on the Grafoil substrate up to thicknesses of 51 layers. This result is surprising because one expects film growth to be interrupted, either by capillary condensation in the porous Grafoil medium, or because thick solid films are not expected to wet the solid graphite substrate, as we mentioned in Section 1.4. In either case, one expects an admixture of thin film and bulk methane in a nominal 51 layer sample.

To check this possibility, we have attempted to fit our data with a sum of two exponential decays, a long one for bulk matter too far from the substrate to be relaxed by the substrate spins, and a shorter one for the film. Interdiffusion between the two phases will not average the relaxation rates as long as $\sqrt{D\,T_1^{film}} \ll R\,a$, where R is the ratio of the amounts of methane in bulk and film, and a is the Grafoil platelet size. This criterion is well met for the solid; yet the data make an excellent fit to a single exponential. Therefore we conclude that the methane in a 51 layer film is distributed near the surface, and that there is no population of methane in a distinct macroscopic phase. (The phenomenon of triple point dewetting described in Section 3.3 should create a nonuniform film just below the triple point temperature, but it occurs in a temperature interval, $\Delta T \lesssim 0.2$ K, too small to be resolved in the present experiment.) We shall remark further on capillary condensation in Section 6.1.

§5.3 Thick films: T_2

Turning now to the relaxation of the transverse magnetization, we show in Figure 22 characteristic decay times T_2 for two film thicknesses. There are four general observations to be made about the data. First, the decay is now a simple exponential for both

Figure 22. *T_2 for thick films; coverages are 51 and 13 layers (top to bottom).*

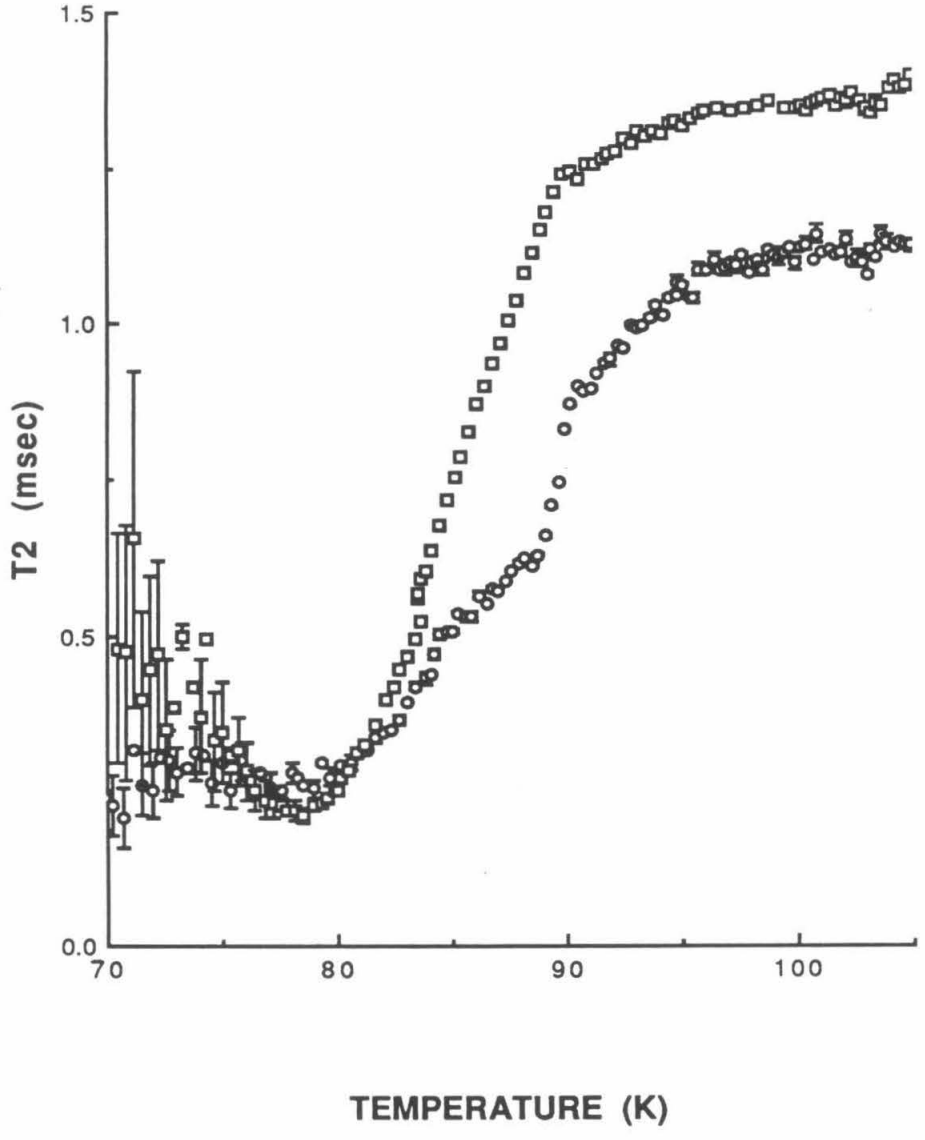

liquid and solid; second, the time constants for the liquid are much shorter in the film than in the bulk; third, the time constant depends only weakly on film thickness; and last, that the 13 layer film shows a small discontinuity in T_2, but the 51 layer film shows only a change in slope. We shall discuss these four points in order.

The explanation of the first two points is based on the fact that diffusion on the Grafoil platelets is bounded in space. When the diffusion length $\sqrt{D\,t}$ becomes comparable to the platelet size, which we shall call a, the exponential cube behavior given by Eq. (7) saturates, and for later times, the magnetization obeys approximately[91]

$$M_{\perp}(t) \propto \exp\left[-\frac{a^4\gamma^2G^2}{120D}\left[t-\frac{17\,a^2}{56D}\right]\right]. \tag{9}$$

Thus one again observes a pure exponential decay, but with a shortened time constant $T_2 = 120D/(a^4\gamma^2G^2)$. This result will hereafter be referred to as the bounded-diffusion model.

This explanation has been offered by Husa et al.[92] to account for data on Grafoil saturated with bulk ethanol. With a platelet size of 1.3 μm, a field gradient of 1000 G/cm is required to reproduce the data. This gradient arises from the inhomogeneous and anisotropic magnetic susceptibility of the graphite flakes. It is consistent with their observed field inhomogeneity $\Delta H = .15$ G, as deduced from the length of the free induction decay. If the inhomogeneity is due to the magnetic susceptibility of Grafoil, then the magnitude of the gradient should be proportional to H_0, and the anomalous relaxation rate should be proportional to ${H_0}^2$, as observed by Husa. Our T_2 imply a field spread of $\Delta H = .5$ G over a platelet, which is not a bad disagreement, especially since T_2 depends on such ill-defined parameters as a and G to high powers.

For the solid, on the other hand, $a^2/D \geq 2.5$ sec, which is much greater than T_2. Thus the bounded-diffusion effect plays no role in the solid, for the magnetization decays before the asymptotic form of Eq. (9) becomes valid. The bounded-diffusion effect

therefore does not have much effect on the solid, which is why T_2 is only weakly dependent on coverage. The dependence that is observed may be a reflection of the fact that motions of molecules near the surface of the films are restricted, reducing the motional narrowing effect.

The other relaxation mechanism we have considered, that arising from spin centers in the substrate, should also affect T_2. Because of the short correlation time of the spins, however, we expect this mechanism to be much slower than the other mechanisms we discuss here.

Finally, we observe that we expect a discontinuity in T_2 at melting, such as is seen in the 13 layer data, unless the dominant relaxation mechanism is one which is not affected by the transition. We have seen, however, that this is not the case. Attempts to find a discontinuity in a 51 layer film by lowering the rate and changing the direction of the temperature drift were unsuccessful. While the discontinuity is expected to be small because of the bounded-diffusion effect, we cannot explain why it is invisible in the 51 layer data. Nevertheless, the melting transition is still apparent in T_2 as a change in slope.

§5.4 Thin films

In the last two sections we have studied films of coverage greater than 10 layers in order to learn about the basic effects of the Grafoil substrate on the NMR signal of the adsorbed film. We shall now apply this knowledge, returning to the study of thin films less than 10 layers thick, which was the original subject of this experiment. Unfortunately, the effect of paramagnetic spins in the substrate, discussed in Section 5.2, completely dominates T_1 in the thin film regime, leaving the curves flat and featureless. Happily, however, the T_2 curves still display a feature at the melting transition, which we shall use to pursue the melting transition to lower coverages. We shall present our results in order of decreasing coverage.

The data shown in Figure 23 indicate that as the coverage decreases there is a gradual reduction of the T_2 discontinuity to a change in slope. This effect probably should not be interpreted as an indication that melting becomes continuous as the coverage approaches a monolayer. According to our study in Section 5.3, the relaxation mechanisms in the liquid and solid are quite different, and equality in T_2 does not imply equality of microscopic behavior. More likely, the discontinuity in T_2, which is small to begin with, is obscured by the effects of substrate inhomogeneity,[93] which are known to broaden phase transitions in adsorbed films by a degree or more in temperature. We have seen in Chapter 3 that the melting curve is very sensitive to the substrate potential and surface tensions, so if there exist imperfections in the surface, there may be points on the substrate where the melting transition takes place at lower or higher temperatures than the rest of the surface. This effect will become stronger as the coverage is reduced.

Surface melting is another possible broadening mechanism that could smooth out the T_2 discontinuity, which we must consider. We have seen in Section 3.4 that in the surface melting model, the transition may be spread out over tens of degrees because of the high energy cost of making the solid-liquid interface approach too closely to the outer surfaces of the film. Although the heat capacity measurements discussed in Section 3.3 show the wrong asymptotic dependence on coverage and temperature to be consistent with surface melting, the hypothesis nevertheless continues to be tempting because the broadening of the transition for thin films might possibly explain why the latent heat of melting vanishes at four layers, as mentioned in Section 1.6. Let us then consider what the NMR signal of a surface melted film should look like.

At high enough temperatures, i.e., above the melting transition, motional narrowing makes *inter*-molecular dipolar coupling an inefficient mechanism for relaxation for both liquid and solid components of the film, compared to the bounded-diffusion mechanism in the liquid. Insofar as some of the spins do not participate in the rapid diffusion of the liquid, then the bounded-diffusion mechanism will be proportionately less effective in

Figure 23. *Dependence of T_2 on coverage for intermediate film thicknesses. Top to bottom: 13, 10 and 7.4 layers.*

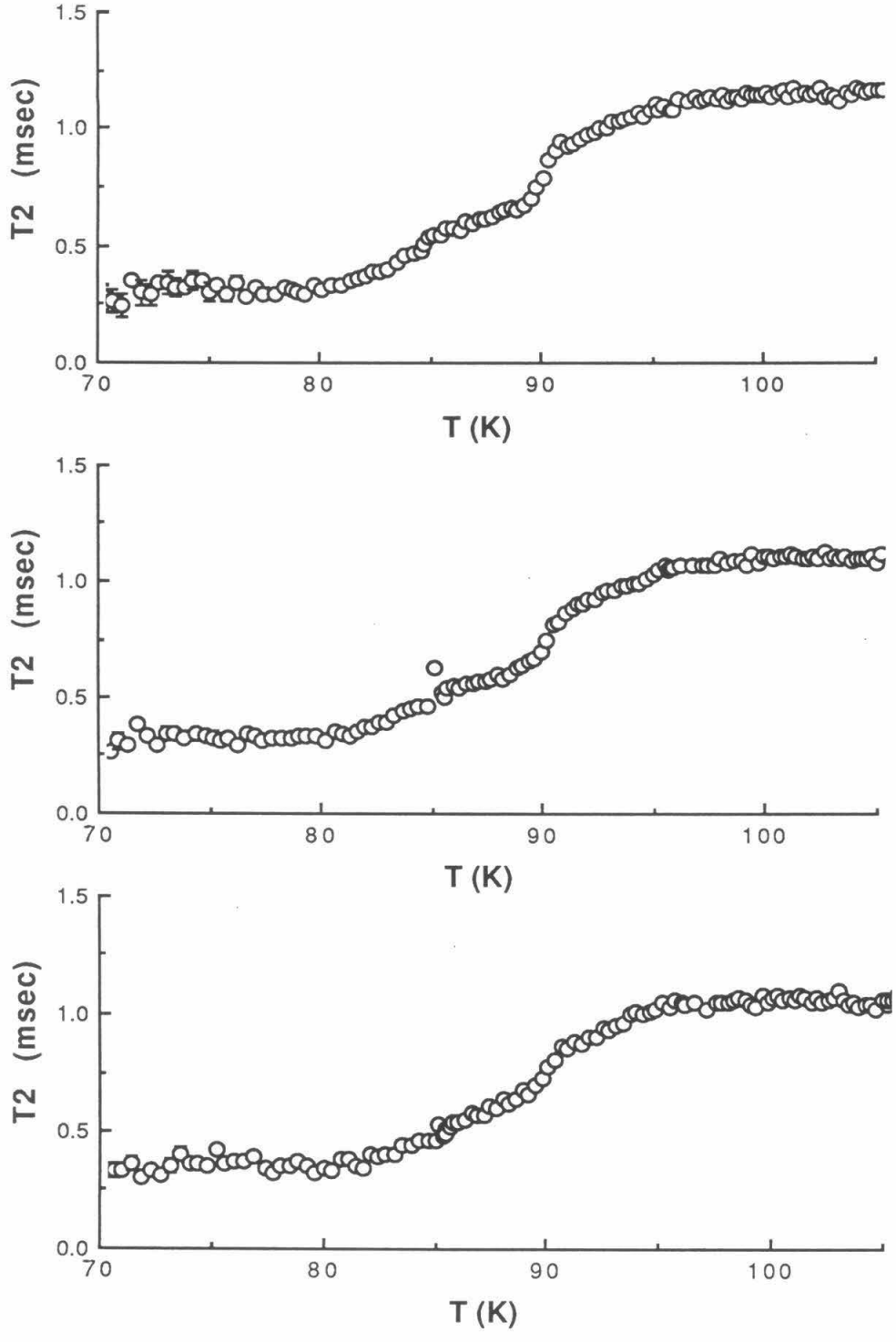

relaxing the total transverse magnetization.

It is plain that this result does not depend very sensitively on the exact model of surface melting. We can provide a somewhat quantitative estimate of the effect. As in Section 5.2, we write a macroscopic equation for the decay of the transverse magnetization,

$$\frac{\partial}{\partial t} M_{\perp}(z,t) = -\frac{M_{\perp}}{T_2(z)} + D\,\nabla^2 M_{\perp}.$$

This time the variation of the local relaxation rate $T_2(z)$ with height z is due to the change in molecular dynamics across the solid-liquid interface. The second term again accounts for the transport of nuclear magnetization by molecular diffusion. We know the T_2's for the individual phases from our thick film data where, if surface melting effects exist, they are a negligible correction. Once again we find that the diffusion length $\sqrt{D\,T_2} \gg 60$ Å for all but the lowest temperatures of the present experiment. For a film much thicker than this, we would expect the transverse magnetization in the liquid and solid components of a surface melted film to be decoupled, so the time dependence of $M_{\perp}$ should be the sum of two exponential decays with time constants T_2^l and T_2^s, respectively. For thick films, however, the transition has narrow width in temperature, and away from the transition, the component of the film in the wrong phase is only a small fraction of the whole, so this effect should not be observable. For thin films such as we consider here, however, the diffusion term causes each spin to experience an average relaxation rate which is a weighted harmonic mean of the individual rates,

$$\frac{1}{T_2} = \frac{x_l}{T_2^l} + \frac{x_s}{T_2^s}, \tag{10}$$

where x_l, x_s are the fraction of the film in the two phases. Using the surface melting model of Section 3.4 to predict the quantities x_l, x_s as a function of coverage and temperature, we find that T_2 should be increased at all temperatures. This is because T_2^s is a rapidly rising function of temperature and crosses T_2^l near the melting transition. Then

below the transition, $T_2^l > T_2^s$ and the presence of liquid raises T_2; while for higher temperatures, $T_2^s > T_2^l$ and the solid raises T_2. The elevation of T_2, which should be as much as 50%, is not observed in the phase above the melting transition, and this corroborates our belief, based on the heat capacity data, that surface melting is not the mechanism of melting in methane on graphite.

Perhaps the most striking feature of the data shown in Figure 23 is the weakness of the dependence of T_2 on coverage. Figure 24 shows that T_2 for the thinnest films, less than 4 layers, is slightly elevated, but otherwise there appears to be remarkably little change in the signal with film thickness. No change is observed at the second layer transition mentioned in Section 1.6.

To test the possibility that the data are the result of an instrumental artifact, one run was made at submonolayer coverage; since the monolayer triple point is 57 K,[46] the curve should not have any feature near the bulk triple point: and the curve shown in Figure 25 is indeed the only one which differs qualitatively from the others, confirming that our other data are valid.

We would like to use our submonolayer data to make contact with previous submonolayer experiments. At the coverage and temperature range of our run, the film is in the two-dimensional liquid phase. Of previous NMR studies of methane on graphite in the submonolayer range, one[94] used a graphitized carbon black called Spheron 6 for a substrate, precisely because the local field inhomogeneities are less for this material than for Grafoil. Accordingly, the liquid T_2's measured in this study are much higher than our data. The other previous study[95] used Grafoil as the substrate, but operated at the lower Larmor frequency of 4.586 MHz. Since the decay time predicted by the bounded diffusion model varies inversely with H_0^2, our liquid T_2's would be expected to be 40 times shorter; indeed we measure T_2's shorter by a factor of 10. Our T_1's are comparable in magnitude to the results of the same study.

Figure 24. *Dependence of T_2 on coverage for thin films. Circles, 4.6 layers; diamonds, 3.5 layers; squares, 1.8 layers.*

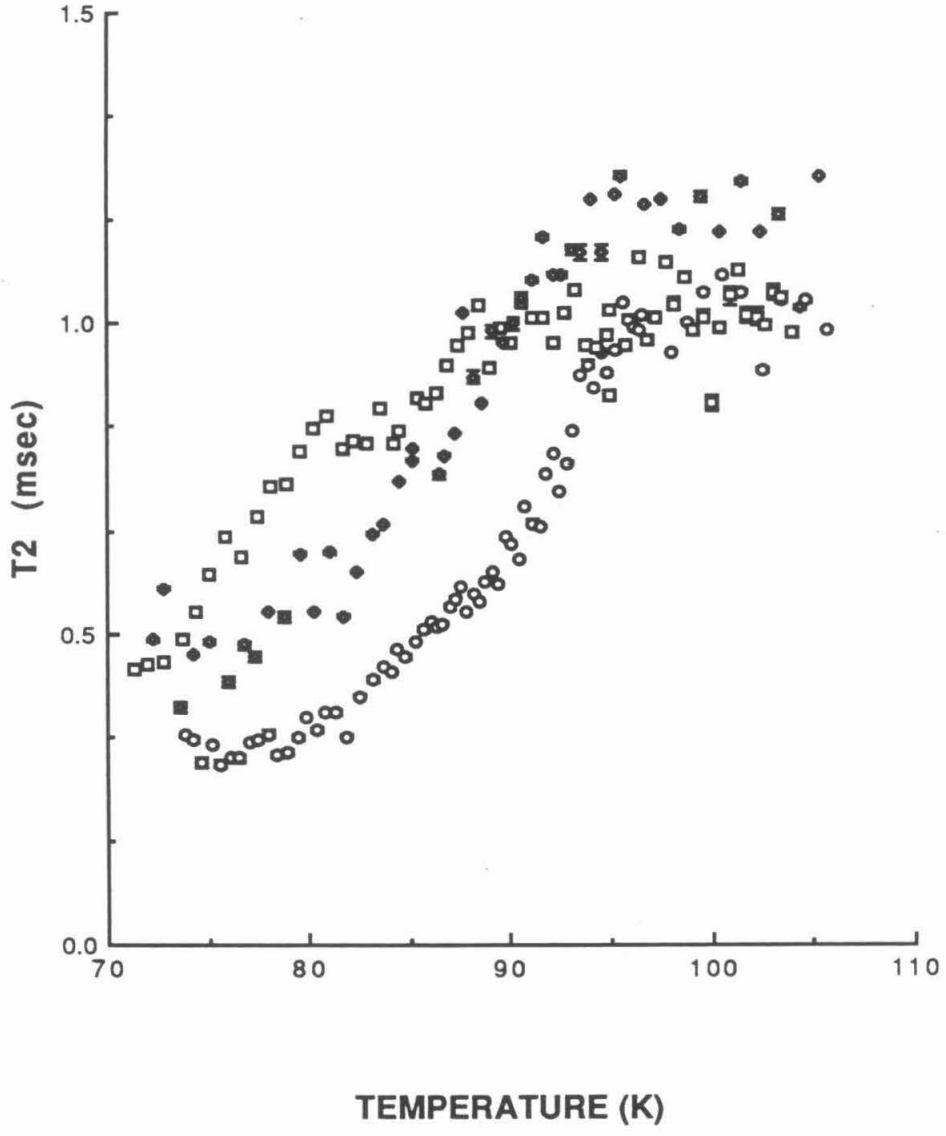

Figure 25. *T_2 for submonolayer film: .87 layers*

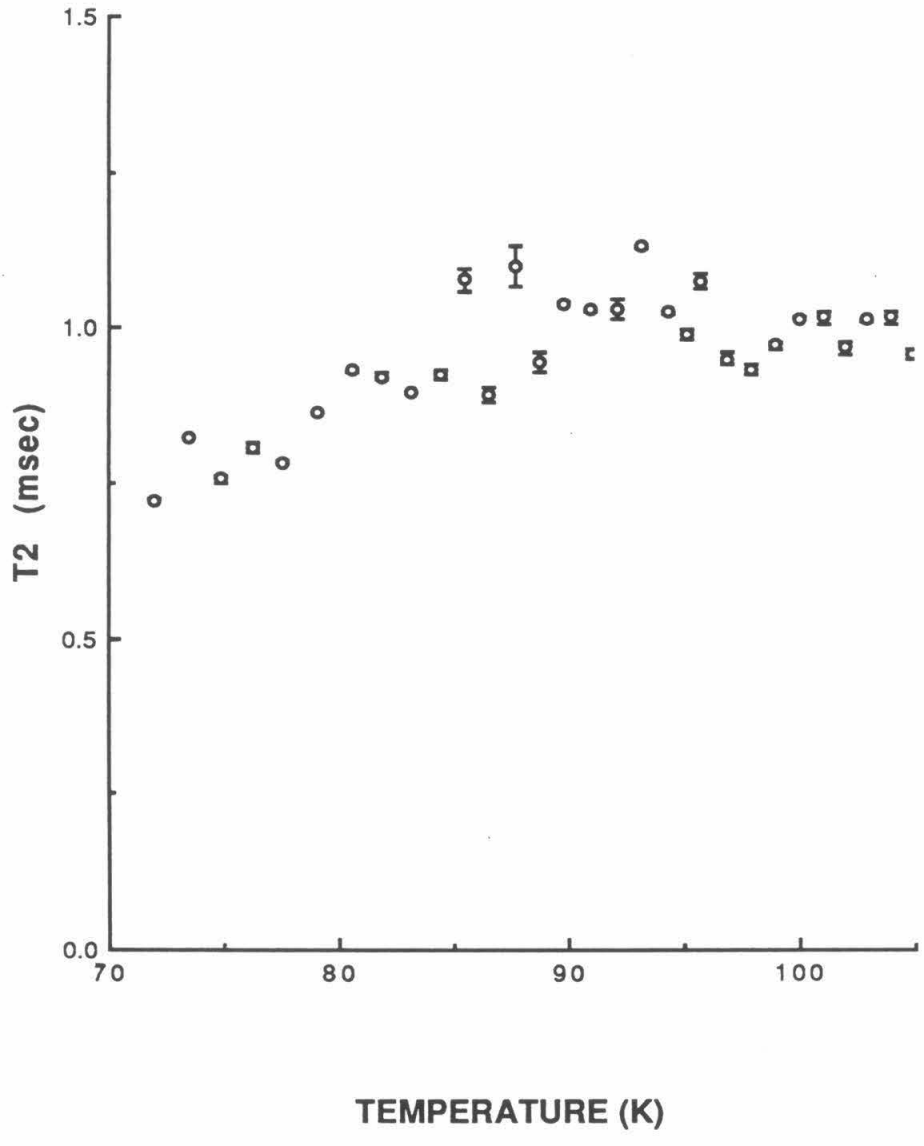

Let us pursue the question of the elevation in thin films of T_2 in the phase below the melting transition. For a thin film one would expect that the geometrical restriction on molecular motion[91] would reduce the effect of motional narrowing and therefore shorten T_2. Instead, in our films of slightly more than 1 layer, we see an increase, implying that the multilayer films show enhanced mobility with respect to the bulk. This is consistent with the conclusion of the heat capacity survey of Hamilton:[26] viz., that above 78 K, the methane surface is rough. Since in the rough phase, steps on the surface are unbound, one would expect free rearrangement of atoms in the top few layers in this temperature regime. However, except for very thin films, this mobile surface region will be a tiny fraction of the film and its mobility will be hard to detect except by surface techniques. The NMR data and latent heat data of Figure 2 both suggest that the width of the roughened interface is approximately 4 layers.

If the elevation of the molecular mobility is due to roughening, one might expect to see the effect turn off below the roughening temperature, 78 K. But the roughening transition of the bulk solid surface is of the KTHNY type,[96] and is therefore infinitely continuous. If this were true of roughening in films, one could at best hope to observe a smooth hump or a rounded corner as its signature in T_2 at the roughening transition temperature.[97] However, roughening is strictly speaking a property of the bulk interface; as we described in Section 1.4, roughening in films is represented by a series of layer-condensation critical points,[24] and in the first layer, at least, the critical point has been shown to be Ising-like.[46] There is thus some hope that the roughening transition can be detected by NMR; but it is not surprising that the signal is not obvious in our data.

Clearly the temperature dependence of T_2 below the melting transition is weaker for thin films than for the bulk. It is tempting to suppose that whatever the dominant relaxation mechanism may be, that T_2 can still be described by the activated form, $T_2 = \tau_0 \exp(-E_d / T)$. Indeed, the energy barrier E_d, derived in this way for films of less than 4 layers, is very close to the bulk liquid value, 390 K. While this result is intriguing,

it must be borne in mind that the prefactor τ_0 will be strongly dependent on the detailed structure of the film, and it may be quite incorrect to treat it as a constant. The data do not appear to warrant a more detailed analysis.

Chapter 6

Conclusions

Let us now return to our original question, how melting in two and three dimensions are related.

§6.1 Discussion

1. *Melting*

We have traced the melting transition from the bulk to one monolayer. Down to 5 layers, the high-resolution heat capacity measurements of Lysek[52] yield a melting curve in agreement with a bulk continuum model of the film. For lower coverages, where the latent heat of melting vanishes, we have been able to observe melting down to nearly one monolayer, though with poorer temperature resolution. We find that the transition persists into the region of coverage where the latent heat vanishes. The solid phase becomes soft in very thin films, where the rough surface layer comprises most of the film. The multilayer melting curve appears to join onto the submonolayer melting curve, but the exact trajectory remains unknown.

Another point to be emphasized is that we observe an increase in mobility associated with the uppermost layers, since all of the pictures we have discussed as possible explanations involve the motion of molecules at the surface. That is to say, qualitatively speaking, the introduction of a third degree of freedom softens the solid by allowing molecules to slide over one another; and thickening the film re-hardens the solid by increasing the average co-ordination number of each molecule.

2. *Wetting*

We have presented a qualitative model of the effect of the substrate on T_1 in the adsorbed film and shown that it can be ascribed to fixed paramagnetic spin centers in the substrate. The effect is strongly dependent on the distribution of the film with respect to

the surface, and therefore is a sensitive diagnostic of the wetting behavior of the adsorbed medium. Our data indeed indicate that methane wets graphite to a thickness of over 50 layers. This is a significant result, because the model of Gittes and Schick[18] predicts that non-wetting solids may form well over 20 layers before growth saturates and bulk condensation begins. Unlike other methods that have been applied to the growth of such thick films, such as the fiber oscillator microbalance[98] and ellipsometry,[99] NMR yields a direct measurement of the distribution of the adsorbate, and should provide a signal from both film and bulk components in non-wetting systems. It would be interesting to test the NMR method on a system known to be non-wetting.

3. *Capillary condensation*

Following Cole and Saam,[100] we may attempt to calculate the limits of stability of the film with respect to the formation of capillary condensation. Let us consider a roughly rectangular cavity between two Grafoil platelets, separated by a distance $2D$ (so that a film of thickness D saturates the pore). The excess Landau potential per area of a filled pore includes the energy cost of forming bulk material off the co-existence curve, and the surface tension of the substrate, so $\Omega_2^{cap}/A = \rho_i D\,(\mu_i(T)-\mu)+\sigma_{i\omega}$. Comparing this to the result of Section 3.2 for the Landau potential of a homogeneous film, we find that the capillary condensed phase has a lower free energy when

$$\frac{3}{2}\rho_i\,(\Delta C_3^{i\omega})^{1/3}\,(\mu_i(T)-\mu)^{2/3}+\sigma_{ig} > \rho_i D\,(\mu_i(T)-\mu).$$

The numerical coefficient of the first term on the left hand side is small, so the onset of capillary condensation occurs approximately when $\mu_i(T)-\mu = \sigma_{ig}/\rho_i D$; that is, when the cost of forming the film-vapor interface outweighs the cost of forming bulk. The surface tension of solid methane is not known, but for the liquid, $\sigma_{lg} = 13\ \mathrm{K}/\mathrm{\AA}^2$.[101] We may estimate the average spacing D from the known density and specific area of Grafoil to be 300 Å. We would conclude that liquid films of more than 4 layers should be unstable against capillary condensation in Grafoil.

Nevertheless, our saturation recovery curves show no evidence of co-existence between a thin-film, short-T_1 phase and a capillary-condensed, long-T_1 phase, where the T_1 for each phase should be independent of the amount of adsorbate. (The data shown in Figure 18 should represent approximately the worst case of such an admixture.) Instead, we measure a single time constant which varies with coverage. This may be due to the fact that to convert from the metastable film phase to the capillary condensed phase requires a large fluctuation in the distribution of mass, for there is no force to drive the transition unless the opposing film surfaces meet, and so the transition may not easily nucleate. Our procedure for growing the film, condensing the methane slowly as the temperature of the substrate drops, rather than exposing a cold surface to the gas, should favor the formation of the metastable phase. In short, while some small fraction of the methane undoubtedly exists in capillary form, the resulting NMR data shows that the methane behaves as though on the whole it is uniformly distributed on the surface.

4. *Roughening and surface melting*

Let us consider the nature of the mobile surface layer we believe is associated with roughening. Can this layer be thought of as a liquid?

Both roughening and surface melting are said to occur in the system of argon on graphite. However, the claim of Zhu and Dash[27] that their heat capacity data indicate that roughening and surface melting are distinct is unconvincing for the following reason. The surface of the liquid is always rough because of capillary waves;[102] the surface melted phase is therefore also rough. The smooth phase must thus be solid; and if the surface melted phase extends down to the roughening transition (as in the Zhu and Dash experiment) then a first order transition between solid and surface melted phases, such as we described in Section 3.5, pre-empts the roughening transition. Under such circumstances, the rough phase and the surface melted phase are identical.

In the neutron scattering experiment of Bienfait,[30] a mobile component of a film of methane on MgO was detected, and found to have a characteristic energy barrier for

diffusion much less than that of the solid, but somewhat higher than that of the liquid. On this basis, the mobile component was identified as a "lattice fluid," and the conclusion was made that methane on MgO exhibits surface melting. However, the picture of mobile molecules arranged on a regular lattice agrees more with the idea of roughening than of surface melting.

Since surface melting by definition is not possible for a submonolayer film, the supposition that surface melting and roughening co-exist requires the existence of a triple point between solid, liquid and surface melted phases, as discussed in Section 3.5. Since such a triple point is not observed in the heat capacity or NMR data for methane on graphite, it would appear that roughening, and not surface melting, is the origin of the mobility increase in thin solid methane films.

Conversely, our thermodynamic analysis has predicted a pair of new phase transitions, from solid or liquid to the surface melted phase, that have not hitherto been observed, but that ought to be seen in systems which exhibit surface melting. Further study of such systems would be desirable.

§6.2 Towards the future

At the end of any experiment, there are always questions left that remain unanswered, or that have arisen in the course of the work itself.

1. We would like to know more about the spin centers in graphite that relax the longitudinal magnetization in the film, as discussed in Section 5.2. Electron paramagnetic resonance measurements should in principle be able to determine the concentration of paramagnetic sites, but because of the electrical conductivity of graphite, this measurement is quite difficult.

From our understanding of the origin of substrate interactions, we can make the following recommendations to improve experimental sensitivity.

2. Since the relaxation rate for the spin centers is on the order of 10^8 sec^{-1}, which is just about the Larmor frequency of the present experiment, the effect of paramagnetic relaxation on T_1 in the film can be reduced by going to higher frequencies, to take advantage of the factor $1+\omega_I{}^2\tau^2$ in the denominator of Eq. (8). Then T_1 would be a more sensitive indicator of molecular behavior in the film.

3. Since the effects of DC field inhomogeneities in the bounded-diffusion model vary as the square of the Larmor frequency, they can be drastically reduced by going to lower fields to make T_2 a more sensitive probe of molecular motions.

4. Another solution to the problem of substrate effects would be to go to a different substrate. However, as we noted in Section 1.6, no other system is known where both solid and liquid wet the substrate and the melting transition is not pre-empted by surface melting, so no candidate for a replacement for the methane/graphite system can be suggested here.

A better theoretical picture of the system would be helpful also.

5. Calculations of the effect of roughening on the mobility of surface molecules would be interesting, as well as an analysis of the thickness of the roughened interface for finite films, and its dependence on temperature and coverage.

6. While we made some general observations of the effects of dimensionality on the melting transition at the end of Section 6.1.1, more quantitative analysis of the behavior of the system is necessary before detailed comparison to experimental results can be obtained.

Corroborative experiments can help answer questions that NMR cannot address.

7. Neutron scattering experiments might be helpful in understanding the structure of the softened solid thin films, perhaps distinguishing between roughening and surface melting. The interpretation of such experiments must be made carefully, however.

8. Scattering experiments made at wavenumbers on the length scale of the surface correlation length should be able to probe roughening directly: specular scattering from the surface should become diffuse at the transition.[103]

9. We have found that thin solid films are qualitatively different from the bulk in their microscopic behavior, and heat capacity experiments show the difference in free energy between thin films of solid and liquid is much reduced from that of the bulk; and yet the model of Section 3.3, based on bulk continuum free energies, predicts melting temperatures which are not in disagreement with the present experiment. It would thus appear desirable to use some technique with greater temperature resolution to make more accurate measurements of the melting curve to resolve the paradox. Our thermodynamic analysis can then be used in reverse, to construct free energies from the melting curve, in regions where heat capacity techniques show no signal.

10. Finally, we would like to see experiments to detect the new phase transitions we have predicted for surface melted films; and experiments applying NMR to the study of wetting behavior in extremely thick films.

The methane/graphite system continues to pose experimental and theoretical challenges; the facts we have learned about the system in the present experiment are quite interesting, and lend hope to the promise that methane on graphite is a unique laboratory for the study of the problem of melting.

Appendix I

Rotational States of the Methane Molecule

In this appendix, we shall study the effect of Fermi statistics on the spin wave functions of the methane molecule, and then address the potential complications introduced by the polyatomic nature of methane, which we shall find to be unimportant.

Because the symmetries of the methane molecule have the effect of permuting the co-ordinates of the protons, the molecular wave functions must obey certain transformation properties under the tetrahedral group, T_d, and not all combinations of the total nuclear spin (S), rotational angular momentum (J), and parity (P) are allowed. Since the molecular moment of inertia I is small, the characteristic rotational temperature $\hbar^2 / I\, k_B = 15$ K is quite high, and the question arises, whether the linking of rotational and spin quantum numbers can affect the NMR properties of methane.

Let us begin by considering the allowed states. The four proton spins can add up to $S = 0$ (2 states), $S = 1$ (9 states), or $S = 2$ (5 states). As with molecular hydrogen, the different spin states are sometimes considered different species, and have been given the names E, or *para*-methane ($S = 0$); T, or *ortho*-methane ($S = 1$); and A, or *meta*-methane ($S = 2$). The rotational states of a spherical top such as methane are $(2J + 1)^2$-fold degenerate: one factor of $2J + 1$ is the usual degeneracy of the component of angular momentum along the spin axis; the other is due to the quantization of the direction of the spin axis in the laboratory frame. Finally, in addition to the rigid body rotations, we may consider states where the molecular framework is inverted, and form eigenstates of parity of either sign.

Let the total number of allowed combinations of such states for S, J and P be given by $(2S + 1)(2J + 1)\, d_{SJ}^P$. The values of d_{SJ}^P, computed by group theoretical methods,[104] are shown in the table. For values of $J \geq 12$, the last line of the table can be used to relate the values of d_{SJ}^P to those shown for $J < 12$.

Table of nuclear spin degeneracy factors d_{SJ}^{P}

J	*Parity +*			*Parity −*		
	$S=0$	$S=1$	$S=2$	$S=0$	$S=1$	$S=2$
0	0	0	0	0	0	1
1	0	1	0	0	0	0
2	1	0	0	1	1	0
3	0	1	1	0	1	0
4	1	1	0	1	1	1
5	1	2	0	1	1	0
6	1	1	1	1	2	1
7	1	2	1	1	2	0
8	2	2	0	2	2	1
9	1	3	1	1	2	1
10	2	2	1	2	3	1
11	2	3	1	2	3	0
$12n+J$	$2n+d_{0J}^{+}$	$3n+d_{1J}^{+}$	$n+d_{2J}^{+}$	$2n+d_{0J}^{-}$	$3n+d_{1J}^{-}$	$n+d_{2J}^{-}$

At finite temperatures, the equilibrium population of a particular state will be proportional to the degeneracy of the state times the Boltzmann factor, $\exp(-E_J / k_B T)$, where $E_J = \frac{\hbar^2}{2I} J(J+1)$, I being the moment of inertia. Thus the equilibrium concentrations $x(S)$ of the different spin species is given by $x(S) \propto \sum_{J,P} (2S+1)(2J+1) d_{SJ}^{P} \exp(-E_J / k_B T)$, with the normalization $\sum_{S} x(S) = 1$. The results, shown in Figure 26, show that despite the large rotational energies, at the temperature range of the present experiment, the spin species are present approximately

Figure 26. *Concentration of spin species as a function of temperature. Arrows mark high-temperature limit*

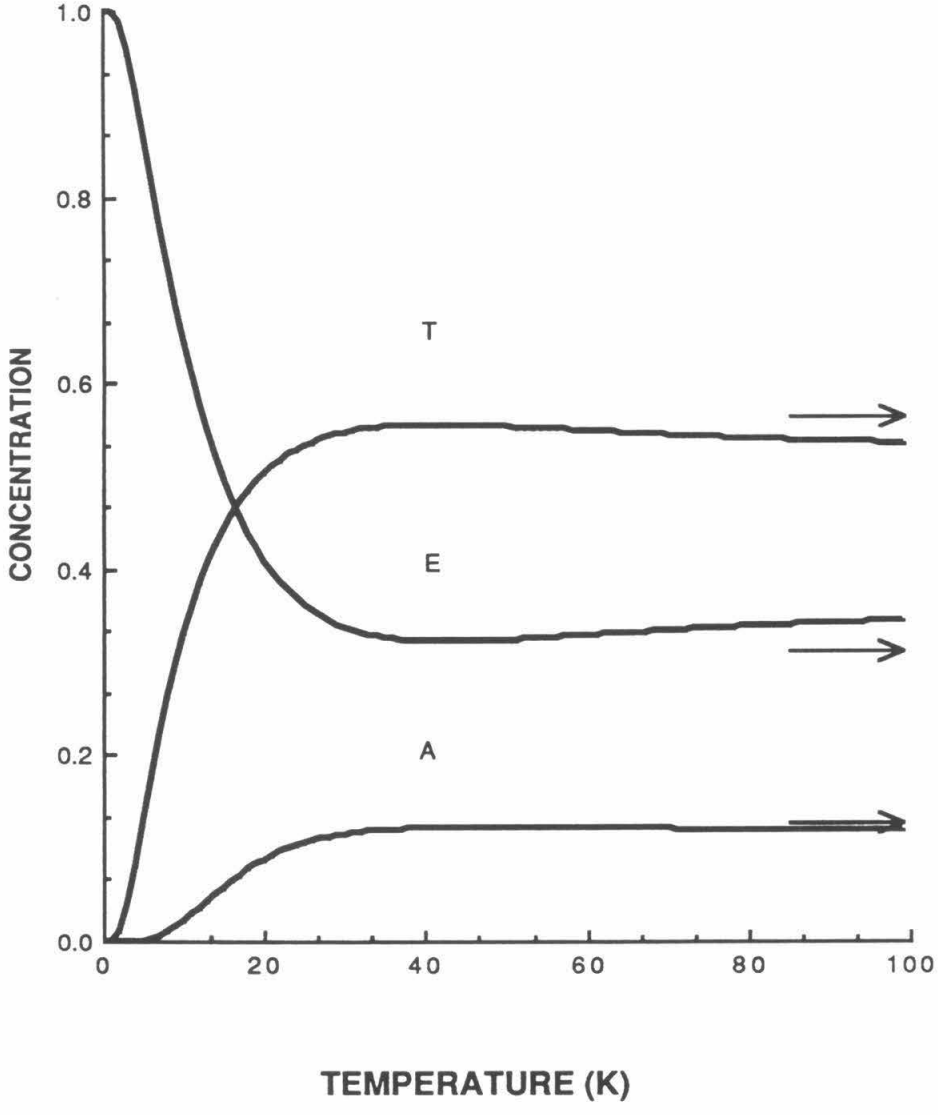

in the proportion 2:9:5, which they would have in the absence of the Pauli principle.

Let us now address the questions raised by the polyatomic nature of methane.

1. *Line splitting*

The protons on a methane molecule are closer to one another than they are to those on neighboring molecules. Furthermore this distance is constant and does not fluctuate. Conceivably, then, the degenerate Zeeman levels might be split by *intra*-molecular dipolar couplings. However, the interaction between two spins A and B can be written in the form $\vec{\mu}_A \cdot \overleftrightarrow{T} \cdot \vec{\mu}_B$, where the tensor $\overleftrightarrow{T}$ is traceless; and so when the molecule is tumbling rapidly, the line splitting will be washed out.[105]

2. *Indirect scalar coupling*

Another possible mechanism for line splitting is the so-called indirect scalar coupling. The dipole field of one nucleus can polarize the electronic wave function, which in turn produces a magnetic field at another nucleus. This results again in an interaction of the form $\vec{\mu}_A \cdot \overleftrightarrow{T} \cdot \vec{\mu}_B$, which, however, need not be traceless. The scalar part of this interaction is also unobservable, though, for the reason that it commutes both with the rest of the Hamiltonian and with the operator for the transverse magnetization $\mathbf{M}_\perp$. It thus can have no effect on the decay of the transverse magnetization for an initial state ψ, $\langle \mathbf{M}_\perp(t) \rangle = \langle \psi | e^{i\mathbf{H}t/\hbar} \mathbf{M}_x e^{-i\mathbf{H}t/\hbar} | \psi \rangle$, which is the Fourier transform of the lineshape (see Chapter 2).[106]

3. *Molecular wave functions*

Next we consider whether it is sufficient to treat the proton spins independently, or whether it is necessary to use molecular spin wave functions, in order to understand the NMR properties of methane. Let us compute, for example, the contribution $1/T_1^{diff}$ of *inter*-molecular dipolar couplings to the longitudinal relaxation rate, caused by molecular diffusion. In the usual approximation,[107] this is proportional to the density of spins N times $S(S+1)$. Let N be the density of molecules; then for individual protons, the

density is $4N$, and $S = ½$, so $1/T_1^{diff} \sim 4N \cdot ¾ = 3N$. On the other hand, if we take the molecular species for our fundamental objects, with the high-temperature proportions 2:9:5, we find $1/T_1^{diff} \sim \frac{2}{16} \cdot N \cdot 0 + \frac{9}{16} \cdot N \cdot 2 + \frac{5}{16} \cdot N \cdot 6 = 3N$, as before. Hence it makes no difference whether we consider the protons independently or together.

4. *Rotational relaxation mechanisms*

The previous argument fails if we attempt to apply it to the contribution $1/T_1^{rot}$ of *intra*-molecular interactions to the relaxation rate (that due to molecular rotation), because the orbital motions of the four protons are strongly correlated. Indeed, in this case it is found[108] that the longitudinal relaxation is not described by a single exponential, but is given by $M_{\|}(t) - M_0 = (M_{\|}(0) - M_0)(a\, e^{-\alpha t/T_1^{rot}} + b\, e^{-\beta t/T_1^{rot}})$; where a=.02, b=.979, α=1.45, β=.99 and $1/T_1^{rot}$ is the relaxation rate calculated neglecting correlations. Fortunately it is seen that the effects are minuscule.

5. *Spin conversion*

Some very pretty experiments have been done studying the rates of interconversion between spin species. For example, since the magnetic susceptibility χ is proportional to $\langle S(S+1)\rangle$, observations of the time dependence of χ can be used to determine equilibration rates.[109] Another experiment is to introduce paramagnetic impurities deliberately into the lattice and study the field dependence of the equilibration rate. One tunes the magnetic field until the Zeeman splitting of the impurity equals the energy difference between rotational levels for the methane molecules, providing an efficient conversion mechanism between species. One has thus a spectroscopy for determining rotational energies in the solid.[110]

In our experiment, however, we are in the high-temperature limit at all times, and do not need to worry about achieving equilibrium amongst the spin species.

In conclusion, we find that while the polyatomic nature of methane leads to quite interesting phenomena at low temperatures, it does not produce any complications for our experiment, and we can treat the protons independently.

Appendix II

The Trouble with Grafoil

Although in many ways Grafoil is an ideal substrate, the difficulties involved in using it in an NMR experiment are manifold. All of the following points need be considered.

1. DC magnetic susceptibility is anisotropic and inhomogeneous, reducing DC field homogeneity
2. electrical conductivity lowers Q of coil, reducing the size of both H_1 and the induction signal
3. RF magnetic field induces eddy currents and generates heat
4. eddy currents exclude magnetic flux, reducing H_1 homogeneity
5. magnetic interaction of paramagnetic centers in the substrate with nuclear spins affects T_1 and T_2

Many of the above can be ameliorated if we can make it difficult for eddy currents to flow in the Grafoil. As described above, in Section 1.6, the platelets in Grafoil are partially aligned, and so the first step is to use the anisotropy of the conductivity of graphite by orienting the easy axes with both H_0 and H_1, as shown in Figure 27. Currents along the third axis are further reduced by inserting 1 mil teflon spacers between the sheets of Grafoil. Teflon contains no hydrogen to contribute to the NMR signal, and is easy to outgas, especially in such thin samples. About .11 cc of teflon altogether are used.

The resultant FID decay time in the presence of the substrate is not much shorter than in the experiments on pure bulk methane performed in the same magnet. We may therefore deduce that the DC field inhomogeneity is not much worse than that intrinsic to the magnet. However, because the characteristic length of the perturbations introduced by the Grafoil is so small, it has a strong effect on T_2 which is discussed in Section 5.3.

Grafoil reduces the Q of the coil from 240 to 3. The addition of teflon spacers raises this value to 10. However, as described in Section 4.4, the gain of the tank circuit

Figure 27. *Orientation of Grafoil sheets in DC and RF magnetic fields*

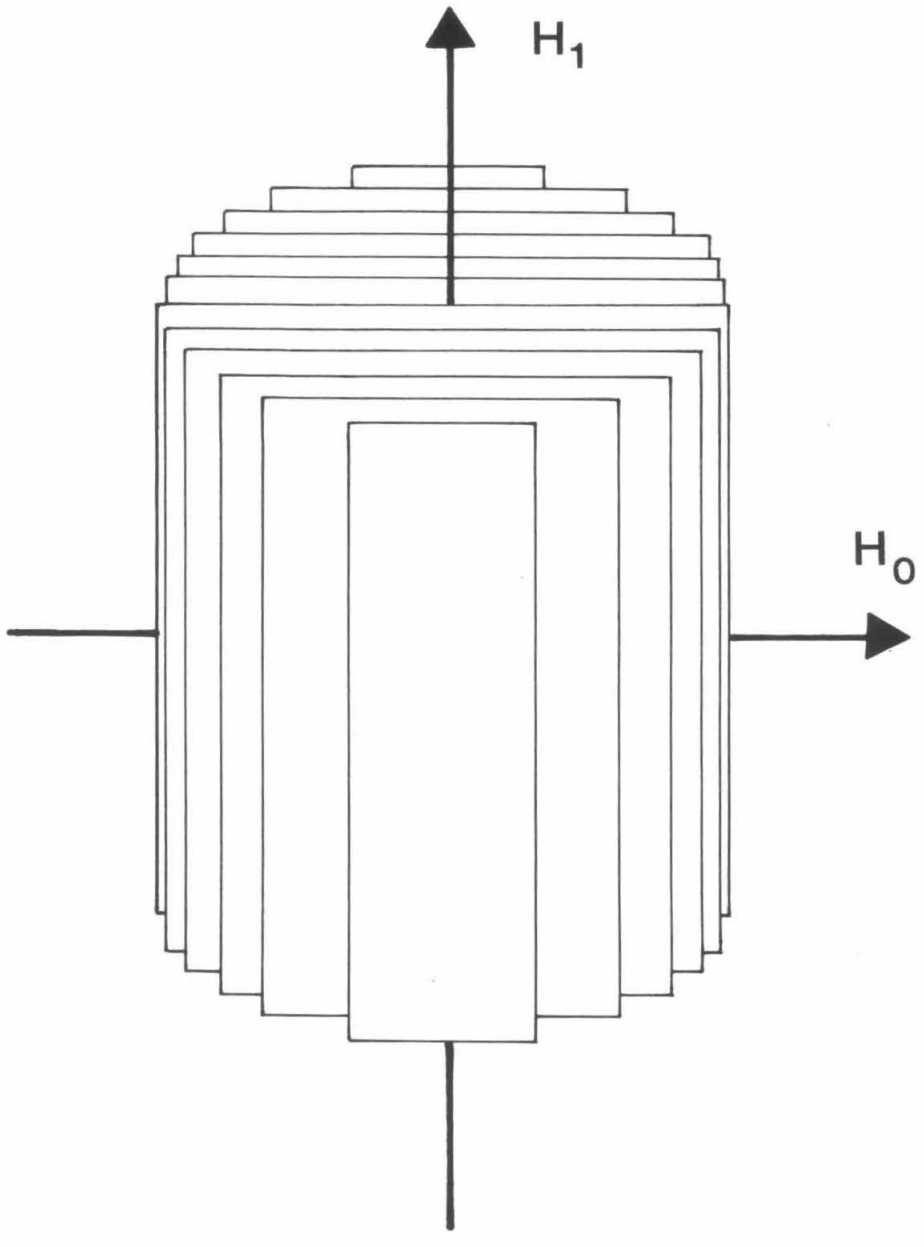

only goes as $\sqrt{Q}$ when tuned to critical coupling, rather than the linear Q dependence computed for uncoupled circuits. So a Q of 10 is acceptable. In our experiments without Grafoil, the limiting loss factor is not the Q of the coil, but dielectric loss in the coax included in the tank circuit.

Since the RF pulse lasts for at most 10 μsec, at a power of 200 W, 2 mJ of heat are deposited in the Grafoil. At 90 K, 1.4 g of graphite has a heat capacity of .17 J/K,[111] so the temperature rise is 12 mK. This is acceptable as long as the repetition rate is low.

The effect of the Grafoil on H_1 homogeneity can be estimated as follows. For a uniform conductive medium in a cylindrical coil of radius a, smaller than a wavelength, H_1 varies with radius r as

$$H_1(r) = H_1(a)\, J_0(\frac{r}{\delta}(1+i)), \tag{11}$$

where $\delta = c / \sqrt{2\pi\omega\sigma}$ is the skin depth,[112] c the speed of light, and and σ the conductivity. We expand the Bessel function for small arguments, and integrate to find the total flux Φ.

Then since Q is the ratio of the real and imaginary parts of the impedance, $Q = \mathrm{Re}\Phi / \mathrm{Im}\Phi = 4\delta^2 / a^2$. Substituting into Eq. (11), we have $|H_1(0)/H_1(a)| = 1 - 1/4Q^2 = 99.98\%$ for a Q of 10. Much more serious are the effects due to the finite size of the coil, and the repulsion of flux by eddy currents in the thermal shield.

The last item, the magnetic interaction between substrate and adsorbate, is discussed at length in Section 5.2.

Appendix III

Computation of the FHH coefficient

It is a widespread practice in the literature[113] to compute the coefficient ΔC_3 of the FHH equation from a model (which we shall refer to as the linear superposition model) by arguing that the relevant potential is the difference in the potentials felt by a gas molecule in the presence of the substrate from that of a homogeneous half space of the adsorbed phase. One then calculates the pressure profile $p(z)$ from hydrostatics and assumes that the interface occurs at the height above the surface where the pressure equals the bulk co-existence pressure, $p(z) = p_0(T)$. However, as Dzyaloshinskii, Lifshitz and Pitaevskii[114] (DLP) point out, the van der Waals interaction between two media, being electromagnetic in nature, will be modified by the presence of an intervening dielectric film. (Analogously, for a medium of molecules of polarizability α and density ρ, the dielectric constant of the medium is not $\varepsilon = 1 + 4\pi\rho\alpha$ but $\varepsilon = (1 + 8\pi\rho\alpha/3)/(1 - 4\pi\rho\alpha/3)$, according to the Clausius-Mossotti equation.[115]) The FHH coefficient thus cannot be computed by a model which linearly adds and subtracts potentials.

In particular, DLP gives, in our notation,

$$\Delta C_3^{as} = -\frac{\hbar}{8\pi^2\rho}\int_0^\infty \frac{\varepsilon_a - 1}{\varepsilon_a + 1}\,\frac{\varepsilon_a - \varepsilon_s}{\varepsilon_a + \varepsilon_s}\,d\omega, \tag{12}$$

where the ε's are the dielectric constants evaluated at imaginary frequency, $\varepsilon(i\,\omega)$, and a and s indicate adsorbate and substrate. From the limit of this equation as the density of the adsorbate vanishes, Vidali and Cole[116] find for the van der Waals potential of a single molecule above the surface

$$C_3^{(s)} = \frac{\hbar}{4\pi}\int_0^\infty \frac{\varepsilon_s - 1}{\varepsilon_s + 1}\,\alpha_a\,d\omega.$$

The linear superposition model of Ref. (113) thus gives

$$\Delta C_3^{as} = \frac{\hbar}{4\pi}\int_0^\infty \left[\frac{\varepsilon_s - 1}{\varepsilon_s + 1} - \frac{\varepsilon_a - 1}{\varepsilon_a + 1} \right] \alpha_a \, d\omega. \tag{13}$$

It is easy to show, using the Clausius-Mossotti equation, that Eqs. (12) and (13) are identical in the limit that both media are weakly polarizable. In general, however, the two models give different results.

By way of illustration, we give a computation of the FHH coefficient for methane on graphite, using the approximation of Ref. (116), that the dielectric properties of both media can be described by an oscillator model, in which each molecule behaves like a simple harmonic oscillator with a single characteristic frequency. In this model,

$$\alpha(i\,\omega) = \frac{\alpha(0)}{1 + \omega^2/{\omega_0}^2},$$

where $\alpha(0)$ is the static polarizability and ω_0 is the characteristic excitation frequency. This model yields good results for the substrate van der Waals coefficient. With the abbreviated notation $\alpha^* = 4\pi\rho\,\alpha(0)/3$ and $x = 1 + \omega^2/{\omega_0}^2$,

$$\frac{\varepsilon_a - 1}{\varepsilon_a + 1} = \frac{3\,\alpha_a{}^*}{\alpha_a{}^* + 2 + 2\,\omega^2/{\omega_{0a}}^2}$$

and

$$\frac{\varepsilon_a - \varepsilon_s}{\varepsilon_a + \varepsilon_s} = \frac{3\,(\alpha_a{}^* x_s - \alpha_s{}^* x_a)}{(2 + \alpha_s{}^* + \alpha_a{}^* - 4\,\alpha_a{}^*\,\alpha_s{}^*) + \left[\dfrac{\alpha_a{}^* + 2}{{\omega_{0s}}^2} + \dfrac{\alpha_s{}^* + 2}{{\omega_{0a}}^2} \right] \omega^2 + \dfrac{2}{{\omega_{0a}}^2\,{\omega_{0s}}^2}\,\omega^4}.$$

The poles of these functions are obvious, and the integrals of Eqs. (12) and (13) are easily evaluated. The results are, for liquid methane on graphite:

ΔC_3^{as} (DLP)=1.33×10^4 KÅ^3

ΔC_3^{as} (linear superposition)=1.25×10^4 KÅ^3

The discrepancy is not large. The surface melting model of Section 3.4 is based on the assumption that the van der Waals potential is additive, and so the linear superposition model values are used there:

$\Delta C_3^{s\omega} = 1.20\times10^4$ KÅ^3

$\Delta C_3^{l\omega} = 1.25\times10^4$ KÅ^3

$\Delta C_3^{ls} = 502$ KÅ^3

Appendix IV

White Noise

We wish to estimate the error in the integral of a digitized signal from the measured RMS noise level. Suppose that a white noise signal $V(t)$ has a Fourier transform

$$A(\omega) = \frac{1}{2\pi}\int V(t)\, e^{-i\omega t}\, dt.$$

According to the standard theory of white noise,[117] $\langle A(\omega)\, A^*(\omega')\rangle = J(\omega)\,\delta(\omega-\omega')$ and $\langle V^2\rangle \doteq 2\pi J(0)\,\Delta f$, where $J(\omega)$ is the power spectrum of V, and Δf is the bandwidth of the noise.

Now let us compute the integral for a period T,

$$F = \int_{-T/2}^{T/2} V(t)\, dt.$$

We can consider F to be the integral over all time of the product of $V(t)$ with a square pulse. Using the convolution theorem, and putting $\sin(\omega T/2)/\pi\omega$ for the Fourier transform of a square pulse,

$$F = \int \frac{\sin \omega T/2}{\pi\omega}\, A(\omega'-\omega)\, e^{i\omega' t}\, d\omega\, d\omega'\, dt$$

$$= \int \frac{2\sin \omega T/2}{\omega}\, A(-\omega)\, d\omega, \quad \text{so}$$

$$\langle F^2\rangle = 4\int \frac{\sin \omega T/2}{\omega}\,\frac{\sin \omega' T/2}{\omega'}\,\langle A(-\omega)\, A^*(-\omega')\rangle\, d\omega'\, d\omega$$

$$= 4\int \frac{\sin^2 \omega T/2}{\omega^2}\, J(\omega)\, d\omega \simeq 2\pi J(0)\, T = \frac{\langle V^2\rangle}{\Delta f}\, T.$$

Now if we are digitizing the signal, T equals the number of points N sampled divided by the sampling rate f_s, so $\langle F^2\rangle = N\,\langle V^2\rangle/\Delta f\, f_s$.

If we were naïvely to assume that the voltages at every sampling point are completely uncorrelated, so that they add in quadrature, we would estimate

$$\langle F^2 \rangle = N \frac{\langle V^2 \rangle}{{f_s}^2}.$$

This underestimates the RMS noise on the integral by a factor of $\sqrt{f_s/\Delta f}$.

References

[1] L. Frank Baum, *The Wizard of Oz* (Bobbs-Merrill, Indianapolis, 1944).

[2] Aristotle, *Complete Works*, J. Barnes, ed., E. W. Webster, tr. (Princeton University Press, Princeton, 1984).

[3] F. A. Lindemann, Phys. Z. **14**, 609 (1910).

[4] S. Alexander and J. P. McTague, Phys. Rev. Lett. **41**, 702 (1978). A claim for a violation of this theorem by NH_3 at high pressure is given by Ph. Pruzan, D. H. Liebenberg and R. L. Mills, Phys. Rev. Lett. **48**, 1200 (1982).

[5] J. M. Kosterlitz and D. J. Thouless, J. Phys. **C6**, 1181 (1973).

[6] D. R. Nelson and B. I. Halperin, Phys. Rev. **B19**, 2457 (1979); A. P. Young, Phys. Rev. **B19**, 1855 (1979).

[7] L. D. Landau and E. M. Lifshitz, *Statistical Physics*, Pt. 1, 3rd ed., E. M. Lifshitz, L. P. Pitaevskii, eds., J. B. Sykes, M. J. Kearsley, trs., §138 (Pergamon, Oxford, 1982).

[8] G. A. Williams, Phys. Rev. Lett. **59**, 1926 (1987).

[9] C. A. Murray and D. H. van Winkle, Phys. Rev. Lett. **58**, 1200 (1987).

[10] C. C. Grimes, Surf. Sci. **73**, 379 (1978); A. J. Dahm and W. F. Vinen, Phys. Today **40**, 43 (1987).

[11] D. J. Bishop and J. D. Reppy, Phys. Rev. Lett. **40**, 1727 (1980).

[12] A. D. Migone, M. H. W. Chan, K. J. Niskanen and R. B. Griffiths, J. Physique **C16**, L1115 (1983); M. H. W. Chan, A. D. Migone, K. D. Miner and Z. R. Li, Phys. Rev. **B30**, 2681 (1984).

[13] H. K. Kim, Q. M. Zhang, M. H. W. Chan, Phys. Rev. Lett. **56**, 1579 (1986); M. Nielsen, J. Als-Nielsen, J. Bohr, J. P. McTague, D. E. Moncton and P. W. Stephens, Phys. Rev. **B35**, 1419 (1987).

[14] P. A. Heiney, R. J. Birgeneau, G. S. Brown, P. M. Horn, D. E. Moncton and P. W. Stephens, Phys. Rev. Lett. **48**, 104 (1982); P. A. Heiney, P. W. Stephens, R. J. Birgeneau, P. M. Horn and D. E. Moncton, Phys. Rev. **B28**, 6416 (1983).

[15] A. Silva-Moreira, J. Codona and D. Goodstein, Phys. Lett. **76A**, 324 (1980).

[16] T. Young, Phil. Trans. **95**, 69 (1805).

[17] D. A. Huse, Phys. Rev. **B29**, 6985 (1984).

[18] F. T. Gittes and M. Schick, Phys. Rev. **B30**, 209 (1984).

[19] K. Kern, R. David, R. L. Palma and G. Cosma, Phys. Rev. Lett. **56**, 2823 (1986).

[20] M. Bienfait, J. L. Seguin, J. Suzanne, E. Lerner, J. Krim and J. G. Dash, Phys. Rev. **B29**, 983 (1984).

[21] J. Cahn, J. Chem. Phys. **66**, 3667 (1977).

[22] R. Pandit and M. E. Fisher, Phys. Rev. Lett. **51**, 1772 (1983).

[23] S. Dietrich, *Phase Transitions and Critical Phenomena*, v. 10, C. Domb and J. Lebowitz, eds. (Academic, New York, 1987).

[24] R. Pandit, M. Schick and M. Wortis, Phys. Rev. **B26**, 5112 (1982).

[25] M. W. Conner and C. Ebner, Phys. Rev. **B36**, 3683 (1987).

[26] J. J. Hamilton and D. L. Goodstein, Phys. Rev. **B28**, 3838 (1983).

[27] D.-M. Zhu and J. G. Dash, Phys. Rev. Lett. **57**, 2959 (1986).

[28] S. Balibar and B. Castaing, J. Phys. Lett. **41**, L329 (1980); J. E. Avron, L. S. Balfour, C. G. Kuper, J. Landau, S. G. Lipson and L. S. Schulman, Phys. Rev. Lett. **45**, 814 (1980); H. J. Maris and A. F. Andreev, Phys. Today **40**, 25 (1987).

[29] G. An and M. Schick, preprint.

[30] M. Bienfait, Europhys. Lett. **4**, 79 (1987).

[31] J. Krim, J. P. Coulomb, J. Bouzidi, Phys. Rev. Lett. **58**, 583 (1987); M. Bienfait and J. P. Palmari, Proc. ICSOS II, J. F. van der Veen, M. A. van Hove, eds. (Springer, Amsterdam, 1986); D.-M. Zhu and J. G. Dash, Phys. Rev. Lett. **60**, 432 (1988); R. Chiarello, J. P. Coulomb, J. Krim and C. L. Wang, preprint.

[32] R. Boyle, cited by J. Dewar, Proc. Roy. Inst. **18**, 177 (1905).

[33] A. D. Migone, H. K. Kim, M. H. W. Chan, J. Talbot, D. J. Tildesey and W. A. Steele, Phys. Rev. Lett. **51**, 192 (1983); J. M. Gay, J. Suzanne and R. Wang, J. Chem. Soc. Faraday Trans. II **82**, 1669 (1986).

[34] A. Terlain and Y. Lahrer, Surf. Sci. **125**, 304 (1983).

[35] A. J. Nijman and A. J. Berlinsky, Phys. Rev. Lett. **38**, 408 (1977).

[36] H. M. James and T. A. Keenan, J. Chem. Phys. **31**, 12 (1959).

[37] T. Yamamoto and Y. Kataoka, J. Chem. Phys. **48**, 3199 (1968).

[38] J. J. Hamilton, thesis, California Institute of Technology, 1983.

[39] D. P. Grimmer and K. Luszczynski, in *Low Temperature Physics—LT13*, K. D. Timmerhaus, W. J. O'Sullivan and E. F. Hammel, eds., p. 170 (Plenum, New York, 1974).

[40] H. Taub, K. Carneiro, J. K. Kjems, L. Passell and J. P. McTague, Phys. Rev. **B16**, 4551 (1977).

[41] J. K. Kjems, L. Passell, H. Taub, J. G. Dash and A. D. Novaco, Phys. Rev. **B13**, 1446 (1976).

[42] X. Duval and A. Thomy, C. R. Acad. Sci. Paris, **259**, 4007 (1964).

[43] N. Fuschillo and C. A. Renton, Nature **180**, 1063 (1957).

[44] R. J. Birgeneau, P. A. Heiney, and J. P. Pelz, Physica **109&110B**, 1785 (1982).

[45] M. Bretz, A. G. Shastri and J. Schwank, J. Mat. Res. **1**, 114 (1986).

[46] H. K. Kim, Q. M. Zhang and M. H. W. Chan, Phys. Rev. **B34**, 4699 (1986); H. K. Kim and M. H. W. Chan, Phys. Rev. Lett. **53**, 170 (1984).

[47] J. Z. Larese, M. Harada, L. Passell, J. Krim and S. Sajita, Phys. Rev. **B**, to be published.

[48] J. M. Phillips, Phys. Rev. **B34**, 2823 (1986).

[49] D. L. Goodstein, J. J. Hamilton, M. J. Lysek and G. Vidali, Surf. Sci. **148**, 187 (1984).

[50] J. Krim, J. M. Gay, J. Suzanne and E. Lerner, J. Physique **47**, 1757 (1986).

[51] H. K. Kim, Q. M. Zhang and M. H. W. Chan, J. Chem. Soc. Faraday Trans. II **82**, 1647 (1986).

[52] M. J. Lysek, M. S. Pettersen and D. L. Goodstein, Phys. Lett. **A115**, 340 (1986); M. S. Pettersen, M. J. Lysek and D. L. Goodstein, Surf. Sci. **175**, 141 (1986).

[53] L. D. Landau and E. M. Lifshitz, §83.

[54] A. Abragam, *Principles of Nuclear Magnetism,* ch. I, §§I.A, I.C, I.D, ch. II, §§A, E, ch. VI, §I.A, ch. VIII, §§II.E.c, III.A.c, ch. X, §I (Oxford University Press, Oxford, 1983).

[55] E. Merzbacher, *Quantum Mechanics*, ch. 10.9 (McGraw-Hill, New York, 1964).

[56] F. Bloch, W. W. Hansen and M. Packard, Phys. Rev. **70**, 474 (1946).

[57] E. M. Purcell, H. C. Torrey and R. V. Pound, Phys. Rev. **69**, 39 (1946).

[58] H. Goldstein, *Classical Mechanics*, ch. 4.8 (Addison-Wesley, Reading, Mass., 1965).

[59] J. S. Rigden, Rev. Mod. Phys. **58**, 433 (1986).

[60] E. Hahn, Phys. Rev. **80**, 580 (1950).

[61] H. Y. Carr and E. M. Purcell, Phys. Rev. **94**, 630 (1954).

[62] J. Frenkel, *Kinetic Theory of Liquids* (Oxford University Press, London, 1949); G. D. Halsey, Jr., J. Chem. Phys. **16**, 931 (1948); T. L. Hill, J. Chem. Phys. **17**, 590 (1949).

[63] L. D. Landau and E. M. Lifshitz, §160.

[64] E. M. Hauge and M. Schick, Phys. Rev. **B27**, 4288 (1983).

[65] P. G. de Gennes, J. Physique-Lettres **42**, 1377 (1981).

[66] E. G. MacRae and R. A. Malic, Phys. Rev. Lett. **58**, 1437 (1987); D. Beaglehole and D. Nason, Surf. Sci. **96**, 357 (1980).

[67] B. Pluis, A. W. Denier van der Gon, J. W. M. Frenken and J. F. van der Veen, Phys. Rev. Lett. **59**, 2678 (1987).

[68] S. G. Hegde, E. Lerner and J. G. Daunt, Phys. Lett. **49A**, 437 (1974).

[69] H. S. Sandhu, J. Chem. Phys. **44**, 2320 (1966).

[70] V. G. Manzhelii and A. M. Tolkachev, Sov. Phys. Sol. State **5**, 2506 (1964) (tr. Fiz. Tverd. Tela. **5**, 3413 (1963)).

[71] A. Roth, *Vacuum Technology*, 2nd ed., ch. 2.7.3 (North-Holland, Amsterdam, 1982).

[72] D. F. Baker and R. H. Bragg, Phil. Mag. **B48**, 475 (1983).

[73] L. G. Rubin and Y. Golahny, Rev. Sci. Inst. **43**, 1758 (1972).

[74] W. G. Clark, Rev. Sci. Inst. **35**, 316 (1964).

[75] E. Fukushima and S. B. W. Roeder, *Experimental Pulse NMR, a Nuts and Bolts Approach*, ch. V.C.9 (Addison-Wesley, Reading, Mass., 1981).

[76] E. Fukushima and S. B. W. Roeder, ch. V.C.7.

[77] A. Abragam, ch. III, §IV.B.d.2.

[78] E. Fukushima and S. B. W. Roeder, ch. VI.A.3.

[79] P. Taborek and D. Goodstein, Rev. Sci. Inst. **50**, 227 (1979).

[80] P. R. Bevington, *Data Reduction and Error Analysis for the Physical Sciences*, ch. 11.4 (McGraw-Hill, New York, 1969).

[81] G. A. deWit and M. Bloom, Can. J. Phys. **42**, 986 (1965).

[82] P. H. Oosting and N. J. Trappeniers, Physica **51**, 395 (1971).

[83] P. H. Oosting and N. J. Trappeniers, Physica **51**, 418 (1971).

[84] A. Abragam, ch. III, §II.A.a.

[85] D. P. Grimmer and K. Luszczynski, in *Monolayer and Submonolayer Helium Films*, J. G. Daunt and E. Lerner, eds., p. 123 (Plenum, New York, 1973).

[86] B. Cowan, L. Abou-Nasr, M. Fardis and A. Hussain, Phys. Rev. Lett. **58**, 2308 (1987).

[87] G. Wagoner, Phys. Rev. **118**, 647 (1960).

[88] H. Harker, J. B. Horsley and D. Robson, Carbon **9**, 1 (1971).

[89] A. Abragam, ch. IX, §II.A.

[90] Z. Wu, W. Happer and J. M. Daniels, Phys. Rev. Lett. **59**, 1480 (1987).

[91] B. Robertson, Phys. Rev. **151**, 273 (1966).

[92] D. L. Husa, D. C. Hickernell and J. E. Piott, in *Monolayer and Submonolayer Films*, p. 133.

[93] J. G. Dash and R. D. Puff, Phys. Rev. **B24**, 295 (1981).

[94] J. W. Riehl and K. Koch, J. Chem. Phys. **57**, 2199 (1972).

[95] J. H. Quateman and M. Bretz, Phys. Rev. **B29**, 1159 (1984).

[96] C. Rottman and M. Wortis, Phys. Rev. **B29**, 328 (1984).

[97] J. M. Greif, A. F. Silva-Moreira and D. L. Goodstein, in *Ordering in Two Dimensions,* S. K. Sinha, ed., p. 297 (North-Holland, New York, 1980).

[98] P. Taborek and L. Senator, Phys. Rev. Lett. **57**, 218 (1986).

[99] M. Drir, H. S. Nham and G. B. Hess, Phys. Rev. **B33**, 5145 (1986).

[100] M. W. Cole and W. F. Saam, Phys. Rev. Lett. **32**, 985 (1974).

[101] *A Compendium of the porperties of Materials at Low Temperature (Phase I), Pt. I. Properties of Fluids,* V. J. Johnson, ed., WADD Technical Report 60-56 (Wright Air Development Division, 1960).

[102] F. F. Buff, R. A. Lovett and F. H. Stillinger, Jr., Phys. Rev. Lett. **15**, 621 (1965); M. W. Cole, J. Chem. Phys. **73**, 4012 (1980).

[103] P.-Z. Wong and A. J. Bray, Phys. Rev. **B**, to be published.

[104] E. Bright Wilson, J. Chem. Phys. **3**, 276 (1935); L. D. Landau and E. M. Lifshitz, *Quantum Mechanics (Non-relativistic theory)*, 3rd ed., J. B. Sykes and J. S. Bell, trs., §105 (Pergamon, Oxford, 1977); C. H. Anderson and N. F. Ramsey, Phys. Rev. **149**, 14 (1966).

[105] A. Abragam, ch. VI, §II.B.c.1.

[106] A. Abragam, ch. XI, §I.

[107] A. Abragam, ch. VIII, §II.E.c.2.

[108] A. Abragam, ch. VIII, §II.E.a.

[109] R. F. Code and J. Higenbotham, Can. J. Phys. **54**, 1248 (1976).

[110] H. Glättli, A. Sentz and M. Eisenkremer, Phys. Rev. Lett. **28**, 871 (1972).

[111] *A Compendium of the Properties of Materials at Low Temperature (Phase I), Pt. II. Properties of Solids.*

[112] J. D. Jackson, *Classical Electrodynamics*. 2nd ed., ch. 7.7 (Wiley and Sons, New York, 1975).

[113] J. G. Dash, *Films on Solid Surfaces*, ch. 4 (Academic, New York, 1975).

[114] I. E. Dzyaloshinskii, E. M. Lifshitz and L. P. Pitaevskii, Adv. Phys. **10**, 165 (1961) (tr. Sov. Phys. Uspekhi **4**, 153 (1961)).

[115] J. D. Jackson, ch. 4.5.

[116] G. Vidali and M. W. Cole, Surf. Sci. **110**, 10 (1981).

[117] F. Reif, *Fundamentals of Statistical and Thermal Physics*, ch. 15.16 (McGraw-Hill, New York, 1965).